
Nuclear Reaction Studies using Stored Ion Beams at ESR with EXL

Studie von Kernreaktionen mit gespeicherten Ionenstrahlen im ESR mit EXL

Vom Fachbereich Physik der Technischen Universität Darmstadt

zur Erlangung des Grades eines Doktors der Naturwissenschaften (Dr. rer. nat.)

genehmigte Dissertation von M.Sc. Juan Carlos Zamora Cardona aus Bogotá (Kolumbien)

Januar 2016 – Darmstadt – D 17



TECHNISCHE
UNIVERSITÄT
DARMSTADT

Fachbereich Physik
Institut für Kernphysik



Nuclear Reaction Studies using Stored Ion Beams at ESR with EXL
Studie von Kernreaktionen mit gespeicherten Ionenstrahlen im ESR mit EXL

Genehmigte Dissertation von M.Sc. Juan Carlos Zamora Cardona aus Bogotá (Kolumbien)

1. Gutachten: Prof. Dr. Thorsten Kröll
2. Gutachten: Prof. Dr. Muhsin N. Harakeh

Tag der Einreichung: 13.10.2015

Tag der Prüfung: 11.11.2015

Darmstadt – D 17

Bitte zitieren Sie dieses Dokument als:

URN: urn:nbn:de:tuda-tuprints-52639

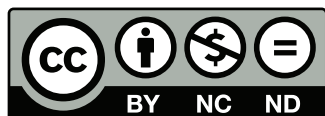
URL: <http://tuprints.ulb.tu-darmstadt.de/5263>

Dieses Dokument wird bereitgestellt von tuprints,

E-Publishing-Service der TU Darmstadt

<http://tuprints.ulb.tu-darmstadt.de>

tuprints@ulb.tu-darmstadt.de



Die Veröffentlichung steht unter folgender Creative Commons Lizenz:

Namensnennung – Keine kommerzielle Nutzung – Keine Bearbeitung 3.0 Deutschland

<http://creativecommons.org/licenses/by-nc-nd/3.0/de/>

Erklärung zur Dissertation

Hiermit versichere ich, die vorliegende Dissertation ohne Hilfe Dritter nur mit den angegebenen Quellen und Hilfsmitteln angefertigt zu haben. Alle Stellen, die aus Quellen entnommen wurden, sind als solche kenntlich gemacht. Diese Arbeit hat in gleicher oder ähnlicher Form noch keiner Prüfungsbehörde vorgelegen.

Darmstadt, den 13.10.2015

(Juan Carlos Zamora Cardona)



*Con profundo amor y agradecimiento
a la memoria mi padre Juan de Jesús Zamora Aldana*



Acknowledgements

This work represents the endeavor and invaluable contribution of many people over several years. Probably only one page would not be enough to mention them all. First, I would like to thank the colleagues which were directly involved in the preparation and execution of the experiment: Branislav Streicher, Yue Ke, Mirko von Schmid, Oleg Kiselev, Manfred Mutterer, Peter Egelhof, Michel Lindemulder, Harry Timersma, Santosh Roy, Catherine Rigollet and Nasser Kalantar-Nayestanaki. During and after the experiment we received a lot of support from many experts, in particular from: Sergey Litvinov, Yuri Litvinov, Fritz Nolden, Markus Steck, Helmut Weick, Holger Kollmus, Ulrich Popp and Nikolaos Petridis.

Foremost, I would like to express my sincere gratitude to my advisor Prof. Thorsten Kröll for his patience, unconditional support, accurate suggestions and the important corrections to this work. Also, I am quite grateful with Prof. Muhsin N. Harakeh for his valuable suggestions and corrections to the analysis and interpretation of the experimental data.

During the time I lived in Darmstadt I received the help of many people to solve different type of problems, in particular I thank to: Ursula von Dungen, Giovanna Umberti, Maria Helm, Mauricio Torres and Claudia Hernández. In the similar way, I am very grateful with my colleagues of AG-Kröll which are also my very best friends: Mirko, Corinna, Ann-Lena, Sasha, Tania, Michael, Sabine, Guille, Han-Bum, Ilja, Christian, Mehmet, Oliver, Timo, Marcus...

Finally, I thank to my beautiful daughter Sofía for the inspiration and strength of every day: *Sofía, tú eres la inspiración y la fuerza que me revitaliza cada día para seguir adelante* ♡



Abstract

In this work, as part of the EXL project nuclear reactions are investigated in inverse kinematics experiments with stored ion-beams. These experiments were carried out at the heavy ion storage ring ESR at GSI with stored ^{58}Ni (at 100 and 150 MeV/u) and ^{20}Ne (at 50 MeV/u) beams. The ^{58}Ni beam was impinged on an internal gas-jet target of helium, while for the ^{20}Ne experiment the internal gas-jet target utilized was hydrogen. The recoil particles produced in different reaction channels were measured with a dedicated detector setup compatible with the Ultra High Vacuum (UHV) in the storage ring. This detector setup included double-sided silicon-strip detectors operating as active barriers between the UHV of the storage ring and an auxiliary vacuum of internal pockets of the experimental chamber. This permitted successful measurements of low energy recoils (hundreds of keV), since both target and detectors were windowless.

Nuclear reaction channels like elastic scattering, excitation of isoscalar giant resonances and neutron pick-up were observed in these experiments. The angular distributions for elastic scattering were analyzed with optical potentials deduced from density-folding models. In particular, the elastic differential cross sections for $^{58}\text{Ni} + \alpha$ were fitted by using the t - $\rho\rho$ potential which is based on the optical limit approximation of the Glauber theory. The resulting RMS point matter-radii are 3.68(10) fm and 3.64(9) fm for the measurements at 100 and 150 MeV/u, respectively. These results are in very good agreement with the literature values.

The excitation of isoscalar giant resonances has been studied for the first time in a stored-beam experiment. In the double-differential cross section measured for $^{58}\text{Ni} + \alpha$ at 100 MeV/u, a well-defined peak in the energy range from 15 to 30 MeV was obtained. A fit with a Lorentz function for the Iso-Scalar Giant Monopole Resonance (ISGMR) component resulted in a centroid of 19.27(61) MeV and a width of 6.45(51) MeV. Moreover, a multipole decomposition analysis was performed to extract the ISGMR contribution. The extracted strength of the ISGMR exhausts 79_{-11}^{+12} % of the Energy-Weighted Sum Rule (EWSR). The results are consistent with the analysis of other experiments performed in the past in normal kinematics as well as theoretical predictions.

A neutron pick-up reaction was measured in the experiment with the stored ^{20}Ne beam. In this experiment, the contribution of the transfer to the ground state and to low-lying states of ^{19}Ne were not kinematically separable. In order to disentangle the different components, a multipole decomposition analysis was applied to the experimental data. Spectroscopic factors were deduced from the analysis of the differential cross section for this transfer reaction. These results are in very good agreement with the predictions from shell model calculations.

The feasibility to perform different types of nuclear reactions with stored ion beams and an internal target by using in-ring detection is successfully demonstrated in this work. This is a paramount milestone toward further EXL experiments with radioactive beams at GSI and in future at FAIR.

Zusammenfassung


In dieser Arbeit wurden als Teil des EXL-Projekts Kernreaktionen in inverser Kinematik mit gespeicherten Ionenstrahlen untersucht. Diese Experimente wurden am Speicherring für Schwerionen, ESR, der GSI durchgeführt mit gespeicherten ^{58}Ni - (bei 100 und 150 MeV/u) und ^{20}Ne -Strahlen (bei 50 MeV/u). Der ^{58}Ni -Strahl traf auf ein internes Gasjet-Target aus Helium, während für den ^{20}Ne -Strahl ein entsprechendes Wasserstoff-Target verwendet wurde. Die Rückstoßteilchen aus den unterschiedlichen Reaktionsskanälen wurden mit einem dedizierten Detektoraufbau vermessen, der mit den Ultrahochvakuumbedingungen (UHV) des Speicherrings verträglich ist. Der Detektor enthielt doppelseitig segmentierte Silizium-Streifenzähler, die als aktive Barriere zwischen dem UHV des Speicherrings und einem Hilfsvakuum in einer sogenannten internen Tasche der Streukammer betrieben wurden. Dies erlaubte die Messung von niederenergetischen Rückstoßkernen (einige 100 keV), da sowohl das Target als auch der Detektor fensterlos waren.

Kernreaktionskanäle wie elastische Streuung, Anregung von isoskalaren Riesenresonanzen und eine Neutrontransferreaktion wurden in diesen Experimenten beobachtet. Die Winkelverteilungen für elastische Streuung wurden mit optischen Potenzialen analysiert, die aus Dichte-Faltungs-Modellen hergeleitet wurden. Insbesondere der differenzielle Wirkungsquerschnitt für die elastische Streuung $^{58}\text{Ni} + \alpha$ wurde angepasst unter Verwendung des t - $\rho\rho$ -Potenzials, welches auf dem optischen Grenzfall der Glauber-Theorie basiert. Die resultierenden RMS-Punktmaterieradien sind 3.68(10) fm und 3.64(9) fm für die Messungen bei 100 bzw. 150 MeV/u. Diese Ergebnisse sind in sehr guter Übereinstimmung mit Literaturwerten.

Die Anregung der isoskalaren Monopol-Riesenresonanz wurde erstmals in einem Experiment mit gespeichertem Strahl untersucht. Der doppelt differenzielle Wirkungsquerschnitt für $^{58}\text{Ni} + \alpha$ bei 100 MeV/u zeigt einen wohldefinierten Peak im Energiebereich zwischen 15 und 30 MeV. Eine Anpassung der isoskalaren Monopol-Riesenresonanz (ISGMR) mit einer Lorentz-Funktion ergab einen Schwerpunkt von 19.27(61) MeV und eine Breite von 6.45(51) MeV. Darüber hinaus wurde eine Multipolzerlegung durchgeführt, um den ISGMR-Anteil zu extrahieren. Die extrahierte Stärke der ISGMR schöpft 79^{+12}_{-11} % der energiegewichteten Summenregel (EWSR) aus. Diese Ergebnisse sind konsistent sowohl mit der Analyse von anderen Experimenten, die in der Vergangenheit in normaler Kinematik durchgeführt wurden, als auch mit Vorhersagen der Theorie.

Eine Neutrontransferreaktion wurde im Experiment mit dem gespeicherten ^{20}Ne -Strahl gemessen. In diesem Experiment konnten die Anteile für den Transfer in den Grundzustand und in niedrigliegende Zustände in ^{19}Ne kinematisch nicht getrennt werden. Um die einzelnen Anteile zu trennen, wurde eine Multipolzerlegung der experimentellen Daten durchgeführt. Die spektroskopischen Faktoren wurden aus dem differenziellen Wirkungsquerschnitt für diese Transferreaktion extrahiert. Die Ergebnisse sind in sehr guter Übereinstimmung mit Vorhersagen aus dem Schalenmodell.

In dieser Arbeit konnte erfolgreich gezeigt werden, dass sich unterschiedliche Typen von Kernreaktionen mit in einem Ring gespeicherten Ionenstrahlen und einem internen Target durchführen lassen.



Dies ist ein wichtiger Meilenstein für weitere EXL-Experimente mit radioaktiven Strahlen bei GSI und in Zukunft bei FAIR.

Contents

1. Introduction	1
1.1. The EXL project	1
1.2. Objectives and outline of this thesis	3
2. Experiment	5
2.1. Production and acceleration of the beam	5
2.2. The heavy ion storage ring (ESR)	6
2.2.1. Stored beam	6
2.2.2. Internal gas-jet target	9
2.3. Detector setup	11
2.3.1. Vacuum chamber bakeout	13
3. Data reduction and calibration	17
3.1. Raw data processing	17
3.1.1. Coherent noise correction	17
3.2. Calibrations	20
3.2.1. Detector calibration	20
3.2.2. Beam and target monitors	21
3.3. Determination of luminosity and cross section	23
3.3.1. Luminosity	23
3.3.2. Cross section	24
4. Simulations	27
4.1. Simulated geometry and the event generator	27
4.1.1. Slit aperture simulations	29
4.2. Angular calibrations	32
4.3. Reaction channels studied with the DSSD2	37
5. Theoretical concepts	45
5.1. Elastic scattering by a short-range potential	46
5.1.1. Scattering amplitude	48
5.1.2. The optical limit of the Glauber theory	48
5.2. Distorted waves	49
5.3. Giant resonances	51

6. Data analysis and results	55
6.1. Elastic scattering and excitation of low-lying states	55
6.1.1. $^{20}\text{Ne} + p$	55
6.1.2. $^{58}\text{Ni} + \alpha$	61
6.2. Isoscalar giant resonances excitation	66
6.2.1. Multipole Decomposition Analysis	71
6.3. Transfer reaction	76
7. Summary and conclusions	83
A. Preparatory works for EXL	87
A.0.1. Crystal correlation (Light leakage)	88
A.0.2. DSSD interstrip signals	91
B. Future upgrades toward full EXL	95
B.1. Optional detector arrangement at the present vacuum chamber	95
B.2. Implementation of the full EXL recoil-detector setup	99
B.2.1. Elastic Scattering	100
B.2.2. Excitation of Isoscalar Giant Resonances	101
B.2.3. Transfer Reactions	102
B.2.4. Quasi-free Scattering	104
C. Continuum Discretized Coupled Channel	107
Bibliography	109

Introduction

Experiments employing light-ion (or neutron) scattering provide important information about the structure of nuclei. For instance, elastic scattering gives access to nuclear potentials and the radial distribution of nuclear matter [1, 2]. Inelastic scattering provides the possibility to study the deformation and collective excited modes of nuclei [3, 4]. In particular, the excitation of giant resonances permits to investigate nuclear bulk properties, e.g., the dipole polarizability and the matter incompressibility [5]. One or few nucleon transfer reactions give information on the single-particle structure and occupation numbers [6, 7]. Usually, these types of experiments are performed in normal kinematics, i.e., light projectiles are impinged on a target composed by the nuclei of interest. However, it is not always possible to produce a target of a given material, this is especially true for radioactive ones. In this case, it is necessary to produce a radioactive beam and to use a stable target composed of the light material. This method is called *inverse kinematics*. In contrast to a normal kinematics experiment, in inverse kinematics the elastically scattered light-particles at forward angles in the center-of-mass-system are detected at laboratory angles in proximity to 90° . Thus, reactions at low momentum transfer are possible without a dedicated spectrometer to select the scattered particles at small angles. A typical limitation of this method are the low luminosities achieved due to a small target density or a low intensity of the radioactive beam. This problem can be overcome by using the novel stored-beam technique. In this technique, the beam is injected into a storage ring which is a kind of circular lattice of electromagnets that keeps the beam particles in circulation in a very clean environment. Thus, the beam revolution frequency inside the storage ring improves the luminosity by several orders of magnitude (as it will be explained in the following chapters). It is clear that for storing the beam in this environment, a low density and windowless target is needed in order to not destroy the beam properties. Therefore, an internal gas-jet target is used in these type of experiments. Additionally, if our objective is to achieve measurements at very low momentum transfer it is also necessary to use windowless detectors because of the small energy of the scattered particles. These principles are employed in the present work to study nuclear reactions in inverse kinematics using stored beams. The results presented here also demonstrate the feasibility of these studies within the EXL project.

1.1 The EXL project

The EXL (**EX**otic nuclei studied with **L**ight-ion induced reactions in storage rings) project is one of the experiments foreseen to be part of the NUSTAR program for **NU**clear **S**tructure, **A**strophysics and **R**eaction studies at the future **F**acility for **A**ntiproton and **I**on **R**esearch (FAIR) [8]. The aim of the EXL collaboration is to investigate light-ion induced reactions in inverse kinematics using novel storage-ring techniques and a universal detector system providing high resolution and large solid-angle coverage which allows for kinematically complete measurements. The full setup expected for this experiment comprises three main parts: a 4π detector system surrounding the internal gas-jet target, a scintillator array placed at

forward direction for neutron and fast charged-ejectile detection and an in-ring heavy-ion spectrometer for the detection of beam-like particles. A schematic view of this setup is shown in Fig. 1.1.

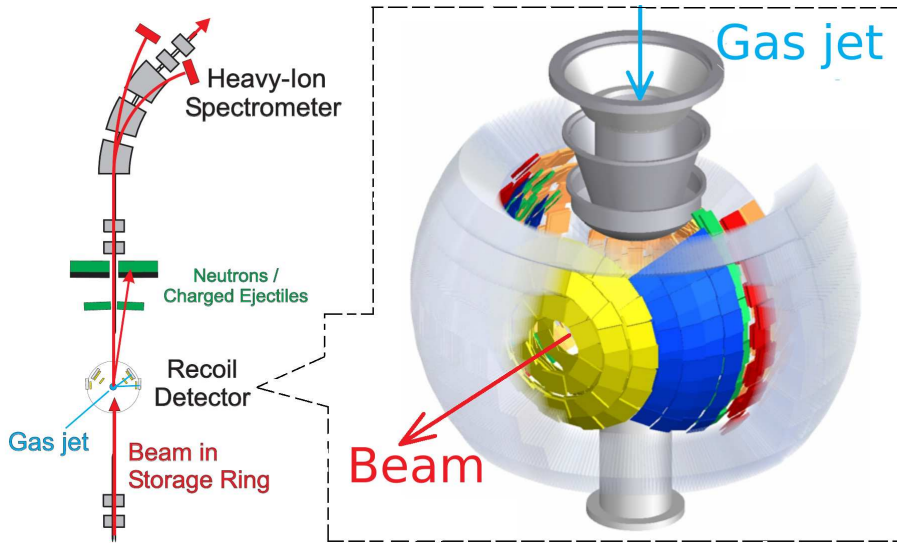


Figure 1.1.: Schematic view of the EXL detector system. On the left hand is the setup which is planned to be installed in a storage ring. On the right hand there is a zoom of the 4π detector system surrounding the gas-jet target. (Adapted from Ref.[8])

The detector setup which surrounds the internal gas-jet target is composed of two parts: an inner array of multisegmented silicon detectors (ESPA, EXL Silicon Particle Array) and an external array of CsI crystals (EGPA, EXL Gamma & Particle Array) [8]. The construction of the inner recoil detection involves some technical challenges as the detector setup has to be compatible with ultra high vacuum conditions. The solution for this problem will be, as demonstrated later, the operation of some ESPA detectors as active windows [9]. Fig. 1.2 shows a cross section through the mid plane of the recoil setup.

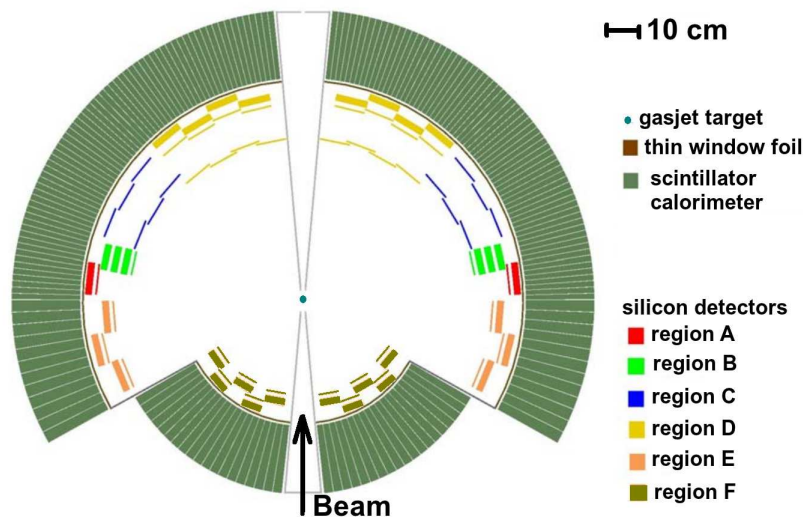


Figure 1.2.: Schematic view of the 4π detector setup surrounding the gas-jet target. The drawing corresponds to the cross section through the mid plane, seen from the gas-jet axis. (Adapted from Ref.[8])

In Fig. 1.2, the ESPA is shown as small segments in proximity to the gas-jet target which represent the manifold detector telescopes at distinct angular regions. This setup is dedicated for both the tracking

and the spectroscopy of charged particles. The ESPA is subdivided in 5 regions labeled with letters from A to F. Depending on the expected particle energies in each angular region, a different number of silicon detector layers are foreseen. On the other hand, in Fig. 1.2 the EGPA is shown as the external green detector which surrounds the ESPA. The function of this array is the detection of γ -rays emitted from excited beam-like products, as well as the residual kinetic energy of fast recoils which punch through the silicon detectors of ESPA.

The EXL project will provide a unique and versatile detector setup for the investigation of the nuclear structure of unstable exotic nuclei. Multiple types of nuclear reaction experiments in kinematically complete measurements will be possible with the full EXL setup. In Appendix B, some examples of nuclear reaction experiments which can be studied in the future with extended setups or the whole detector array will be shown.

1.2 Objectives and outline of this thesis

One of the main objectives of this thesis is the investigation of nuclear reactions in a stored-beam experiment by employing an internal gas-jet target and a sophisticated setup including ultra-high vacuum compatible detectors. For these experiments, the stable beams of ^{20}Ne and ^{58}Ni are used to study the resulting nuclear reaction channels from the interaction with the internal gas-jet targets of hydrogen and helium, respectively. Reaction channels like elastic scattering, excitation of low-lying states and giant resonances and neutron transfer were possible to be measured in the present work. In particular, the excitation of giant resonances has been investigated for the first time in a stored-beam experiment. With the analysis of the present experimental data the feasibility of this experimental technique is demonstrated by showing the consistency with experiments performed in the past in normal kinematics. From these results, our goal also is to provide a proof of principle for the EXL project which in the future will extend such techniques to study nuclei far away from the valley of stability.

Parallel to this, dedicated simulations were made in order to understand the performance of the current detector setup and the future EXL system for the investigation of distinct nuclear reaction channels. The present simulations routines are the starting point of a full simulation framework for the EXL collaboration.

The outline of this work is the following:

- **Chapter 2:** Description of the facility and the experimental setup which was utilized for the measurements of this work
- **Chapter 3:** Explanation of the offline routines applied for the raw data processing and calibrations
- **Chapter 4:** Simulation results with the present detector geometry and various reaction channels. Application of these simulations to the angular calibrations of the experimental setup and identification of reaction channels
- **Chapter 5:** Theoretical concepts and tools employed for the analysis of the experimental results of this work
- **Chapter 6:** Data analysis and results. Elastic scattering data are analyzed with distinct optical potentials from which it is possible to deduce the nuclear matter distribution. Isoscalar giant resonances are studied in an α inelastic scattering experiment. Hole-states of ^{19}Ne are investigated based on the experimental data of a neutron transfer reaction $^{20}\text{Ne}(p, d)$
- **Chapter 7:** Summary and conclusions
- **Appendix A:** Experimental studies and simulations performed for the preparation of the experiment E105. Charge and light cross-talk effects are studied by comparisons with an in-beam detector test

-
- **Appendix B:** An outlook including extended EXL detector setups is presented. Some examples of nuclear reactions are studied in simulations of the full EXL detector recoil setup

Experiment

The experimental part of this work was performed at the GSI (*Helmholtzzentrum für Schwerionenforschung*) facility, in Darmstadt (Germany), during the months of October and November of 2012. The experiment was carried out at the existing heavy-ion storage ring ESR (**Experimental Storage Ring**) using an internal gas-jet target and a dedicated detector setup compatible with the ultra-high vacuum conditions in the ring. With this system a successful EXL campaign was carried out with stored $^{56,58}\text{Ni}$ and ^{20}Ne beams. The experimental data for this thesis comprises different runs with ^{58}Ni beam and a ^4He -gas target (experiment E105) as well as with a ^{20}Ne stored beam and a H_2 -gas target (experiment E087). In this chapter some details about the preparation and execution of the experiment will be explained.

2.1 Production and acceleration of the beam

At GSI the primary beams are accelerated by a system composed of the UNILAC (**UNI**versal **LI**near **AC**celerator) and the heavy-ion synchrotron SIS18 (**S**chwer **I**onen **S**ynchrotron). The main part of the UNILAC consists of an Alvarez DTL (**D**rift **T**ube **L**inac) with two different beam injectors, the high charge state (HLI -*HochLadungsInjektor*) and the high current injector (HSI -*HochStromInjektor*). In the HLI, the beams are produced by an ECR (**E**lectron **C**yclotron **R**esonance) ion source and preaccelerated by a radio-frequency quadrupole (RFQ) system [10]. The high-current beams are delivered by a MUCIS/MEVVA type ion source. A RFQ system preaccelerates the low charge state ion beam, passing through a first stripper, to be finally injected into the UNILAC [11, 12]. In this experiment, the $^{58}\text{Ni}^{2+}$ ion beam was produced in the VARIS (a MEVVA-type) ion source with a current of about 5 *emA*. After the preacceleration and stripping, the ions were injected into the UNILAC at an energy of 1.4 MeV/u [13]. Later, in the UNILAC, the heavy ions obtain a maximal energy of 11.4 MeV/u. A diagram of the present UNILAC can be seen on the left side of Fig. 2.1.

After this point the beam passes through a second stripper (in our case obtaining $^{58}\text{Ni}^{26+}$ ions) and is transported to the synchrotron accelerator (SIS18) which has a circumference of 216 m and a maximum magnetic rigidity of 18 Tm [15]. This step provides an acceleration for the heavy ions to energies between 50 to 2000 MeV/u. Finally, the accelerated beam can be extracted to different experimental areas (e.g. the storage ring ESR), as is suggested also in the diagram of Fig. 2.1. After a slow (or fast) extraction the beam can be delivered to experiments at the caves in the target area (for producing unstable beams) to the FRS (**F**ragment **S**eparator), or be extracted into the transfer line towards the heavy ion storage ring (ESR). The intensity of the extracted beam (from the SIS) during this experiment was about 5×10^8 part./s on average [16]. In the transfer line the ions pass through a thick stripper foil where the remaining electrons are removed. From the emerging charge state distribution, the fraction of bare ions is magnetically separated and injected into the storage ring.

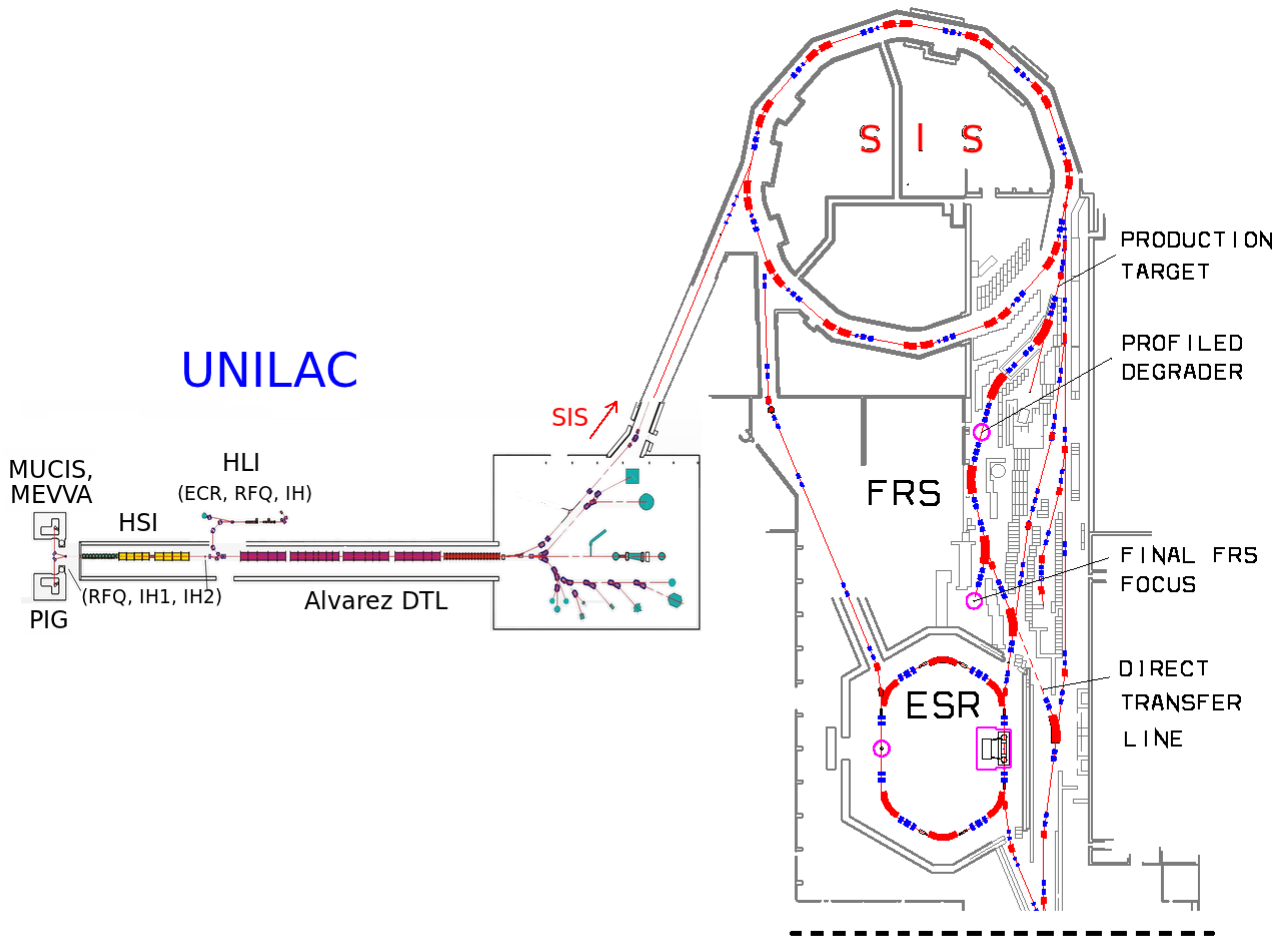


Figure 2.1.: Diagram of part of the GSI facility which is relevant for this work. On the left side, the UNILAC with its respective ion sources is presented. On the right side, the synchrotron SIS18 and the scheme of different experimental areas, like the ESR, are shown. (Adapted from Ref. [14])

2.2 The heavy ion storage ring (ESR)

The storage ring is a type of circular lattice of bending and focusing magnetic multipoles whose purpose it is to accumulate and store ions up to the highest possible currents. The ESR is capable to store ion beams from helium ($Z = 2$) up to uranium fully ionized ($Z = 92$) at velocities below 10% to almost 90% of the speed of light [17]. The ESR has a circumference of 108 m and a maximum magnetic rigidity of $B\rho = 10 \text{ Tm}$ that allows to store fully stripped ions of uranium up to the maximum specific energy of 560 MeV/u. A layout of the ESR can be seen in Fig. 2.2 with some of the important parts such as the electron cooler, RF cavities and the internal gas-jet target.

2.2.1 Stored beam

Usually, the injected beams to the ESR have a large transversal size and wide angular divergence (*hot* ions), with a typical emittance of about $5\pi \text{ mm mrad}$ [19]. These beams are efficiently *cooled* down by collisions with *cold* electrons traveling in the same direction of the beam for a distance of 2.5 m (length of the electron cooler). When the ions enter the electron cooler region, their velocity distribution is

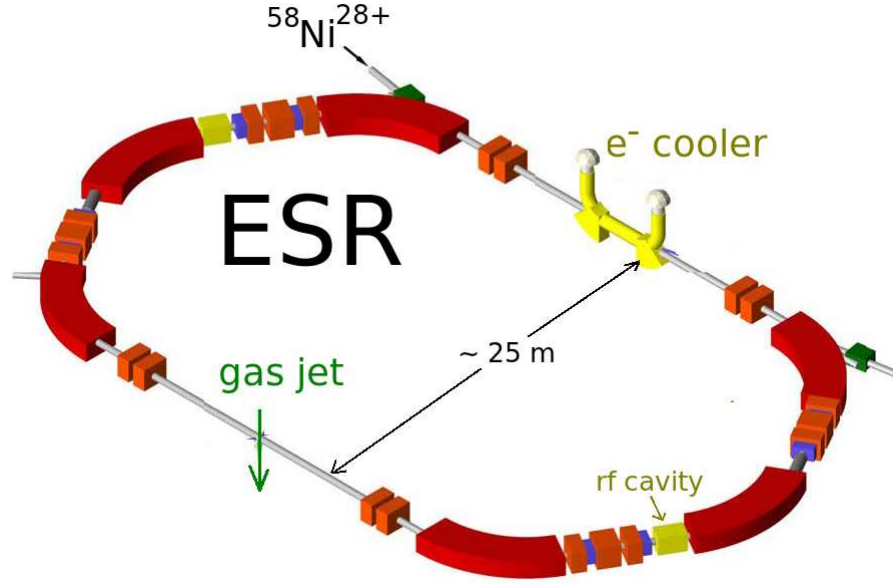


Figure 2.2.: Schematic sketch of the present heavy ion storage ring ESR at GSI. The ion beams are stored in a lattice of bending and focusing magnetic multipoles which maintain the ion circulation at frequencies around 10^6 rev./s. (Adapted from Ref. [18])

reduced and they are forced to circulate in the storage ring with a fixed velocity that is determined by the electron cooler high-voltage, U_{cooler} , as:

$$E_e^{\text{kin}} = m_e c^2 (\gamma - 1) = e U_{\text{cooler}}, \quad (2.1)$$

with

$$\gamma = 1 + \frac{e U_{\text{cooler}}}{m_e c^2}, \quad \text{and} \quad \gamma = \frac{1}{\sqrt{1 - \beta^2}}, \quad (2.2)$$

where c is the speed of light, and m_e and e are the mass and charge of the electron, respectively. This technique leads to an emittance of the stored beam of less than 0.1π mm mrad and also guarantees a well defined constant velocity with a spread in the order of $\Delta\beta/\beta \approx 10^{-5}$ [20]. This can be monitored in a non-destructive way by recording the signal which is induced by the ions in the pick-up electrodes at every turn and applying a fast Fourier transform (FFT). As result, a peak in the frequency spectrum is obtained for a specific ion species (Schottky frequency spectrum). An example of such a type of spectrum with uncooled and cooled beam samples is shown in Fig. 2.3. As one can see, the non-cooled beam has a wider frequency distribution which is related to the emittance of the beam. After few seconds of cooling, the frequency distribution of the beam is well reduced, which also means a reduction in the emittance and a better velocity definition of the stored ions.

When the electron cooling is in operation, all ions have approximately the same velocity in the ring. Thus, the revolution frequency can be expressed as:

$$f_{\text{rev}} = \frac{\beta c}{S}, \quad (2.3)$$

where S is the orbit circumference of the ions that depends on its mass-to-charge ratio (m/q) and the bending strength of the ESR magnets. That means, the revolution frequency changes for different stored-ion species or beam energies. In the present experiment, the ^{58}Ni stored-beam was run at energies of 150 and 100 MeV/u, and hence revolution frequencies were 1.4 and 1.2 MHz, respectively. For the beam

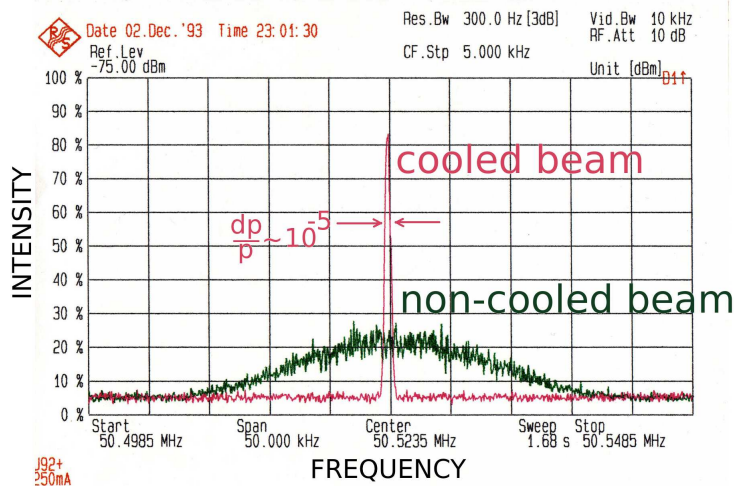
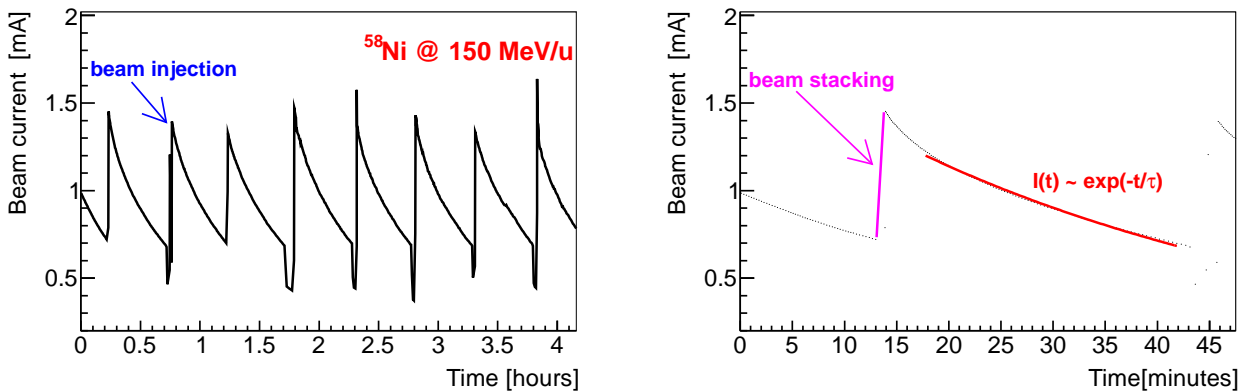


Figure 2.3.: Example of a Schottky frequency spectrum with the stored ion-beam $^{238}\text{U}^{92+}$ at the ESR. The relative longitudinal-momentum spread of the beam is reduced approximately from $\delta p/p \sim 10^{-3}$ to $\delta p/p \sim 10^{-5}$ in a few seconds. (Adapted from Ref. [20])

of ^{20}Ne at 50 MeV/u the revolution frequency was 0.9 MHz.

The beam current in the ESR is measured with a DC current transformer [21] which measures the signal induced by a time varying magnetic flux due to the beam current, similar to a flux-gate magnetometer [22]. Then, the DC signal, which is proportional to the beam current $I(t)$, is integrated during the experiment. In Fig. 2.4 the experimental beam current during a run of ^{58}Ni at 150 MeV/u is shown. In Fig. 2.4(a) one can see various sharp rises when the beam injection was done (no target) and subsequently a decay of the beam intensity during the target operation period.



(a) Different cycles of beam injection and decay.

(b) Zoom-in of one of the cycles.

Figure 2.4.: Stored beam current during the experiment of ^{58}Ni at 150 MeV/u. The sharp rises represent the different beam injections. In this case the beam lifetime was about 45 minutes.

The beam injection to the ESR is usually performed in several shots in order to accumulate enough particles in the ring to start a new run, this process is called beam stacking. The stacking of primary beams in the ESR is usually quite fast (about one or two minutes in this case) due to the high intensity in the production, but for the case of unstable ones this procedure might take an order of magnitude longer [23]. The stored-beam lifetime is highly dependent on the free path of the ions along their trajectory in the ring. Thus, the ESR environment must be as clean as possible. Usually, the operation vacuum in the

ring is about 10^{-11} mbar and 10^{-10} mbar for the target region, both in the regime of Ultra High Vacuum (UHV). However, under these conditions the ions can still capture electrons from the residual gas, the internal target or the electron cooler. Hence, atomic charge-exchange reactions are produced from the stored-beam interaction, and the total rate can be estimated as [24]:

$$\lambda = \lambda^{\text{res. gas}} + \lambda^{\text{target}} + \lambda^{\text{cooler}} = \frac{1}{\tau} \quad \text{and} \quad \lambda = \rho \cdot \sigma^{\text{ch.-ex.}} \cdot f_{\text{rev}}, \quad (2.4)$$

where τ is the beam lifetime, ρ the effective target density and $\sigma^{\text{ch.-ex.}}$ the atomic charge-exchange cross section. Therefore, the beam current can be maintained for a long time depending on the vacuum quality and also the probability for an electron pickup. The experimentally determined lifetime for the ^{58}Ni stored-beam at 150 MeV/u was about 45 minutes, which is consistent with the expectation from eq. (2.4) assuming a density of 10^{12} part./cm² and a cross section of about 10^2 barn [25].

2.2.2 Internal gas-jet target

The internal target station of the ESR is located on the opposite side of the electron cooler (see Fig. 2.2), between the two quadrupoles that focalize the ion-beam onto the interaction zone. The target is a vertical flux, perpendicular to the beam direction, of an atomic (or molecular) gas at supersonic speed. This jet is produced by expanding the gas through a nozzle of 5 μm diameter into the vacuum. The divergence of the jet is reduced by collimating the gas flux with a set of small orifices (skimmers) along its trajectory [26]. With this, the produced jet has a uniform density around the region of the interaction zone with the ion beam, and also its diameter can be fixed by the position and dimensions of the skimmers. The jet dump system is located in the lower part guaranteeing that the gas flux is pumped away from the ring without a substantial backstreaming. A schematic illustration of the internal gas-jet target is shown in Fig. 2.5. The source of the gas target is also cryogenically cooled by a continuous flow of helium making operation temperatures down to 4 K possible. At such conditions the cold gas-target expands through the laval nozzle into the vacuum and its thermal energy is converted directly into kinetic energy [26]. In particular, assuming a stationary, adiabatic and reversible expansion of a perfect gas into vacuum, the speed of this jet is given by [27]

$$v = \sqrt{\frac{2k_B T_0}{m} \frac{\gamma}{\gamma - 1}}, \quad (2.5)$$

where k_B is the Boltzmann constant, T_0 the temperature of the source, m the mass of the gas molecule and γ the adiabatic index (for a monoatomic ideal gas set to 5/3). For instance, in this experiment, the temperature of the helium target was kept at 12 K and a dynamic pressure of 3.6 bar, which resulted in a flux speed of about 354 m/s.

During the experiment, the density of the target was monitored by the vacuum gauges of the four-stage differentially pumped dump system. With these monitors, the target density at the interaction zone (n_T) can be extracted from the dump pressure, using

$$n_T \Delta z = C \frac{P_{\text{dump}}}{v}, \quad (2.6)$$

where Δz is the target thickness, $C = 4S_{\text{dump}}/(\pi k_B T \Delta x)$ and S_{dump} is the pumping speed at the dump pressure (P_{dump}), which for the case of hydrogen is about 1050 l/s and for helium 1320 l/s. In Fig. 2.6 two examples of target density during the experiment, for helium and hydrogen, are shown.

As can be noted, the target density was rather stable during the experiment. During each beam injection the gas jet was turned off to guarantee an efficient cooling and beam stacking. For this reason, in Fig. 2.6(a), it is possible to see small blank spaces in cycles of less than one hour. The average helium

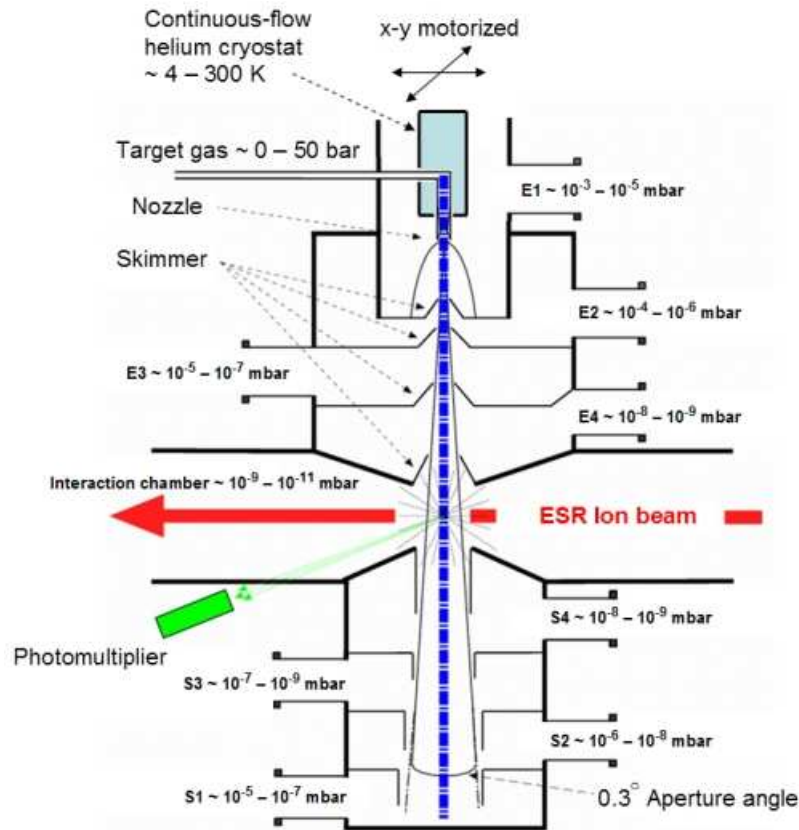
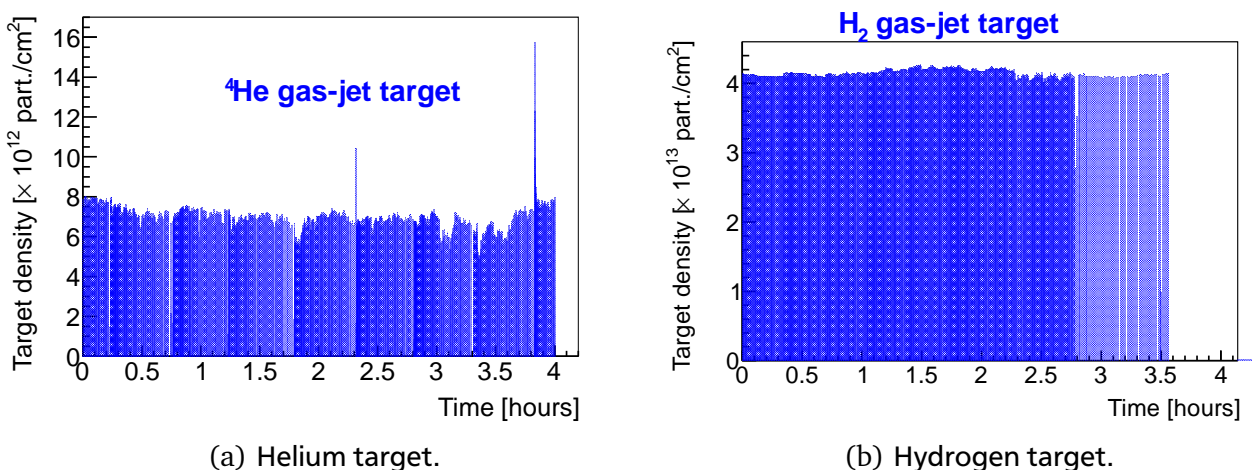


Figure 2.5.: Schematic illustration of the internal gas-jet target of the ESR. The jet source is on the top of the figure, the flow direction is downward and on the bottom the jet dump system is located. The interaction zone of the gas jet with the ion beam is represented in the middle of the flow trajectory. (Adapted from Ref. [28])



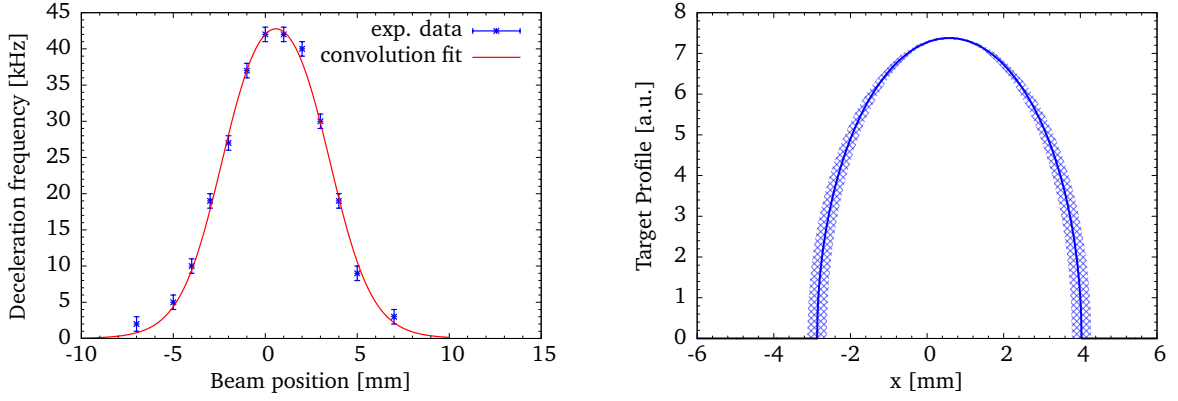
(a) Helium target.

(b) Hydrogen target.

Figure 2.6.: Target density for two different runs of the experiment. The discontinuities are due to the target flux halt during the beam injections.

target density was in the order of 10^{12} part./ cm^2 while for hydrogen it was about 10^{13} part./ cm^2 . Another important characteristic of the target is its diameter in the interaction zone which, in principle, is limited by the dimensions of the nozzle and skimmer. In our experiment we measured the target profile

by scanning the interaction zone with a low beam intensity. As the interaction of the beam with the target leads to an average energy loss, the small changes in frequency of a non-cooled stored beam can be easily measured by the Schottky frequency monitor. For this reason, the electron cooler was switched off and then the revolution frequency shift (deceleration), after a 30 s interval, was measured. To control the position of the beam, two scrapers located at 3 m in front and behind of the target region were used [29]. The experimental data points for different beam positions are shown in Fig. 2.7(a).



(a) Beam deceleration due to interaction with the internal target as a function of the horizontal (perpendicular) beam position. (b) Target profile extracted from the convolution fit given by the eq. (2.7)

Figure 2.7.: Experimental measurement of the target profile.

Given that the stored beam was not cooled in this measurement, the beam divergence is expected to be larger (see Fig. 2.3), and therefore the profile curve can also be affected. In order to unfold the beam size from this measurement, a convolution of the beam and target shapes projected on a plane perpendicular to the beam direction was fitted to the experimental data:

$$d(x) = \int_{-\infty}^{\infty} t(x')b(x-x')dx', \quad \text{with} \quad (2.7)$$

$$b(x) = A_b e^{\left(-\frac{1}{2} \frac{x^2}{\sigma_b^2}\right)}, \quad \text{and} \quad t(x) = A_t \begin{cases} 2\sqrt{r^2 - x^2} & \text{if } |x| \leq r \\ 0 & \text{if } |x| > r \end{cases}.$$

The beam is assumed to be a Gaussian ($b(x)$) with standard deviation σ_b , and the target ($t(x)$) as a projection of a cylinder of radius r and a uniform density. This shape has been used to successfully describe the target profile in measurements utilizing different methods [30, 31]. The fit was done by varying the two parameters, r and σ_b , for each numerical convolution. A global χ^2 minimum at $\sigma_b = 1.94(2)$ mm and $r = 3.45(7)$ mm was found. The target width is in good agreement with previous measurements involving different experimental setups [30, 32]. The unfolded target profile can be seen in Fig. 2.7(b).

2.3 Detector setup

In the present experiment the detector array for recoil detection was mounted in a vacuum chamber specially designed for compatibility with the UHV conditions in the storage ring. This chamber was installed in the region of the internal gas-jet target of the ESR (see Fig. 2.2). As the goal of this experiment was to measure very low energy recoils (hundreds of keV), the detector array has to be windowless and placed

within the ring environment. This is one of the most challenging parts of the technical design of this type of experiments, because, together with the detectors, connectors, cabling, and cooling system (it will be explained later) would have to be mounted in the ring environment where a vacuum in the order of 10^{-10} mbar or below is required. Such a configuration is in fact hardly feasible. An additional constraint is that for achieving such vacuum conditions in the ESR, it is necessary to increase the temperature of the chamber to a minimum value of $150\text{ }^{\circ}\text{C}$ for several days (*bakeout*) before the experiment. In order to overcome these limitations, the detector setup was installed inside internal *pockets*, where an auxiliary vacuum (AV) was operated. This provides a separation of all unbakeable and outgassing elements from the UHV of the storage ring [9, 33]. This was possible by using DSSDs (Double-sided Silicon Strip Detector) of $285\text{ }\mu\text{m}$ thickness as differential pumping barriers between the UHV of the ring and the AV inside the pockets. For the safety of these *active windows*, the differential pressure was maintained below of 10^{-2} mbar.

In the present experiment, two of these internal pockets were installed at angles of 80° and 32° with respect to the beam direction, as illustrated in Figure 2.8.

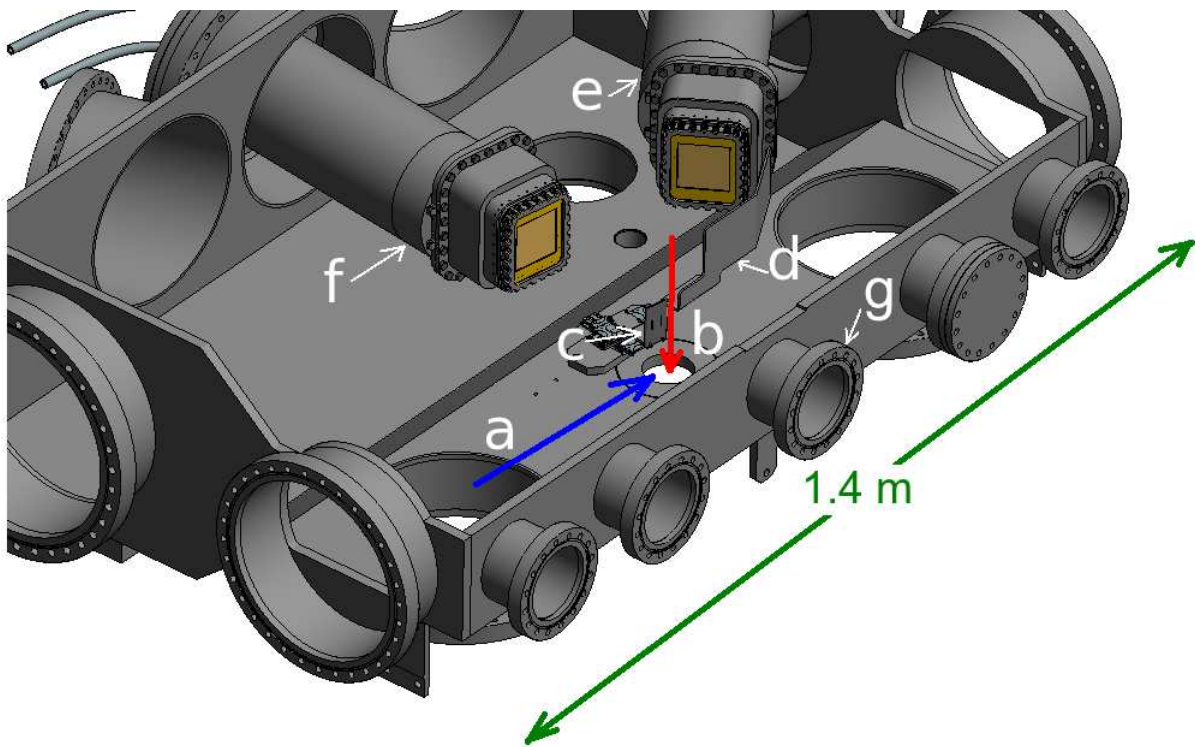


Figure 2.8.: Schematic illustration of the vacuum chamber: **a)** beam direction, **b)** gas-jet direction, **c)** slit plate, **d)** shield to prevent the detection of scattered residual-gas particles in the DSSD2, **e)** pocket 2 at 32° , **f)** pocket 1 at 80° and **g)** flange where a ^{241}Am alpha source was installed on a movable system. (Technical design by M. Lindemulder, KVI [34])

In the front part of each pocket, as mentioned before, a DSSD of $(64 \times 64)\text{ mm}^2$ in area and with 128×64 perpendicular strips was placed, also shown in the photography of Fig. 2.9(a). The distance between the surface of the DSSD1 (at 80°) and the center of the target was 250 mm, and 350 mm for the DSSD2 (at 32°). Inside the first pocket (at 80°), two Si(Li) detectors (which are unbakeable) were placed behind the DSSD in order to operate the whole system as a telescope for the detection of elastically scattered recoils. A schematic illustration of this pocket can be seen in Fig. 2.9(b). The Si(Li) detectors are 6.5 mm thick and have an active area of $(100 \times 56)\text{ mm}^2$, divided in eight quadratic pads with independent readout. The first Si(Li) (closest to the DSSD1) was mounted to cover the angles between 86° and 77° , and the second Si(Li) for the region from 82° to 73° . The challenge of using Si(Li)s in the present experiment

is that temperatures above 35 °C can irreversibly damage the detector structure, as the lithium dopant starts to drift at these temperatures [35].

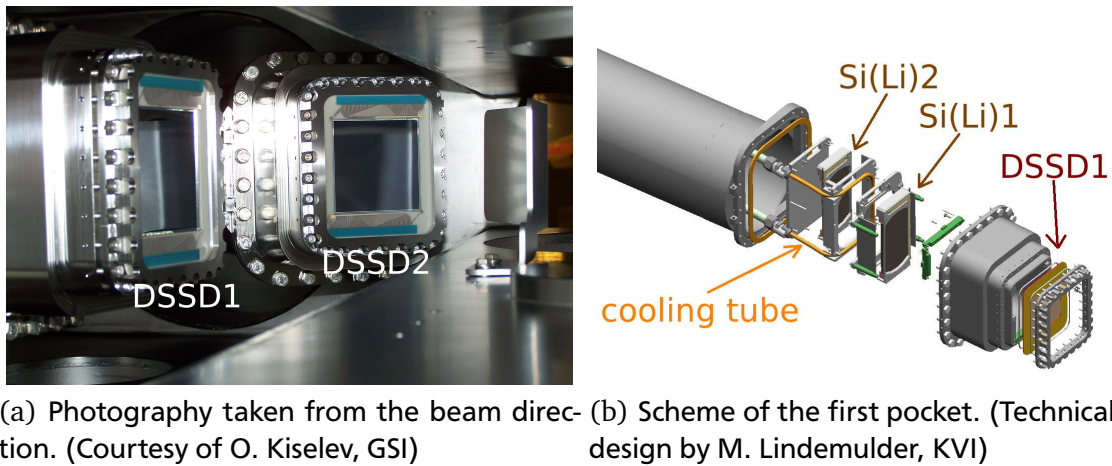


Figure 2.9.: Internal pockets seen from inside of the vacuum chamber. The photography shows the DSSDs in the front part of each pocket. The figure on the right presents the internal structure of the first pocket.

For this reason it was necessary to include a cooling system to keep the Si(Li) detectors at low temperatures, especially during the *bakeout* of the vacuum chamber. The cooling was achieved by a liquid-circulation pump connected to a copper tube that was directly in contact with the detectors, as shown in Fig. 2.9(b). The cooling liquid employed was a solution of water and ethyl alcohol (50-50%) to prevent its freezing at temperatures below 0 °C.

As the achievable angular resolution was kinematically limited by the extension of the gas-jet target, a slit plate inside the chamber was included to reduce the acceptance and thus improve the angular resolution of the telescope of pocket 1. There were two available slit apertures on this plate, 1 and 2 mm. The material chosen for the plate was tantalum with a thickness of 2 mm, sufficient for stopping the recoils in the covered angular region. This slit plate was mounted on a remote-controlled piezo motor composed by two drives, with a resolution below 1 μm , for moving the plate in two dimensions (the horizontal axes of the chamber).

The second pocket comprised only a DSSD, but this angular region is adequate for the detection of inelastically-scattered recoils at low energy. For example, in the angular range of this detector, the energy of the recoils was calculated from the kinematics to be only about 300 keV for excitation energies around 20 MeV. Also, in order to avoid a significant source of background at low energies in the DSSD2, a shielding for blocking the elastic scattering of the residual-gas particles was installed, as presented in Fig. 2.8. This shielding is a barrier of stainless steel fixed to the vacuum chamber that covers the small angle scattering (in center-of-mass system) along the beam trajectory.

For calibration purposes an alpha source of ^{241}Am was installed on a flange in front of the detectors and the target (see Fig. 2.8), with a movable system to transport the source inside or outside the chamber when it was required.

The entire experimental setup had to be *baked* for several days before the campaign in order to reach the UHV conditions necessary for the operation in the storage ring. In the following, the results of this important procedure will be presented.

2.3.1 Vacuum chamber bakeout

In order to perform the bakeout, the outer walls of the vacuum chamber were fully covered with *heating jackets* which were used to increase the temperature to a final value of 150 °C. Before this procedure

started, the cooling system of the Si(Li) detectors was set to a temperature of $-12\text{ }^{\circ}\text{C}$ with the objective to protect the Si(Li) detectors from possible damages during the bakeout. Besides various temperature probes, pressure meters and residual-gas analyzers were included in the setup for monitoring the progress of the chamber bakeout. In Fig. 2.10 some samples of the bakeout evolution can be seen, like the pressure inside the pockets, the temperature at the wall of the pocket and also at the Si(Li) detectors.

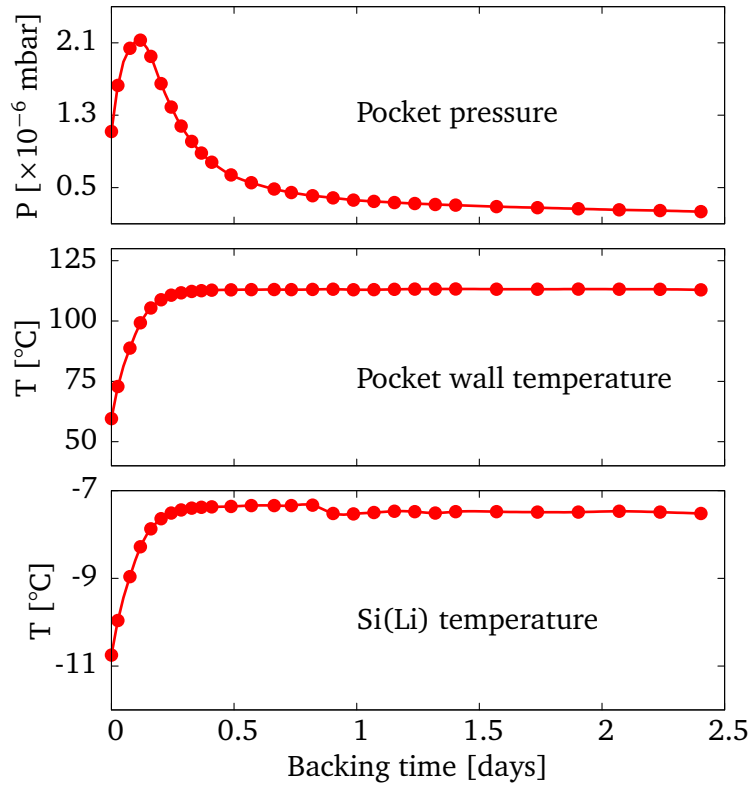


Figure 2.10.: Results of the vacuum chamber *bakeout*. In the upper part the monitoring of the pressure inside of the pockets is shown. The temperature on the walls of the pocket is presented in the middle plot. In the bottom, the temperature of the Si(Li) detectors is shown.

After the first six hours the temperature inside the chamber was already above $100\text{ }^{\circ}\text{C}$, and with this, most of the water was evaporated, bringing also a slight deterioration in vacuum, but quickly extracted by the pumping system. When the final bakeout temperature was achieved, the temperature on the detectors changed less than $5\text{ }^{\circ}\text{C}$ with respect to the initial value. This shows the significant gradient of temperature handled in the whole experimental setup during the procedure. As result, after four days of bakeout, pressures in the gas-target region of 1×10^{-10} mbar and 8×10^{-8} mbar inside the pocket system were achieved. Also, the temperature at the Si(Li) detector was kept below $-7.5\text{ }^{\circ}\text{C}$ during the bakeout, guaranteeing a good operation during the experiment.

The residual gas was analyzed using mass spectrometers monitors from which it was possible to quantify the abundance of a specific element and molecule by the relative current in the readout. Thereby, the residual-gas particles can be differentiated by their mass number. In Fig. 2.11 a spectrum of the residual-gas analysis-test (it was performed in the vacuum laboratory) after and before the bakeout process is shown.

As can be noticed, after the bakeout there is an important reduction of abundance of water, nitrogen and organic components, which finally is reflected in an improvement of two orders of magnitude in the vacuum.

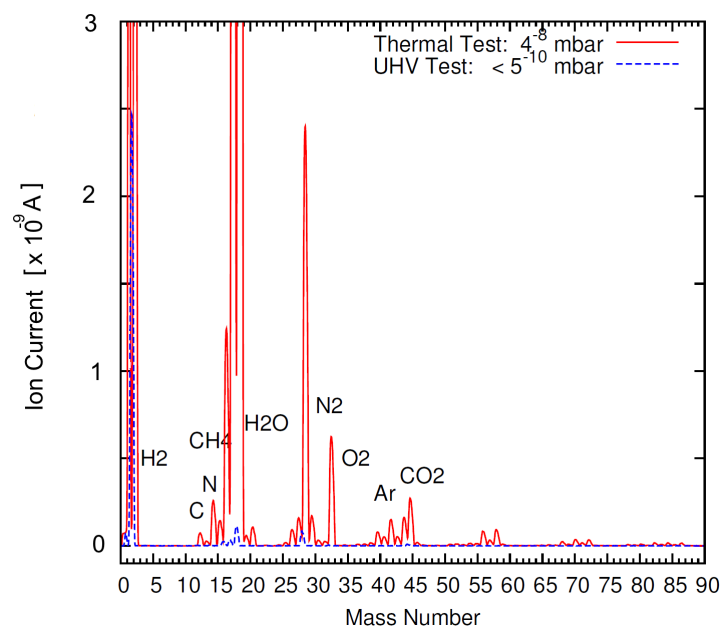


Figure 2.11.: Mass spectrometer vacuum test before (solid line) and after (dashed line) a bakeout test. The intensity of the peak is proportional to the abundance of the element (or molecule) inside of the vacuum chamber. (Courtesy of B. Streicher, GSI)



Data reduction and calibration

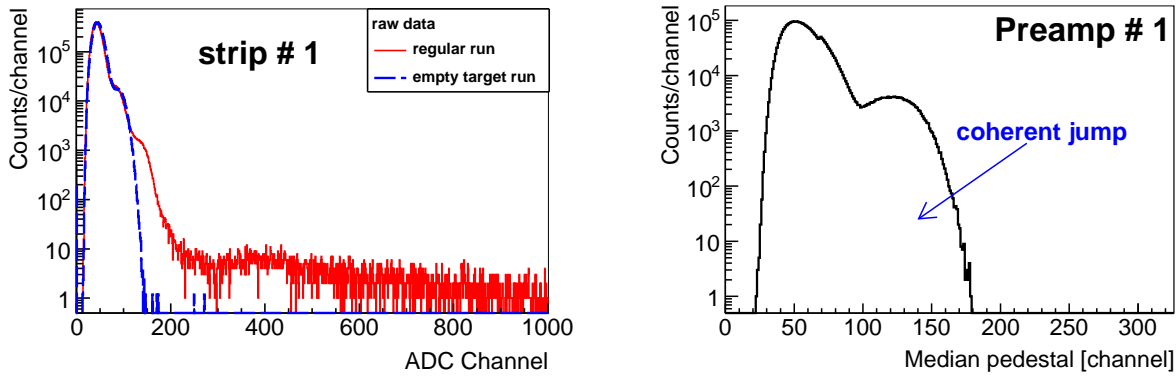
3.1 Raw data processing

As explained in Chapter 2, in the present experiment more than 300 detector channels were operated by a dedicated electronics arrangement for an individual analog-signal processing. The digital signals (from ADC, TDC or scaler) were recorded by using a data-acquisition code [36] based on the Multi-Branch System (MBS)[37]. For the off-line analysis the raw data were unpacked, sorted and saved in the ROOT format file [38] which permits a simple implementation of a data-analysis code in the C++ language. The data-analysis code that has been developed for this work includes data processing at different levels: classification, calibrations and subsequent data transformations. The first step before starting this raw data processing is to make a clear identification of the detector noise conditions, as will be shown as follows.

3.1.1 Coherent noise correction

In order to quantify the electronic background of each detector channel, various runs without the gas-jet target (empty target run) were measured during the experiment. In these runs the respective stored beam was kept in circulation for mainly two reasons: to measure the component from residual-gas scattering and to observe the influence of the ESR electric devices (in operation) to the total electronic background. In this way, it is possible to compare all these individual channel outputs with the measurements from a regular run (gas-jet target in operation). As an example, one can see in Fig. 3.1(a) the ADC output of the strip number 1 from the DSSD2, for the two cases. The empty-target run data show an irregular double-humped distribution that ends abruptly around channel 180, so all events from the target can be selected beyond this lower limit. Similarly, the regular run presents the same background structure for the first ADC channels, but its distribution is extended to higher channels. Interestingly, a comparable trend was observed in all other channels, with a much better similarity for the strips that were connected to the same preamplifier. As a naive examination of this pedestal shape, the ADC output for all strips were printed in tables for part of the run. After a careful observation, a systematic behavior was noticed. The pedestal values of the strips connected to the same preamplifier jump coherently, at certain events, by approximately the same number of channels. This is certainly an indication of a coherent noise occurrence during the experiment. The origin of such coherent noise in the silicon-strip detectors is not fully understood [39–41]. One possible source is electromagnetic pick-up from external devices, or even due to an unstable connection in the input or output signals of the preamplifiers. This effect is commonly seen in compact multichannel electronic systems as a correlation in groups of the output signals. In order to implement an off-line correction for the coherent noise, the mean distribution of all pedestals has to be analyzed in an event by event mode. One feature of the type of electronics

employed in the experiment is that the output pedestals are quite comparable among them, e.g., in the present data most of the pedestal signals were centered around channel 50 with a standard deviation of 10 channels. So, in the case of an empty-target run, the average pedestal value of all strips connected to the same preamplifier is equivalent to the mean ADC channel of an individual strip signal. However, in a regular run the conditions are different since for real events the most likely occurrence is the low channel multiplicity (only few strips are triggered), what in turn modifies the mean pedestal distribution considerably. Therefore, the most adequate statistical estimator in this case is the median (instead of the mean value). The reason is that for low multiplicity the median provides the coarse average, because the few channels with the large ADC values have no weight in the common distribution. Thus, the correction can be implemented with the calculation of the median signal \tilde{a}_k , for each event. Fig. 3.1(b) shows the median pedestal distribution from a regular run.



(a) Comparison of a strip signal for a regular and an empty-target run. (b) Median Pedestal distribution of a group of channels connected to the same preamplifier.

Figure 3.1.: Electronic background identification for the DSSD2.

In this case, only the result of one preamplifier group is presented. The main contribution is at low values, centered around channel 50, as was initially expected for the common pedestal behavior. In some events, this average pedestal position jumps to higher values what generates a second bump in this distribution. This is, in fact, the result of coherent noise pick-up. It is also interesting to see that this common tendency is very similar to the electronic background of an individual strip output (like in Fig. 3.1(a)).

A correction algorithm for the coherent noise was developed for this work, and is divided in two parts: the identification of the median pedestal distribution and the classification of the events in which this common effect occurs. In the first part of this routine, the “correct” average pedestal position, $\langle a \rangle_k$, is calculated from the dominant peak of the pedestal distribution. Hence, for each event the correction which was applied is:

$$a''_i = a'_i - \delta_k, \quad \text{with} \quad \delta_k = \tilde{a}_k - (\langle a \rangle_k + n\sigma_k), \quad \text{only if} \quad \delta_k \geq 0. \quad (3.1)$$

Here, a'_i is the uncorrected signal of the strip channel i , σ_i is the standard deviation of the main contribution of the median pedestal and n is a value which is chosen typically between 2 and 3. Then, the events in which the pedestals suffer from a sudden coherent jump (i.e. the small bump of Fig. 3.1(b)), the factor δ_k is larger than zero and all channels are commonly corrected by this value. As an example, in Fig. 3.2 the effect of the coherent correction in one of the strip signals for a regular run can be seen. Clearly, the correction suppresses the second most intense peak at low channels, and especially above channel 150 which will be important for the separability of some reaction events.

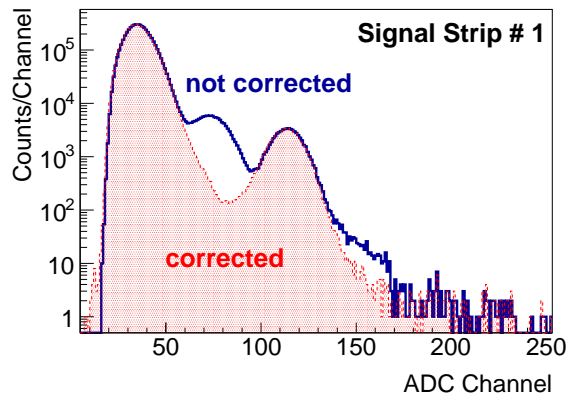
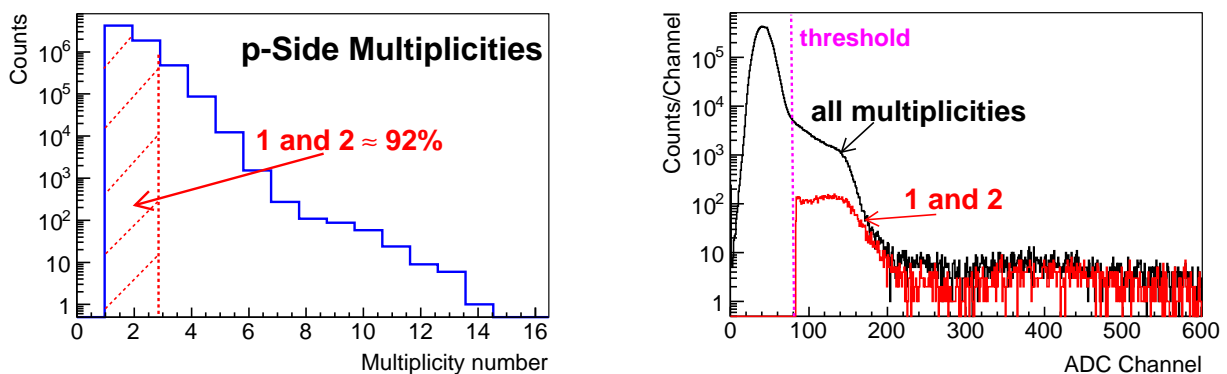


Figure 3.2.: Example of coherent noise correction for one of the strips of the DSSD2 in a regular run.

Another advantage of this correction is the possibility to apply lower threshold cuts and then to make a more efficient cluster separation, especially for low multiplicities. This can be done by performing an event discrimination from the number of strips triggered in every case. In principle, the “real” events are assumed to have a multiplicity 1 or 2 if the hit occurs in the inter-strip area (in Appendix A, inter-strip effects in DSSDs are studied). Accordingly, a threshold has to be applied to cut the noise contribution, which is composed mostly by high event multiplicities. In order to have a better understanding of this procedure, the events from a regular run have been sorted versus the number of strips triggered per event, as presented in Fig. 3.3(a). In this case, the threshold was set at the right side of the pedestal, at 2 times of the standard deviation from the centroid. The multiplicity 1 is dominant and comprises about 80% of the total events. The multiplicity 2 is an order of magnitude lower and is only accepted if the two triggered strips are first neighbors. It is clear that the efficiency of these low multiplicities depends on the position of the threshold, but at the same time the total number of events has to be the highest possible. Thus, by applying the proper threshold, the multiplicities 1 and 2 contain more than 90% of the accepted events. This percentage can be even closer to 100%, depending on the contribution of reaction channels at very low energy.



(a) Events sorted by the number of triggered strips. (b) Example of noise reduction in a strip signal by imposing only multiplicities 1 and 2.

Figure 3.3.: Event discrimination by the number of multiplicities. In this case, the *p*-side multiplicities in the DSSD2 are shown for a regular run.

In the analysis code, the multiplicities can be employed as a condition to suppress the background in all detector channels. In Fig. 3.3(b) it is possible to see how the background contribution is significantly

reduced when the condition of multiplicity 1 and 2 is applied. It is important to note that the chosen threshold position in this case seems correct, because the amount of events in the high ADC channels remains the same. The next step consists of the calibration of all digital signals, which will be explained below.

3.2 Calibrations

3.2.1 Detector calibration

As explained in Chapter 2, the energy calibration of the detectors was done with an α -source of ^{241}Am . This source was mounted on a movable arm at the opposite side of the detector pockets. In the calibration runs, the α -source was moved and placed in front of the detectors for several hours until good statistics (sufficient to resolve the energy peaks of the ^{241}Am) was achieved in all strip spectra. For the analysis of these calibration runs it was necessary to implement a routine that provides an automatic peak detection in a given histogram, and executes the respective multiple Gaussian fit. For this task, the *TSpectrum Class* of the ROOT framework was employed, which is based on the algorithm for multidimensional peak identification of M. Morhac et al. [42]. In this way, a large amount of histograms (> 500) were efficiently analyzed for the calibration runs. An energy-spectrum sample of the ^{241}Am measurement, for one of the detector strips, is shown in Fig. 3.4(a). Here it is important to note the good resolution of the DSSD detectors (better than 1%) which allows even the detection of the second most intense α -decay line of ^{241}Am at 5442 keV. Thus, by applying a fit for each individual spectrum, and after the respective pedestal subtraction, it is possible to correlate the ADC channel number with the deposited energy directly.

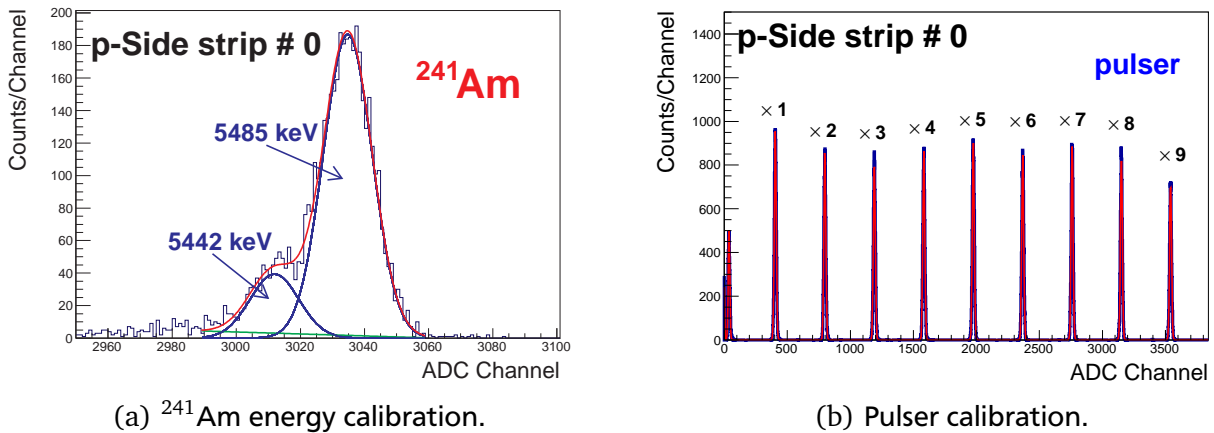


Figure 3.4.: Sample of calibration spectra for one of the detector channels.

The second part of the calibration corresponds to the linearity test of the electronics. This method allow us to extend the energy calibration along the whole ADC channel range. As usual, in this calibration a pulse generator is employed as an input signal for the preamplifiers. Initially, for each measurement, the pulse intensity was adjusted to generate a peak in the last channels of the strip spectra (around channel 3500). Later, the gain of the pulse signal was changed by a proportional factor in order to generate a second peak at a lower channel number in the spectra. This procedure was repeated several times until the whole spectrum range was covered, as Fig. 3.4(b) shows an example for one of the strips. Finally, for all spectra, a second order polynomial calibration was performed, using

$$E_{\text{pulser}}[\text{a.u.}] = a_2 \times \text{channel}^2 + a_1 \times \text{channel} + a_0, \quad (3.2)$$

where a_0 is the offset, a_1 the proportionality factor and a_2 the second order coefficient which is about six orders of magnitude lower than a_1 for every fit. These parameters are adjusted to correlate the arbitrary

units of the attenuation number with the equivalent energy position which is derived from the ^{241}Am calibration.

The third and last part of the calibration has the objective to correct the energy loss in the detector dead-layer. This type of correction improves the calibration mostly at energies below 1 MeV. The dead layer assumed for the DSSDs was 100 nm, as suggested by the detector manufacturer [43]. Accordingly, a subroutine for the particle deposited-energy calculation was implemented. This code interpolates the experimental stopping-power data (taken from Ref. [44]), and integrates the particle energy loss over the entire thickness of the dead-layer. The effective-thickness effect due to small incident angles is negligible, because as seen in Chapter 2 the DSSDs acceptance limits the particle direction in angles up to 10° , i.e. corrections of less than 2% are expected. An example of the resulting correction functions for protons and α particles with a 100 nm dead layer is shown in Fig. 3.5. As can be seen, the respective corrections are more significant for energies below 1 MeV, especially for α particles where the correction at 500 keV can go up to 26 keV. In order to implement this correction, a re-calibration of the ^{241}Am run is needed due to the 11 keV which these α particles deposit in the dead-layer. After that, the correction functions are used to return the missing energy in all spectra. The uncorrected deposited energy is assumed to be the incident kinetic energy of the particle in the detector, and then, the corresponding correction value is added individually to the detector energy of each event.

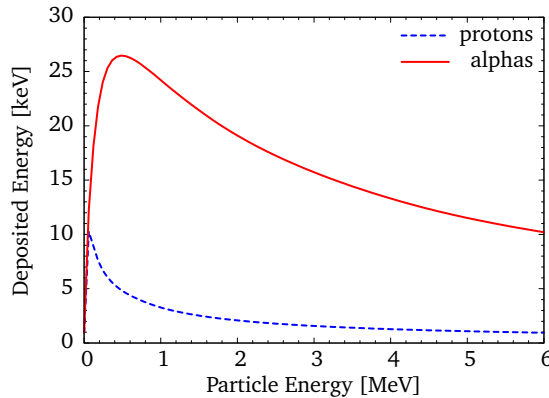


Figure 3.5.: Energy deposited for protons and α s in the 100 nm dead layer of the DSSDs.

3.2.2 Beam and target monitors

During the experiment many scalers were included in the data acquisition in order to measure different settings of the ESR. In particular, the beam current and the target density monitors were read from scalers modules at every event. However, these scaler signals also require a calibration. In the following part such procedures are explained.

Beam settings

As it was previously mentioned in Chapter 2, the beam current was monitored with a DC transformer. Similar to a flux-gate magnetometer, the integrated beam current is proportional to the input frequency signals:

$$J(t) = a \left(\frac{\text{scaler}}{t} - b \right), \quad (3.3)$$

where b is an offset and the proportional constant $a = \frac{1 \text{ mA}}{100 \text{ kHz}}$ [45]. Thus, the current can be determined in the analysis code by a numerical derivative

$$J(t) = \int_{t_0}^t I(t') dt' \quad \Rightarrow \quad I(t) \simeq \frac{\Delta J(t)}{\Delta t}. \quad (3.4)$$

The time Δt is chosen large enough (\sim seconds) in order to reduce the numerical fluctuations. Eventually, the average number of ions in the ring, at a given time t , can be also calculated as

$$N_b(t) = \frac{I(t)}{Qef_{\text{rev}}}, \quad (3.5)$$

with Q the charge state of the stored beam, $e = 1.6 \times 10^{-19}$ C, the elementary charge and f_{rev} the beam revolution frequency.

On the other hand, as the beam velocity is determined by the electron-cooler conditions, and in principle, its kinetic energy, K_b , can be deduced from the electron cooler high-voltage U_{cooler} and its current i_e :

$$K_b = m_b c^2 \left(\frac{e\tilde{U}_{\text{cooler}}}{m_e c^2} \right), \quad \text{with} \quad \tilde{U}_{\text{cooler}} = U_{\text{cooler}} - \frac{\zeta i_e}{\sqrt{1 - \left(1 + \frac{e\tilde{U}_{\text{cooler}}}{m_e c^2} \right)^{-2}}}, \quad (3.6)$$

$m_e c^2$ and $m_b c^2$ the electron and the ion beam rest mass, respectively. In this case, the electron cooler high-voltage is corrected to take the space charge effect into account, which causes a reduction of the electric potential within the beam [46]. This correction term depends on the dimensions of the electron beam and the drift tube, which results in a proportionality factor $\zeta = 1.13 \times 10^{-4} \frac{\text{kV}}{\text{mA}}$ [17, 47]. Thus, the corrected electron cooler high-voltage (eq. (3.6)) is calculated numerically and later employed for deducing the kinetic energy of the corresponding stored beam. For instance, in a ^{58}Ni run the electron cooler was set to $U_{\text{cooler}} = 82.33$ kV and $i_e = 200$ mA, which in turn defines the kinetic energy of the stored beam to be 149.99 MeV/u. Similarly, for other ^{58}Ni runs, the electron cooler was operating with the parameters $U_{\text{cooler}} = 54.71$ kV and $i_e = 50$ mA, from which the respective kinetic energy was 99.71 MeV/u.

Gas-jet target density monitor

In order to deduce the target density it is sufficient to measure the gas pressure at the dump region, as noted from eq. (2.6). Experimentally this is achieved with a system composed of four IONVAC pressure meters [48] that are labeled with S_1 , S_2 , S_3 and S_4 . The individual output of these sensors is a DC voltage u , from 0 to 10 V, which is converted to a frequency and is interpreted by scaler as

$$\frac{\Delta \text{scaler}}{\Delta t} = 10^{\left(\frac{u+2}{2.5} \right)}. \quad (3.7)$$

This voltage is related to the pressure by a calibration function provided by the manufacturer [48]

$$P[S_i] = \begin{cases} 10^{\left(\frac{u-7.75}{0.75} \right)} \text{ mbar} & \text{for } S_1 \text{ and } S_2 \\ 10^{(u-12)} \text{ mbar} & \text{for } S_3 \text{ and } S_4 \end{cases}, \quad (3.8)$$

and hence, the total pressure at the dump can be obtained with

$$P_{\text{dump}} = k_{\text{gas}} \sum_{i=1}^4 P[S_i], \quad (3.9)$$

where k_{gas} is a conversion factor used for gases other than air. For example, with hydrogen $k_{\text{H}_2} = 2.4$, and helium $k_{\text{He}} = 5.9$. The uncertainty associated to the present measurements is about 15% [48]. Using all the above, the internal gas-jet density is calculated in the analysis code, at any P_{dump} read-out, with the expressions:

$$(n_{\text{T}}\Delta z)^{\text{H}_2} = \left(1.91 \times 10^{18} \frac{1}{\text{mbar}}\right) P_{\text{dump}} \frac{\text{part.}}{\text{cm}^2} \quad (\text{Hydrogen}), \quad (3.10)$$

$$(n_{\text{T}}\Delta z)^{\text{He}} = \left(2.24 \times 10^{18} \frac{1}{\text{mbar}}\right) P_{\text{dump}} \frac{\text{part.}}{\text{cm}^2} \quad (\text{Helium}). \quad (3.11)$$

3.3 Determination of luminosity and cross section

3.3.1 Luminosity

The luminosity is the density of collision centers in the target multiplied by the number of particles colliding with this target per unit time. By definition the luminosity is given by the ratio of the event rate (\dot{Y}) with the cross section (σ) of a particular event [49]

$$\mathcal{L} \equiv \frac{\dot{Y}}{\sigma} = \frac{1}{\sigma} \left(\frac{d}{dt} Y \right). \quad [\text{cm}^{-2}\text{s}^{-1}] \quad (3.12)$$

Usually, for stored-beam experiments, the luminosity is expressed as the product of the beam revolution frequency and the luminosity of a single collision (\mathcal{L}_{sc}), $\mathcal{L} = f_{\text{rev}}\mathcal{L}_{sc}$ [50]. Assuming a fixed target (because the velocity of the gas-jet is negligible in comparison to the beam velocity v_{beam}), this single-collision luminosity can be approximated by the overlap integral ¹

$$\mathcal{L}_{sc} \approx \Delta z \int n_{\text{T}}(r)n_{\text{B}}(r)d^3r, \quad [\text{cm}^{-2}], \quad (3.13)$$

where Δz is the target thickness and $n_{\text{T(B)}}$ are the particle volumetric-density of the target (T) and beam (B). As it was shown experimentally in Chapter 2, a good approximation for the internal gas-jet target is an uniform cylinder with constant density n_{T} . In this case, eq. (3.13) is reduced to the calculation of the number of beam particles involved in this single collision. In a first approximation we can assume that all stored particles in the ring are concentrated in a single bunch, so the number of beam particles involved in a single collision is equal to N_{b} (eq. (3.5)). Therefore, the luminosity in a given time t can be finally expressed as

$$\mathcal{L}(t) = \alpha f_{\text{rev}} \times N_{\text{b}}(t) \times (n_{\text{T}}\Delta z)(t) = \frac{\alpha}{Qe} \times I(t) \times (n_{\text{T}}\Delta z)(t). \quad (3.14)$$

However, this simple approximation overestimates the experimental luminosity and usually a correction factor α is needed. The correction factor can be found from a relative normalization with a luminosity monitor. For instance, by measuring the deflected ions from the central beam orbit due to atomic charge-exchange, or by detecting of the ultra-violet light produced in the beam-target interaction zone [52]. In this work a relative normalization with the elastic scattering for the most forward angles ($\theta_{\text{cm}} < 3^\circ$) was employed. Moreover, the time dependence of eq. (3.14) obeys to the variation of the beam current

¹ From the expression of Ref. [51], we can assume that the densities do not change during the single collision.

and the target density during the experiment, as can be seen in Figs. 2.4 and 2.5. Nevertheless, for the analysis of the experimental data it is convenient to use the integrated luminosity

$$\mathcal{L}_{\text{int}} = \int_0^{t_f} \mathcal{L}(t) dt = t_f \times \langle \mathcal{L}(t) \rangle_{\text{ave}} = \frac{\alpha}{Q_e} t_f \times \langle I(t) \times (n_T \Delta z)(t) \rangle_{\text{ave}}, \quad (3.15)$$

where t_f is the time elapsed for the whole run and the brackets $\langle \rangle_{\text{ave}}$ represent the average value². Thus, the corresponding luminosity of a given run is deduced directly from the average value of the product of the beam current and the target density. The uncertainty of this mean luminosity is divided in three independent components: statistical, instrumental and one part from the normalization

$$\varepsilon(\mathcal{L}) = \sqrt{(\varepsilon_{\text{stat}})^2 + (\varepsilon_{\text{instr}})^2 + (\varepsilon_{\text{norm}})^2}. \quad (3.16)$$

The main error contribution in the luminosity measurement is produced by the target density due to the uncertainty of the pressure meters ($\sim 15\%$).

In the experiment with the ^{20}Ne stored-beam and the internal gas-jet of hydrogen the average luminosity was $6.1(9) \times 10^{27} \text{ cm}^{-2}\text{s}^{-1}$. In the case of the ^{58}Ni stored-beam at 150 MeV/u with the helium target, the corresponding mean luminosity was $3.9(6) \times 10^{26} \text{ cm}^{-2}\text{s}^{-1}$. For the runs of 100 MeV/u (with same target and beam) the luminosity was smaller, $6.3(9) \times 10^{25} \text{ cm}^{-2}\text{s}^{-1}$, since a significant reduction in the beam intensity occurred because of its deceleration within the ESR.

3.3.2 Cross section

The differential cross-section measured in the laboratory frame is calculated using³

$$\left(\frac{d\sigma}{d\Omega} \right) (\theta_{\text{lab}}) = \frac{Y}{\mathcal{L}_{\text{int}} \Delta\Omega_{\text{lab}}} \times 10^{27}, \quad [\text{mb/sr}] \quad (3.17)$$

where Y is the total number of events registered in the detector which was placed at a laboratory angle θ_{lab} and covering the solid angle $\Delta\Omega_{\text{lab}}$. Here, the factor 10^{27} is included to change the unit cm^2 to millibarns (mb). In order to deduce the correct solid angle acceptance for each detector strip, a correction in the relative position of the detectors is needed. In this work, simulations are employed to derive these correction functions and the respective solid angles, as explained in Section 4.2. Moreover, in scattering theory often the representation in the center-of-mass system is employed, because in this frame normal and inverse kinematics are equivalent. The respective transformations to the center-of-mass system were performed with a relativistic two-body-kinematics code which is based on the Mandelstam variables formalism [54]. Therefore, the experimental differential cross section in the center-of-mass frame is given by

$$\left(\frac{d\sigma}{d\Omega} \right) (\theta_{\text{cm}}) = \frac{Y}{\mathcal{L}_{\text{int}} \Delta\Omega_{\text{lab}}} J \times 10^{27}, \quad [\text{mb/sr}] \quad (3.18)$$

where

$$J \equiv \frac{d\Omega_{\text{lab}}}{d\Omega_{\text{cm}}} = \frac{d(\cos \theta_{\text{lab}})}{d(\cos \theta_{\text{cm}})}. \quad (3.19)$$

This factor J is the Jacobian of the transformation that can be calculated directly from the particle kinematics. Finally, for the calculation of the errors of the cross section, we assumed three independent components

$$\partial \left(\frac{d\sigma}{d\Omega} \right) = \left(\frac{d\sigma}{d\Omega} \right) \times \sqrt{\left(\frac{\partial Y}{Y} \right)^2 + \left(\frac{\partial \mathcal{L}}{\mathcal{L}} \right)^2 + \left(\frac{\partial(\Delta\Omega)}{\Delta\Omega} \right)^2}. \quad (3.20)$$

² Due to the mean value theorem [53]

³ By integrating eq. (3.12) with respect t .

As could be seen in the previous section, the main contribution is the uncertainty of the average luminosity which is about 16%. The error in the solid angle is derived from the squared root of the accepted events in the simulation (see Chapter 4), in all cases it was lower than 5%. The statistical error due to the total number of events registered in the detector, Y , is more significant around the minima of the cross sections, where its value can be up to 15%.



Simulations

Nowadays, simulations are an essential part in experimental nuclear-physics research. Their applications range from the design of complex detector setups up to the realistic estimation of detector output signals. In this work we have used GEANT4, which is a toolkit written in the C++ object-oriented language for the simulation of the particle transport and its interaction with matter [55]. That toolkit has a great versatility to make or import complicated geometries and to create any kind of projectile or target. Therefore, it is an appropriate tool to simulate new detector systems and/or study the setups under development, as required for the EXL project. The EXL detector setup is an ambitious project that requires a lot of work in detector development and techniques for operation under diverse environments. In this case, the simulations are an important tool that may help us to understand many issues about the experimental performance of the newly designed detector systems. In the past several years, the EXL collaboration has performed a large amount of experimental research of detector responses under different conditions. For the present work, various of these setups are simulated, showing a way to study detector correlations and their applications for in-ring experiments. For the preparation of the present experimental work, simulations of an in-beam experiment test are studied and are shown in Appendix A. Such results were particularly important to understand the cross-talk effects in some of the detectors planned to be used in the EXL project. Similarly, in Appendix B simulations of future detector setups of the EXL project are studied. The present chapter is dedicated to the simulations of the experimental setup which have already been explained in the Chapter 2. These simulations were extremely helpful during the analysis of the experimental data. In the first part of this chapter, the geometry, particle generator and the slit plate simulations will be discussed. Later, the simulated detector geometry is employed to perform the angular calibrations of the experimental data. Finally, different reaction channels are simulated in order to understand the experimental energy spectra in the DSSD2.

4.1 Simulated geometry and the event generator

As it was previously explained in Chapter 2, the experimental part of this work was carried out in the ESR storage ring with ^{58}Ni and ^{20}Ne ion beams, and the internal gas-jet targets of helium and hydrogen. The recoil detector-geometry consisted of an array of two DSSD and two Si(Li) detectors mounted in a especially designed vacuum chamber for UHV compatibility that was installed in the internal gas-jet target region (see Fig. 2.8 and Fig. 2.9). In order to create a more realistic scenario of this setup in our simulations, the detector elements were constructed and placed inside of a stainless steel chamber whose geometry was imported from a simplified CAD drawing [34] of the original design using the interface class CADMesh [56]. Based on our measurements of the target profile (shown in Fig. 2.7) and other experiments [30, 32], the gas-jet target was assumed as a vertical cylinder with uniform density and a radius of 3.45 mm. Additionally, to simulate realistic dimensions of the cooled beam at the interaction zone, the systematic measurements of Ref. [57] with different beam species and intensities at the ESR

were employed. Thus, the simulated interaction volume for the primary events is limited by the superposition of these target and beam distributions.

The primary events in our simulations were generated for a specific reaction channel using a function that takes into account the relativistic reaction kinematics for two and three bodies in the output channel. This function is based on the particle kinematics formalism that is explained in detail in Ref. [54]. Hence, the use of this routine allows to generate the recoils coming from different reaction channels, e.g.: elastic and inelastic scattering, transfer, breakup, knockout, etc. Its implementation is done in the *Primary Event Generator* class of the simulation, where the particles are created with a specific kinetic energy and direction. Another option of this particle generator is the possibility to produce the events with a given probability distribution, e.g., a differential cross section. This can be done with the standard Monte Carlo method, as

$$r = \frac{\int_{\theta_1}^x \left(\frac{d\sigma}{d\Omega}\right)_{\text{lab}} 2\pi \sin \theta d\theta}{\int_{\theta_1}^{\theta_2} \left(\frac{d\sigma}{d\Omega}\right)_{\text{lab}} 2\pi \sin \theta d\theta} \quad ; \quad r \in [0, 1] \longrightarrow x \in [\theta_1, \theta_2], \quad (4.1)$$

where r is a uniform random variable and x is a variable distributed by the respective cross section. Usually, the cross sections are extracted from external codes for nuclear reaction calculations in numeric tables format [58–61]. Complementarily, a cubic interpolation subroutine is also included for a smooth evaluation of eq. (4.1) in the defined angular range. Also, the respective transformations from center-of-mass to laboratory system for inverse kinematics are applied at the beginning of the simulation.

For example, we can explore the results of our simulations including the kinematics and the respective cross section for the reaction $^{58}\text{Ni}(p, p)$ at 400 MeV/u (beam energy). Because of the inverse kinematics, the elastically scattered recoils at laboratory angles close to 90° correspond to very forward angles in the center-of-mass system ($\theta_{\text{cm}} \rightarrow 0^\circ$). In this case, it is clear to focus our simulation on the pocket 1 that, as it was mentioned in the Chapter 2, was placed at an angle of 80.5° (with respect to the beam axis) with a telescope formed by a DSSD and the two Si(Li) detectors. In Fig. 4.1 one can see the simulation results of elastically scattered protons detected in pocket 1.

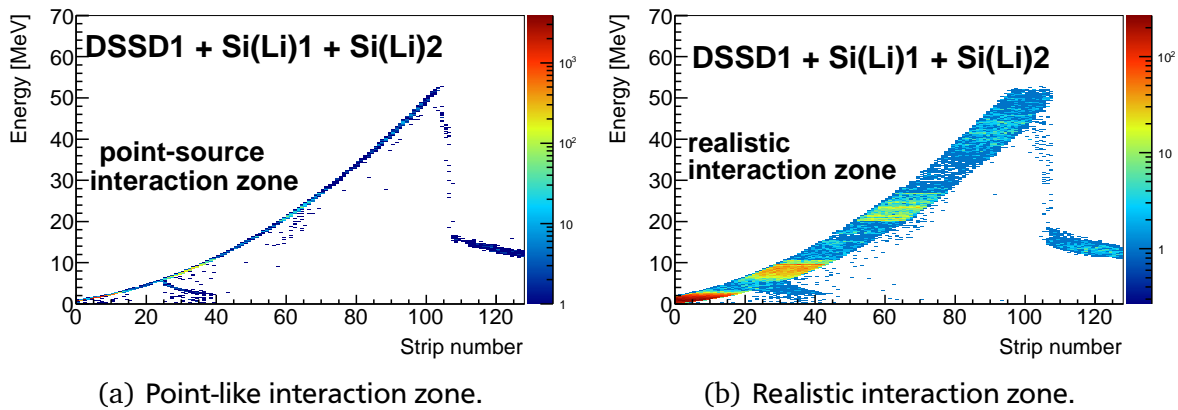


Figure 4.1.: Simulation of elastic scattering of $^{58}\text{Ni} + p$ at 400 MeV/u. The recoils are detected in the telescope system of pocket 1 (at $\theta_{\text{lab}} = 80.5^\circ$) which comprises a DSSD and two Si(Li) detectors. For this simulation we have assumed two distinct cases for the beam-target interaction zone: a point-like type and an extended distribution with realistic dimensions.

The x -axis corresponds to the vertical strip number of the DSSD, that is proportional to the laboratory polar-angle (in this case the strip number 0 is closer to 90°). The y -axis is the total energy deposited in the three detectors. In order to see the effect of the target and beam dimensions on the detected angular resolution, a realistic and a point-like interaction zone are simulated. In Fig. 4.1(a) it is possible

to observe the small contribution of the strip size to the angular resolution, about 0.1° in the laboratory system. When the realistic dimensions of the beam and target are included into the simulation (see Fig. 4.1(b)), the resulting kinematics plot presents a more extended distribution, approximately 10 times larger than in the point-like source case. As the strip number is proportional to the polar angle, the angular resolution expected for such an experiment is around 1° in the laboratory system. Therefore, the angular resolution is limited by the size of the interaction zone and not by the pitch of the strips. The physical reason for such a large angular resolution is the extension of the beam and target interaction volume. Mainly, the gas-jet target diameter (see Section 2.2.2) allows the event generation over an extended region which is reflected in a deterioration of the detected angular resolution, even with a small strip width (like in the present case). This problem can be solved by including a slit aperture that collimates the scattered particles in the angles covered by this telescope. Below we will study this element in more detail.

4.1.1 Slit aperture simulations

As mentioned above, the extended beam-target interaction volume has a direct consequence in the coarse angular resolution for the detected particles. This is a limitation if we are interested in measuring a particular reaction channel that demands a precise angular resolution and/or a good separation of other reaction channels. For instance, as one of the goals in this experiment, we want to extract the nuclear matter density by measuring the angular distribution for elastic scattering, but to obtain accurate results it is crucial to have a good knowledge of the laboratory angle and separability from the inelastic channels. One way to improve the angular resolution is by including a slit plate to reduce the angular acceptance and constrain the detection to scattered particles from a part of the interaction volume only. For this reason, the slit plate is mounted in between the gas-jet target and the detectors, at proximity to the interaction zone in order to illuminate the entire detector area. In Fig. 4.2 a schematic illustration of the slit plate mounted in front of pocket 1 (at $\theta_{\text{lab}} = 80.5^\circ$) is shown.

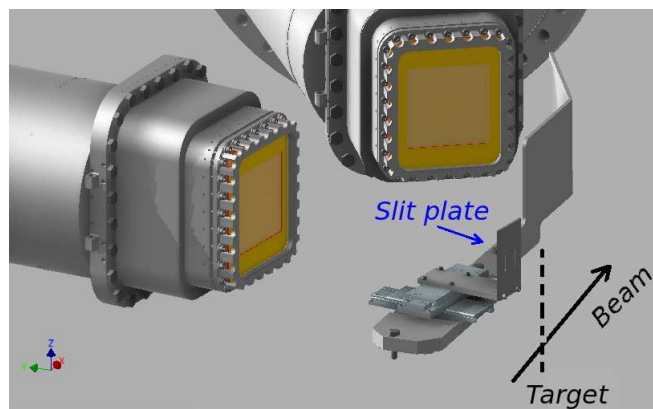
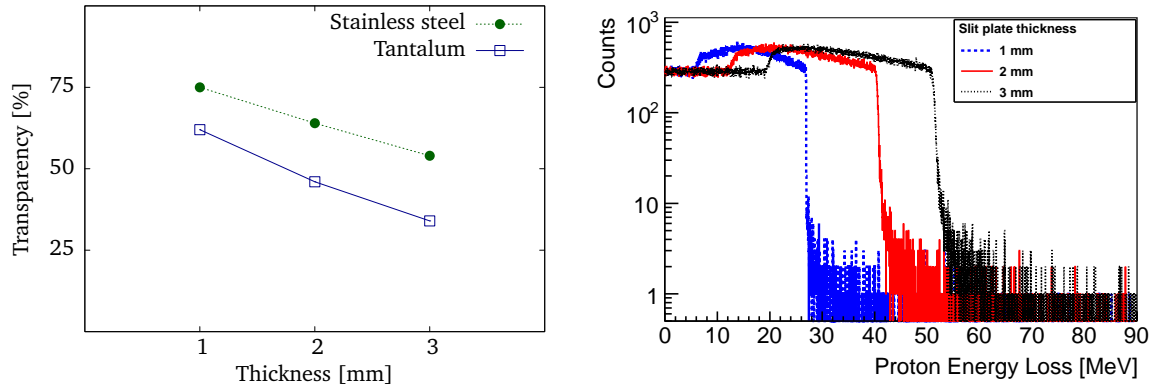


Figure 4.2.: Illustration of the slit plate geometry placed in front of pocket 1. (Adapted from the technical designs by M. Lindemulder, KVI)

This device must be well separated from the target in order to not interfere with the gas flow, where the limit has to be around three times the target radius (approx. 10 mm). Experimentally, this distance was fixed to 30 mm.

During the preparation for the experiment, one of the important tasks addressed by simulations was to design the slit plate. Beforehand, it was known that the material for the construction of this device should fulfill three requirements: machinable, UHV compatible and high stopping power. A natural material could be stainless steel, which is the main component of the vacuum chamber. However, few millimeters of this material are not enough to stop high energy protons completely. A more dense material that also fulfills the requirements is tantalum. It was important to know the needed thickness of

the plate in advance because its construction price might be high. In order to solve this, simulations of the plate for both materials with impinging protons at uniform energies in the range of $0 < E_p \leq 100$ MeV were performed. As we can see in Fig. 4.3(a), the tantalum material is more efficient in stopping the protons at such energies than stainless-steel, because the percentage of protons punching through the plate is smaller (“transparency”). If this material is used, we can stop about 20% more particles than with a stainless-steel plate with the same thicknesses.



(a) Percentage of protons that punch through the plate. (b) Stopped protons in the tantalum plate for different thicknesses.

Figure 4.3.: Simulation results for the slit plate assuming a proton source with uniformly distributed energies from 0 to 100 MeV.

Also, we studied the number of stopped protons in the tantalum plate at different thicknesses (Fig. 4.3(b)). Protons with energies above 28 MeV punch through the 1 mm plate, while for the 2 mm one it happens only above 42 MeV, and the 3 mm plate still can stop protons at energies below of 58 MeV. In order to decide which thickness is more suitable for the experiment, we included a more realistic proton source including also the elastic cross section, as shown in Fig. 4.1. With such a simulation we can predict that in the real experiment, with a slit plate of tantalum of 2 mm thickness, about 98% of the protons that hit the slit are blocked. Now the question is what are the consequences in the energy spectra when the slit plate is used? For instance, we can see the contrast of the simulation without slit plate (Fig. 4.1(b)) and the ones including this volume with two different aperture widths (1 and 2 mm), as presented in Fig. 4.4.

The resolution of the elastic kinematic line is tremendously improved and the trend is more noticeable when the slit aperture is smaller. However, the background from particles scattered on the slit plate is significant, especially around the minimum of the cross section. Another constraint when employing the slit plate is concerning the attenuation of the total detected events per strip. The 2 mm wide slit leads to an attenuation factor of 4, while the 1 mm one reduces the total amount of detected events by a factor of 8. This means, the experimental measurements have to be done for longer time in order to reduce the statistical errors.

On the other hand, the angular resolution and separability of reaction channels can be studied by adding to the simulations the first excited state of ⁵⁸Ni, the 2₁⁺ state at excitation energy $E_x = 1.45$ MeV, which is the next most intense channel in the angular region of pocket 1. In order to investigate this we compared the simulated energy spectra per strip with different slit apertures, as shown in Fig. 4.5.

In the simulation without the slit plate, the corresponding energy spectra are composed by broad and skewed peaks, from which it is not possible to distinguish between the contributions of elastic scattering and the excitation of the first excited state. This asymmetry in the energy peaks is caused by the large angular acceptance that allows the detection of many recoils produced at small angles in the center-of-

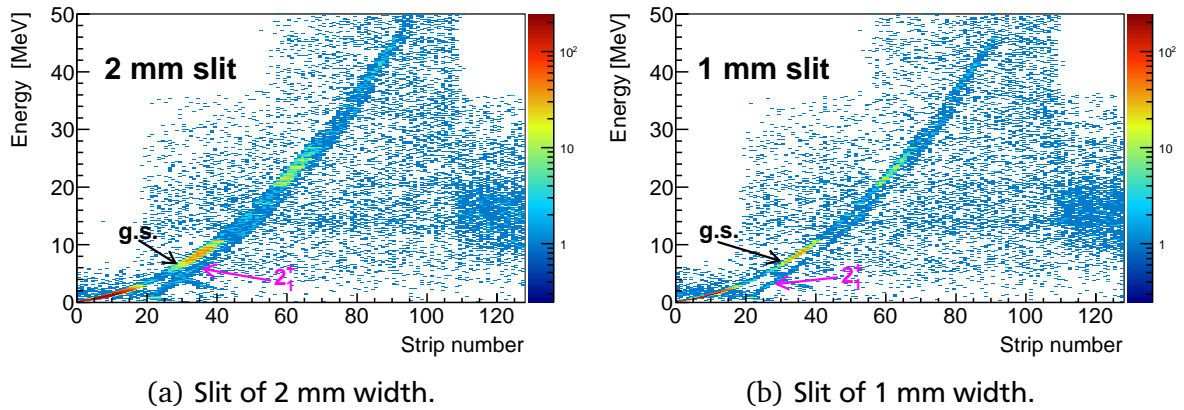
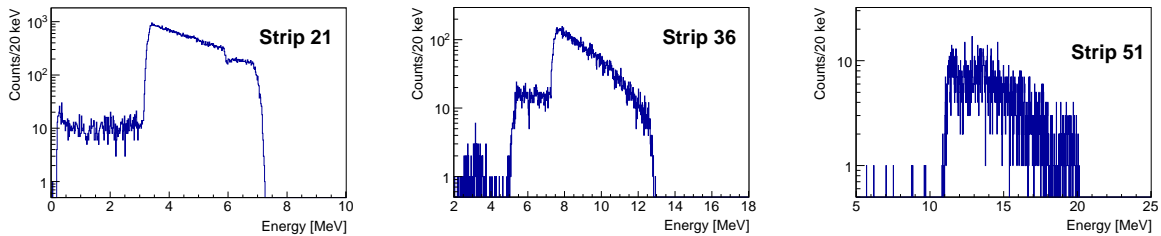
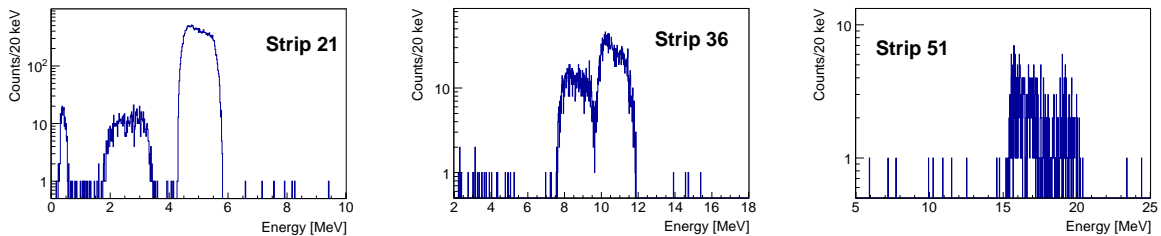


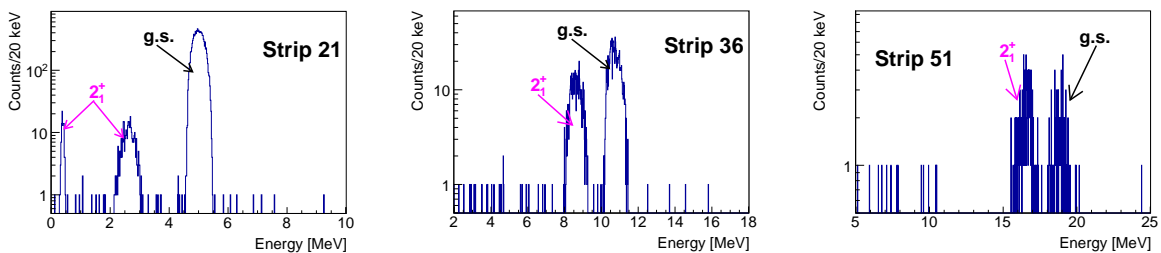
Figure 4.4.: Simulated energy spectrum of pocket 1 including the elastic scattering and the first excited state in the system $^{58}\text{Ni} + p$ at 400 MeV/u. The slit plate was employed in two cases: 1 mm and 2 mm aperture.



(a) Without slit plate, strip 21. (b) Without slit plate, strip 36. (c) Without slit plate, strip 51.



(d) 2 mm slit, strip 21. (e) 2 mm slit, strip 36. (f) 2 mm slit, strip 51.



(g) 1 mm slit, strip 21. (h) 1 mm slit, strip 36. (i) 1 mm slit, strip 51.

Figure 4.5.: Sample of the simulated energy spectra for various strips and slit apertures. On the top are the results without slit plate. The spectra from the middle correspond to the simulation with a slit width of 2 mm, and on the bottom for a 1 mm slit width.

mass system. For the simulation with a 2 mm slit, it is possible to identify two peaks, one on the right side that belongs to the elastic scattering contribution and the other from the inelastic one. It is still

possible to observe a slight asymmetry in the energy peaks, but not as major that it would compromise the distinction of the two reaction channels. Finally, for the simulation of the 1 mm slit, the peaks are symmetric and better defined. In this case the elastic scattering is easily separable from the first excited state in each strip. For a better visualization of the above mentioned it is convenient to define a parameter that quantifies the separation between peaks [62]

$$\alpha = \frac{\mu_1 - \mu_2}{2(\sigma_1 + \sigma_2)}, \quad (4.2)$$

where μ denotes the centroids, σ the standard deviations and the subscript 1(2) elastic (inelastic) peaks. When this parameter is larger than 1 the peaks are totally separated, but for lower values the peaks are overlapping and the distance between the centroids is less than twice the standard deviation for each peak. In Fig. 4.6(a), we can see that the separability for the 2 mm slit is affected starting at strip number 36 and above, however, for the 1 mm slit, the elastic and inelastic scattering contribution are not mixed in these detectors. As we have seen, the peak separation becomes more difficult in the last strips because their widths are also increasing. In Fig. 4.6(b) it is possible to see the standard deviation of the elastic scattering peaks for the two slit apertures studied. The increase of the energy resolution is due to a rapid growth of the proton kinetic energy with the polar angle what finally produces a dispersed energy loss distribution in the detectors.

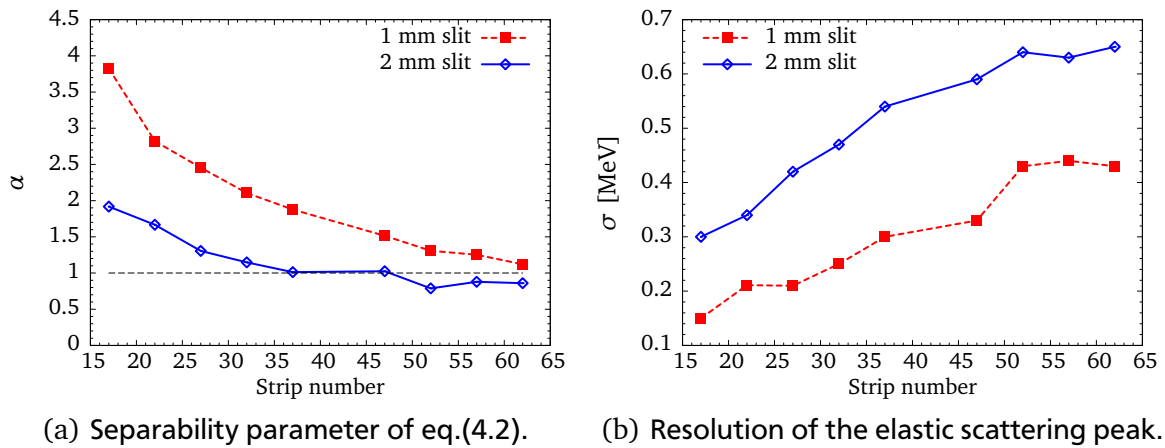


Figure 4.6.: Elastic and inelastic peaks separability for different slit apertures.

4.2 Angular calibrations

In this section, some of the simulations used for the experimental data analysis, like the angular corrections and numerical calculations for the angular acceptance, are explained. For this task, one of the simplest ways to check the nominal angular calibration for the detector setup is to compare the energy-angle correlations of the experimental elastic scattering with the simulation. Since the kinematics of elastic scattering is well known and the position of the detectors is supposed to be the same as in the designs, the discrepancies which are expected in these comparisons are mainly due to small misalignments in the experimental setup. Naturally, our simulations must be made with the same geometry provided by the technical designs of the vacuum chamber and other devices [34]. For this purpose, experimental data of elastic scattering that was measured in the present campaign was used. For a proper comparison, experimental runs with and without the slit plate are needed. Therefore, the most adequate runs in this case are the proton elastic scattering experiments with the beams ^{20}Ne (at 50 MeV/u) [63] and ^{56}Ni (at 400 MeV/u) [23, 36]. Initially, we are interested in the measurements made without the slit plate in order to verify the correct geometry of the experimental setup. In Fig. 4.7, the experimental

elastic scattering is compared with simulations that were performed with the same geometric setup as in the technical drawings. Here, the experimental kinematic plot is presented as black dots and the simulation results are shown in color. In the comparison of the DSSD1 energy spectrum it is possible to observe a small offset in the strip number between experiment and simulation. Interestingly, in both cases (^{20}Ne and ^{56}Ni data) the simulations predict the position of the kinematic plot at five strips left to the experimental one, what might be an indication of a systematic angular offset.

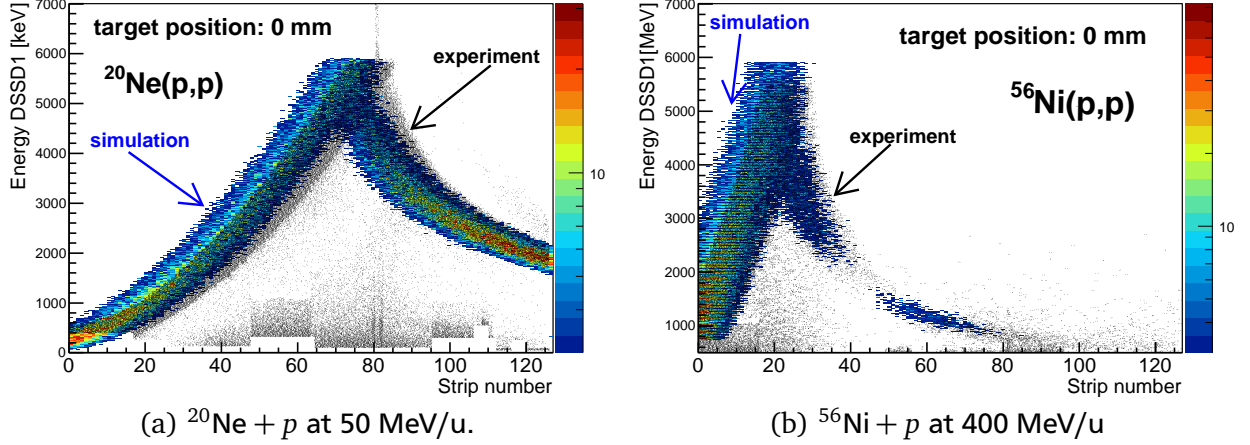


Figure 4.7.: Comparison of simulations with experimental results for elastic scattering in the DSSD of pocket 1. The experiment is presented as black dots while the simulations are in color. In both cases, the simulations were done assuming the same geometry as given in the technical drawings [34].

A possible reason for this difference is a small misalignment, in the order of millimeters, with the center of the gas-jet target during the assembly of the vacuum chamber to the ESR. As it was shown in Chapter 2, the measurement of the target profile (see Fig. 2.7) proved an offset of 0.58 mm along the axis perpendicular to the beam direction. However, the misalignment along the axis parallel to the beam direction is unknown. Likewise, the positioning of the slit plate can also be affected because its calibration was made with respect to the center of the vacuum chamber. Hence, the present simulations can be quite useful to find the real positions of the target center and the slit plate and, eventually, the correction functions for the angular calibration of the experimental data. The basic idea of our calculations is to fit the experimental data with simulations for diverse target-center positions along the axis parallel to the beam direction. Also, the slit plate position x_{slit} , parallel to the detector surface, is varied, as suggested by the schematic illustration in Fig. 4.8.

For fitting these two parameters it is clear that we should make use of two different energy spectra: with and without the slit plate. Initially, the fit of the energy spectrum without the slit plate is done separately to determine z_{tar} . Later, this result is employed during the fitting procedure of the slit plate data in order to limit the number of degrees of freedom of the system.

For the comparison of the simulated and experimental spectra, the centroid and standard deviation of the peak of each strip are tabulated at the end of every simulation. With these values, the respective χ^2 parameter is obtained as

$$\chi^2 = \sum_{i=0}^{127} \frac{(E_{i,\text{exp}} - E_{i,\text{sim}})^2}{\sigma_{i,\text{exp}}^2}, \quad (4.3)$$

where $E_{i,x}$ is the energy centroid of the peak in the strip number i and $\sigma_{i,x}^2$ is the corresponding variance. Each simulation, with a given geometry configuration, delivers a single value of χ^2 which is stored in a matrix. From this matrix one can eventually search for the global minimum by a numerical interpolation.

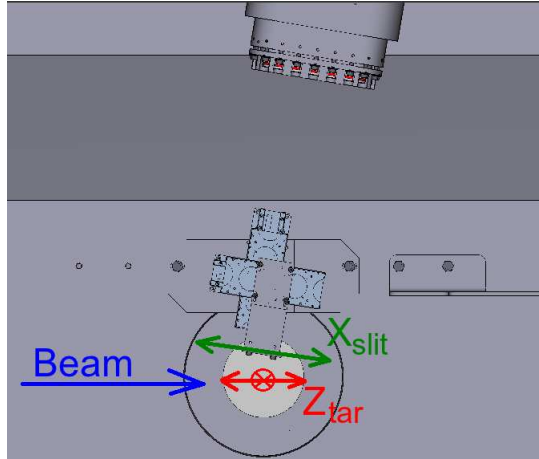


Figure 4.8.: Illustration of the simulated setup. Two parameters are changed in the simulations: z_{tar} (red arrows) and x_{slit} (green arrows).

It is clear that the position of this global minimum corresponds to the best configuration which fits the experimental data.

As mentioned above, the first parameter to be fitted is the center of the target, z_{tar} , using the experimental data without the slit plate both for the ^{20}Ne and the ^{56}Ni case. As can be seen in Fig. 4.9(c), a global minimum of the χ^2 is obtained at $z_{\text{tar}} = 2.5$ mm. Simulations with this result are directly compared with the experimental data previously shown in Fig. 4.9(a) and Fig. 4.9(b). One can observe that this small displacement in the target center is enough to describe satisfactorily the experimental results.

For the next part, the position of the slit plate is also fitted to correct the disagreement with the experimental data, as shown in Fig. 4.10(a). In this case, small displacements from the nominal position of the slit plate can change the position of the kinematic plot significantly because of the improvement in the angular resolution. After the new target position was fixed (z_{tar}), the fit of the experimental data with the slit plate is performed similarly than in the previous case, obtaining the χ^2 for each configuration of x_{slit} . As shown in Fig. 4.10(c), a minimum was found for an offset of $x_{\text{slit}} = 1.0$ mm from the nominal position. Now with this result, the simulation delivers a kinematic plot which is in a good agreement with the experimental data, as also can be seen in Fig. 4.10(b).

In general, such types of geometric corrections not only allow us to describe the kinematic curves of the elastic scattering, but also to perform simulations that are fully consistent with all energy spectra for any channel in our detector setup. This can be applied to perform a more dedicated simulation with the aim to extract the effective angular positioning of the detectors. In this sense, we can extract a relation between the strip (or pixel) number of the DSSDs and the scattering angle of the recoils (an angle calibration) directly. For this task, we can use the *Primary Event Generator class* in order to access the initial momentum of the recoils that are generated in the interaction volume, and store them at every event. For convenience, the spherical coordinates are employed to set the primary direction of the recoils, where the two standard angles are needed: θ the polar angle, and ϕ the azimuth angle. Then, if a detector hit occurred in the simulation, histograms for the primary angles are saved for each pixel activated in the DSSDs. In the DSSD1, 8192 (128×64) histograms are analyzed to obtain the calibration for one of the angles of the recoil scattering. Similarly, for the DSSD2, 512 (32×16) are employed. In Fig. 4.11(a) and Fig. 4.11(b) the results for the angular calibration of the DSSD1 are shown. The relation of the polar angle with the integer strip number from the p -side is highly linear (the Pearson correlation coefficient is $r = -0.9998$), covering the angles from 73° to 89° . This implies that each strip from the front side of the DSSD1 represents a well-defined polar angle θ . For the azimuth angle relation, in Fig. 4.11(b), are shown three samples for different n -side strips: at top edge ($n = 0$), middle ($n = 32$) and bottom edge ($n = 63$). The angular acceptance for each p -side strip is in the range

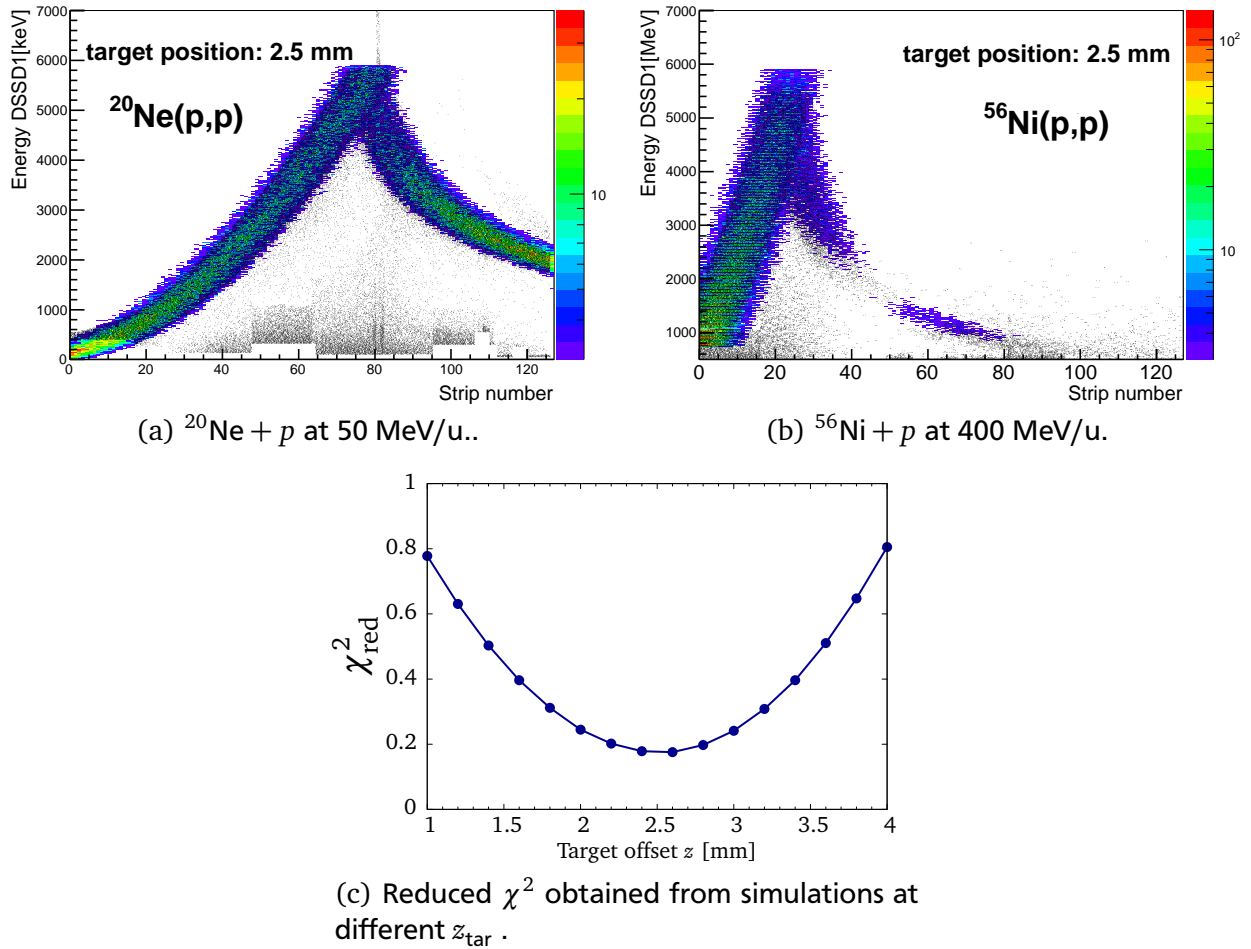
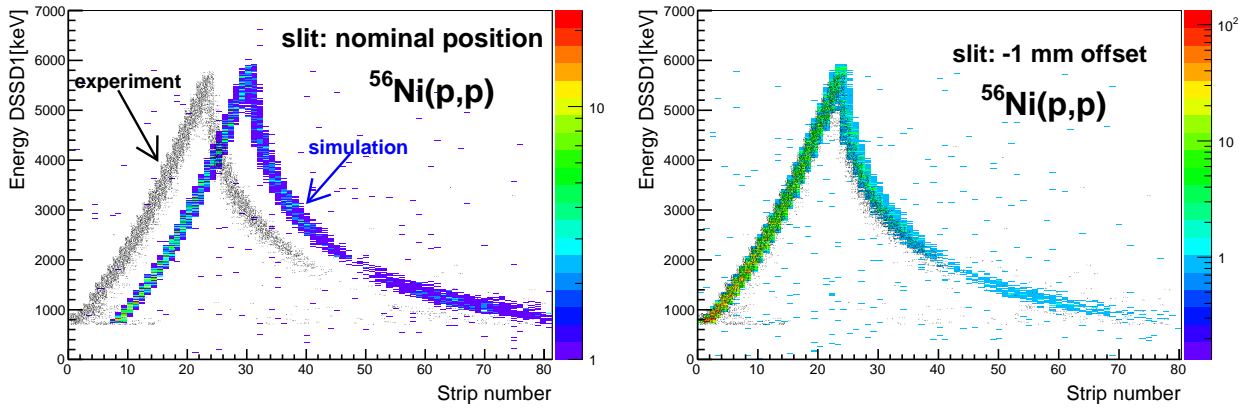


Figure 4.9.: Comparison of experimental data without the slit plate and the simulations using the fitted parameter $z_{\text{tar}} = 2.5$ mm.

of $-7.5^\circ < \phi < 7.5^\circ$. The constant tendency of the curves along the p -side strip number is an indication that also each horizontal strip represents a well-defined azimuth angle ϕ . This can be explained by the relatively large distance of the DSSD1 from the target and its proximity to 90° .

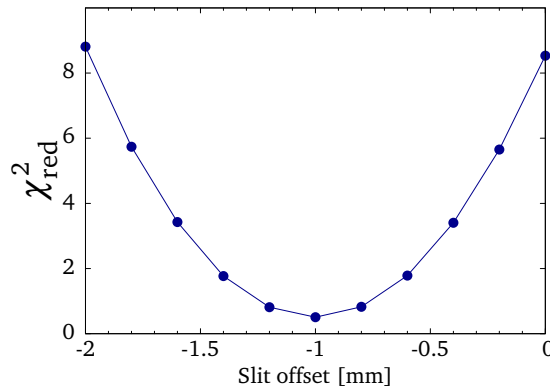
Furthermore, the calibration results for DSSD2 can be found in Fig. 4.11(c) and Fig. 4.11(d). In this detector, the laboratory angular-resolution, which is required for the identification of the inelastic reaction-channels is not as demanding as in DSSD1. This is the case because the center-of-mass angular range of DSSD2 is contracted due to the kinematics of the reaction, i.e., $\Delta\theta_{\text{cm}} \ll \Delta\theta_{\text{lab}}$. Therefore, the signals of each four strips were coupled for the p and n sides. So, the effective number of strips at the front side was 32 and 16 at the back side.

Note, in this DSSD the front-side strip-numbering was inverted with respect to the DSSD1 assignment due the cabling. Similarly as seen in the calibration of DSSD1, due to the large distance between this detector and the target, the relation between the polar angle and the front-side strip number is linear. From this result it is possible to observe that the polar angular coverage of the DSSD2 was in the range of $27.8^\circ < \theta < 37.9^\circ$. Now, in the azimuth angle calibration, we can see a more evident dependence of the ϕ angle with the front-side strips, mostly at the vertical edges of the rear side of the detector. This is caused by the large effective width of these strips (~ 4 mm). As a result, more extended ϕ angle distributions are obtained for the n -side strip projections. For instance, in strips $n = 0$ and $n = 15$ the azimuthal angular distribution has a width of about 2° .



(a) Simulation with x_{slit} at the nominal position.

(b) Simulation with $x_{\text{slit}} = 1$ mm.



(c) Reduced χ^2 obtained from simulations at different x_{slit} .

Figure 4.10.: Comparison of experimental data with the slit plate and simulations using the nominal position and the fitted value $x_{\text{slit}} = 1$ mm.

Another use of the present simulations is the option to derive the solid angle covered by the detector setup, either per pixel or per strip. The advantage of employing numerical simulations for this task is that the exact calculation for solid angles becomes very difficult when an extended beam-target interaction volume is assumed, and even more if the slit plate is included. A way to address the problem is to generate uniformly distributed points on a spherical section by employing Marsaglia's method [64] which is quite efficient for large numerical calculations. This distribution is useful for sampling the momentum orientation of the primary particles created in the interaction volume. The principle of this simulation is to generate N_V particles in directions uniformly-distributed over a total solid angle Ω_V . By definition the solid angle covered by the detector geometry, $\Delta\Omega_i$, is contained in Ω_V , the total solid angle. Then, if only n_i particles hit the detector, the solid angle can be approximated by

$$\Delta\Omega_i \longrightarrow \Omega_V \left(\frac{n_i}{N_V} \right). \quad (4.4)$$

It is clear that the validity of the method depends on the total simulated events, so N_V must be large enough to reduce statistical fluctuations. In the present case, for $N_V \sim 10^9$, the solid angle per pixel is obtained with an error smaller than 5%. In Fig. 4.12(a) and Fig. 4.12(b) the simulation results for the solid angle in each p -side strip of the DSSD1, with and without the slit plate are shown.

In absence of the slit plate, the solid angle distribution is slightly bended around the middle of the detector, as is expected because the edges of the detector are farther from the reaction point. In this

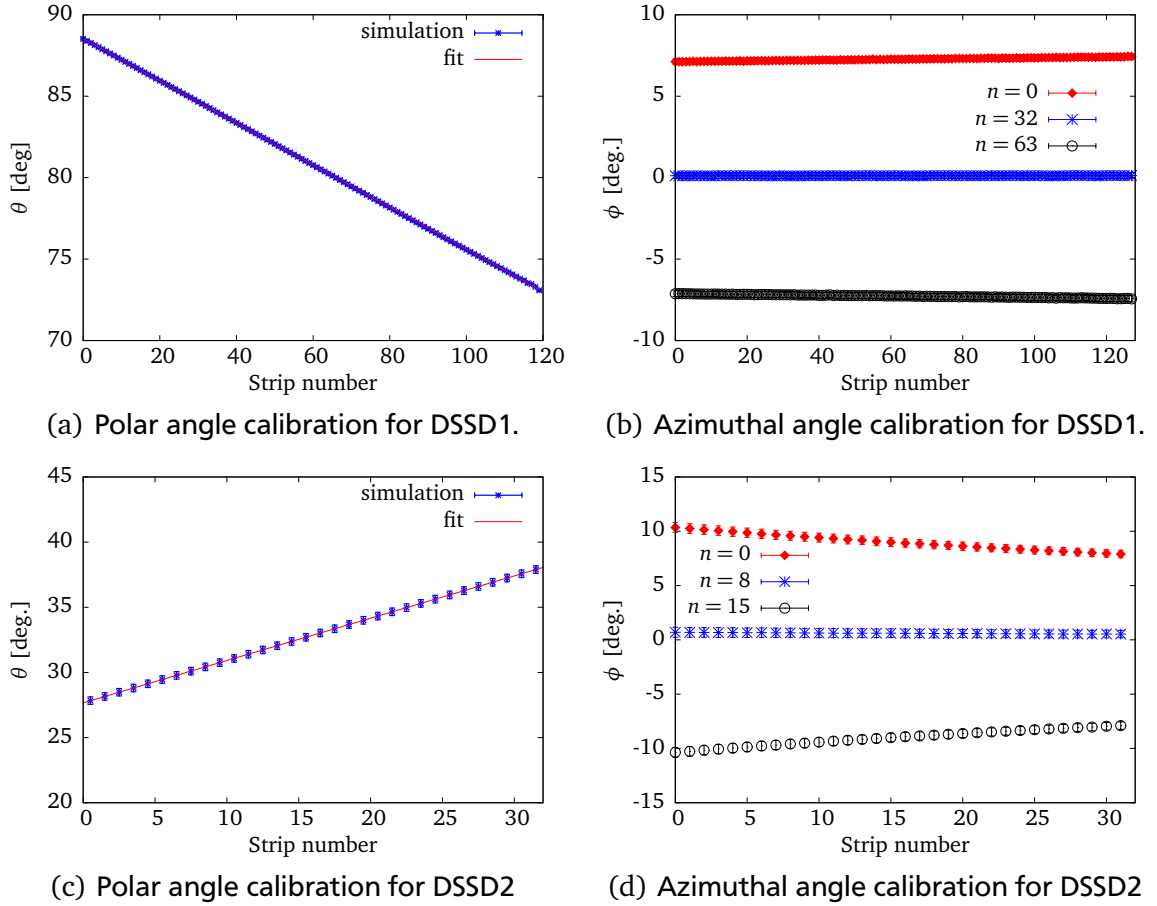


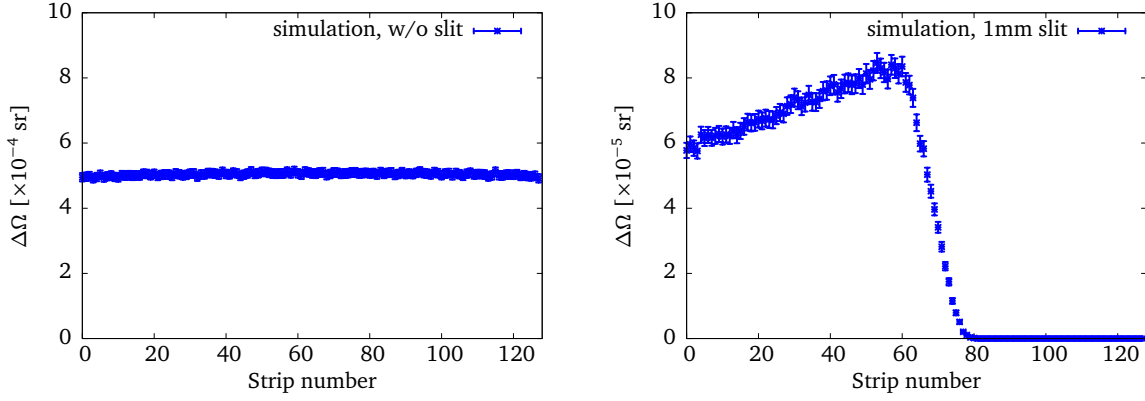
Figure 4.11.: Angular calibration of the DSSDs for the present experimental setup. On the top are the angle-strip correlations for DSSD1 and on the bottom for DSSD2.

case the average solid angle per strip is about 5×10^{-4} sr. Now, when the slit plate is included in the geometry, the solid angle is reduced by almost one order of magnitude. Besides, the respective solid angle distribution is quite asymmetric, with a maximum around the strip number 60. For the strips with numbers larger than 80, the corresponding solid angle drops to values close to zero. This is because the shadowing effect of the slit plate over that region of the detector.

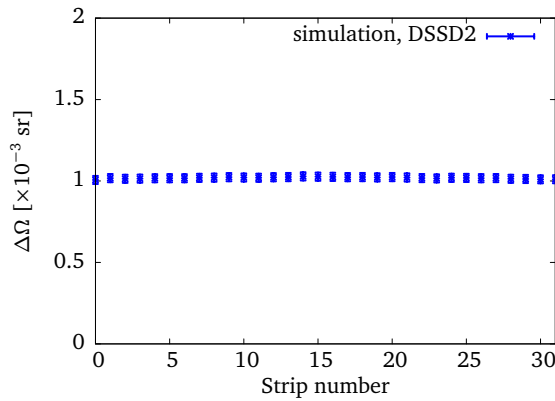
In the case of DSSD2, as seen in Fig. 4.12(c), the solid angles are much larger than the results seen above, since the effective strip width was increased by a factor 4. Since the slit plate was not shadowing this detector, the respective solid angle acceptance is nearly constant for all strips with a value around 1×10^{-3} sr.

4.3 Reaction channels studied with the DSSD2

As it was previously explained, the DSSD2 detector was included in the experimental setup with the aim to measure the recoils produced by inelastic reactions. Particularly, the angular range in which the DSSD2 was mounted is kinematically favorable for the detection of different reaction channels. However, in some cases the identification of a particular reaction channel may be a difficult task because the different contributions are agglomerated in the low energy part of the DSSD2 spectra. In the present angular coverage most of these particles have a very low kinetic energy (hundreds of keV), but it is also possible that very fast recoils punch through the detector losing only a part of their kinetic energy. For example, the reaction $^{20}\text{Ne}(p, d)$ at 50 MeV/u can be observed in the DSSD2 because the deuteron recoils in this angular region (with kinetic energies between 30 to 130 MeV) deposit their energy only in



(a) Solid angles of the DSSD1 without the slit plate. (b) Solid angles of the DSSD1 with the slit plate.

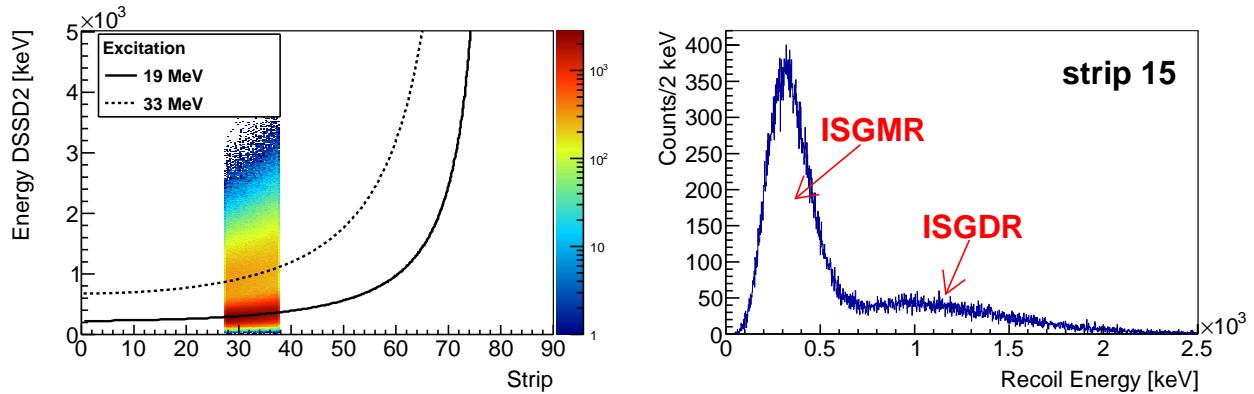


(c) Solid angles of the DSSD2.

Figure 4.12.: Solid angle per strip obtained from simulations. (a) and (b) are the solid angles for the DSSD1 without and with the slit plate, respectively. (c) corresponds to the solid angles of DSSD2.

the range from 500 keV to 1.8 MeV. Thus, the resulting energy spectra are compressed at low energies (below 2 MeV), which sometimes makes the proper reaction channel identification difficult. In this case, the simulations can offer a way to decompose the most important ingredients in the energy spectra and determine the regions of interest for the analysis. In the present work we are interested in measuring in the DSSD2 the excitations of isoscalar nuclear resonances that are mostly excited by alpha inelastic scattering. As explained in Chapter 5, at very forward angles in the center of mass system ($\theta_{\text{cm}} \sim 1^\circ$), the most important contribution to the giant resonances excitation are the monopolar (ISGMR) and the dipolar (ISGDR) multipolarities. In order to simulate these resonances, we have used the experimental results from Ref. [65], wherein such excitations are parameterized as Gaussians, which can be easily implemented into the *Primary Event Generator class*. Initially, it is interesting to see the detector response when the only possible reaction channels are the excitations of giant resonances, because in this way we can explicitly observe the position and shapes of the peaks that are expected in the experiment. For this purpose, the system $^{58}\text{Ni} + \alpha$ at 100 MeV/u was simulated in inverse kinematics. In Fig. 4.13 the energy spectra for the detected recoils in DSSD2 are presented. Fig. 4.13(a) is a 2D histogram of recoil energy vs. laboratory angle (proportional to the strip number). In this figure also the kinematic lines of the excitation energy centroids of ISGMR (19 MeV) and ISGDR (33 MeV) are plotted. As can be seen, the expected peak position of the ISGMR contribution in all strips of the DSSD2 is in average 300 keV. These peaks cover the recoil energies from 100 to 600 keV. For the excitation of ISGDR, the respective recoil

distributions are more extended than the ISGMR peaks, and their centroids are expected in the energy range of 700 keV to 1 MeV.



(a) 2D histogram of the detected recoils and the particle kinematics for the centroids of ISGMR and ISGDR. (b) Energy projection of a strip in the middle of the detector.

Figure 4.13.: Simulation of ISGMR and ISGDR excitation of ^{58}Ni beam at 100 MeV/u. The α recoils were detected in DSSD2 which covers the laboratory angular range of $[27^\circ, 37^\circ]$.

In Fig. 4.13(b), an energy spectrum of one of the strips from the middle of DSSD2 is shown. This projection shows the relative strength of the ISGMR and ISGDR contributions which are expected to occur in the experiment. At angles smaller than 1.5° in the center-of-mass system, the excitation of the ISGMR is dominant [4]. Thus, it is very important to have a good separation of the ISGMR from other reaction channels detected at low energies in order to successfully identify the events originating from the excitation of nuclear resonances. It is also important to consider these other reaction channels, because their contribution may be a significant source of contamination for the giant resonances identification. The first step is to identify the most likely reaction channels to be observed in the present angular range. For instance, very few elastic scattering events are expected to be seen in DSSD2 due to the small cross section contribution in these angles and the high kinetic energy of these recoils. In contrast, given that the target is composed of a molecular gas, atomic reactions like electronic transitions or δ -ray production can occur with a significant rate in this region. The δ -rays are generated when the stored beam knocks out an electron from the target atom at a certain angle and energy, that corresponds mainly to the elastic electron scattering kinematics. In particular, for the present experiments such δ -rays are expected to have energies in the order of few keV, what makes them easily detectable by the silicon detectors. Even more, due to the high production rate of δ -rays in some cases the detection of nuclear reaction channels is also affected. In Fig. 4.14 we see three samples for the δ -rays kinematics produced with ^{58}Ni beam at various energies.

In this plot the vertical green-band corresponds to the angular range covered by the DSSD2. For beam energies of 100 and 150 MeV/u, the recoiling electrons are detected in DSSD2 between 150 to 300 keV. Also, at these energies the recoils originating from nuclear inelastic scattering (at very forward angles in center-of-mass system) are expected. Obviously, difficulties for the identification in the experimental data are foreseeable. In the case of 400 MeV/u, the kinetic energy of the δ -rays is higher, sufficient to punch through the DSSD. The probability that these electrons deposit all energy in the detector is quite small, but due to the high intensity of this reaction channel the contribution from the total absorption energy is detectable. The same can be observed in Fig. 4.15, where the dashed lines represent the simulation of δ -rays when only the elastic scattering kinematics is assumed. Each peak corresponds to the total energy deposited by electrons in different frontal strips of the DSSD2. In the range below 300 keV, the

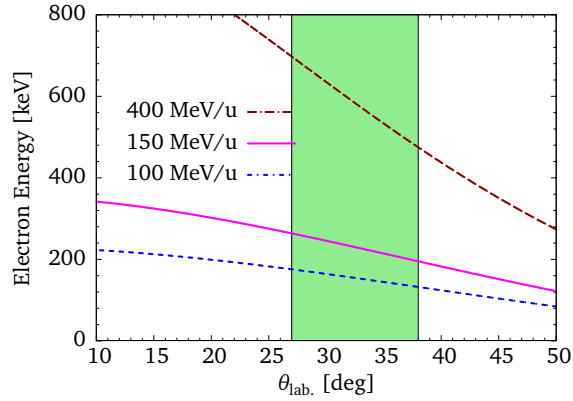
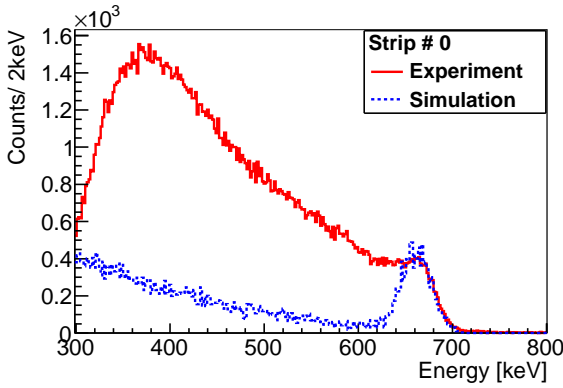
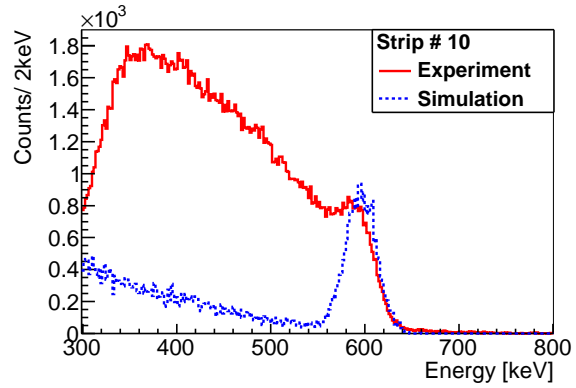


Figure 4.14.: Inverse kinematics for electron elastic scattering: $e(^{58}\text{Ni}, e)$ at 100, 150 and 400 MeV/u. The vertical green band represents the angular range of DSSD2 (centered at 32°).

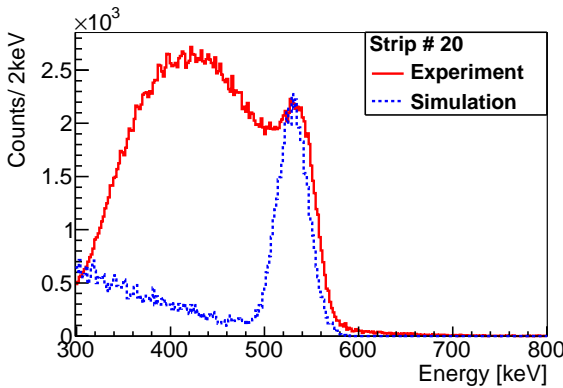
energy loss contribution is much more intense, but in order to have a more clear comparison with the experimental data, the histograms are presented only above this energy value.



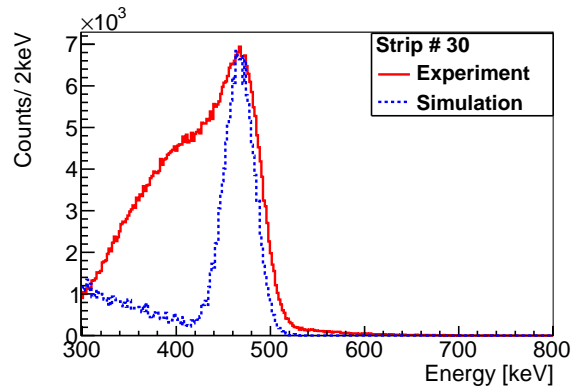
(a) Strip number 0, $\theta_{\text{lab.}} \approx 27.5^\circ$.



(b) Strip number 10, $\theta_{\text{lab.}} \approx 30.7^\circ$.



(c) Strip number 20, $\theta_{\text{lab.}} \approx 33.9^\circ$.



(d) Strip number 30, $\theta_{\text{lab.}} \approx 37.1^\circ$.

Figure 4.15.: Comparison of experiment and simulation of the ^{58}Ni beam at 400 MeV/u on a hydrogen target. The energy spectra correspond to different strips of the DSSD2. Dashed lines are simulations of δ -rays produced in the target and the full lines the experimental data.

In these comparisons we can clearly see the total absorption component of the elastically scattered electrons (normalised to the experiment) at the right side of the spectra. The experimental energy spectra

exhibit a widespread distribution which ends with a pronounced peak corresponding to the electrons that were fully absorbed in the detector, for each strip. In turn, the simulations can properly explain the change in energy position of these peaks for the different strips, which are proportional to the laboratory angle. As expected, the total absorption probability of these δ -rays becomes more efficient at lower energies, close to the punching through energy threshold (~ 300 keV). On the other hand, atomic inelastic processes and nuclear excitations, at very forward angles in the center-of-mass system, are also important ingredients of these experimental energy spectra at the left side to the total absorption component. Hence, if we want to reduce the contribution of atomic processes in the energy spectra of DSSD2, we must decrease the energy of the beam in order to have the scattered δ -rays with lower kinetic energies than the detection range for nuclear inelastic events. In this way it is possible to separate energetically the undesired atomic contribution from the recoils originating from nuclear excitations.

Coming back to the excitation of giant resonances, we can perform more realistic simulations by including also the δ -rays production reaction channel. In this case it is important to normalize the simulation with the experimental data in order to have a clearer identification of the reaction channels that were measured. In Fig. 4.16 the simulation results for the ^{58}Ni beam at 100 MeV/u and 150 MeV/u are shown.

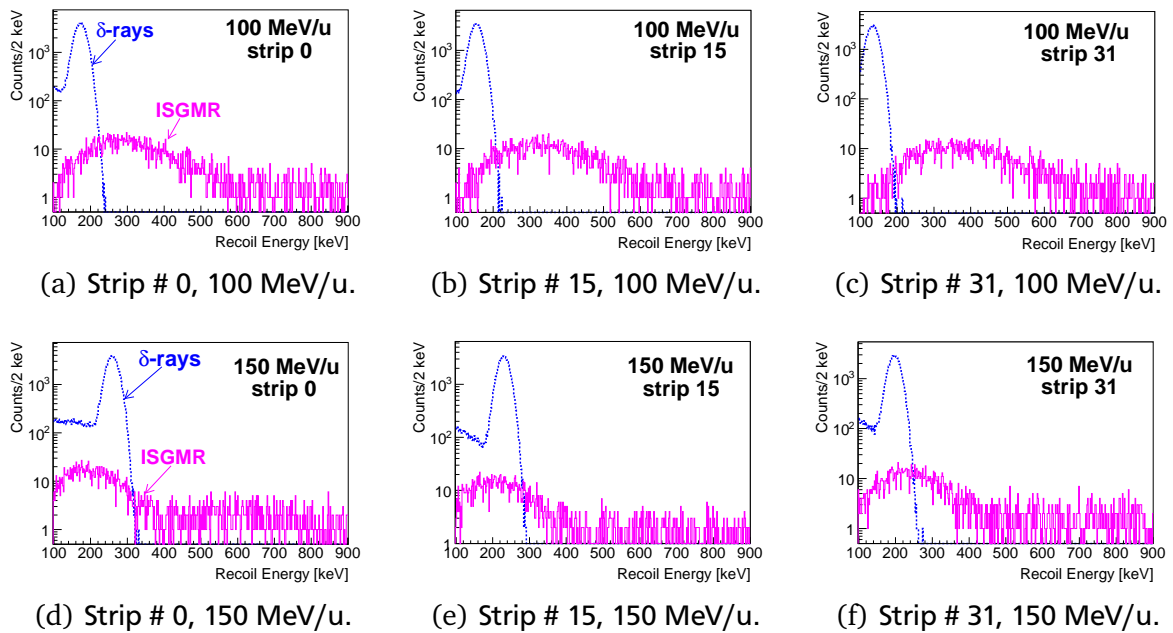
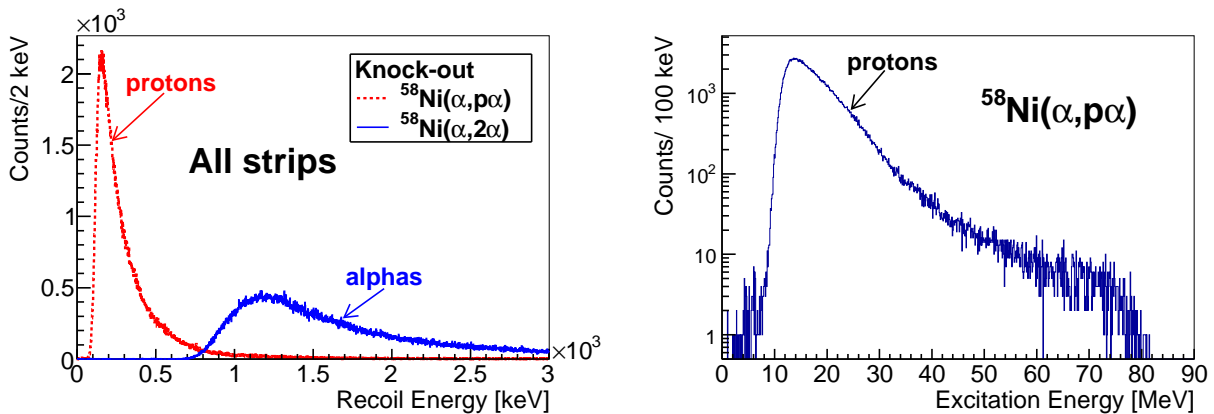


Figure 4.16.: Simulations of DSSD2 including the δ -ray production and the nuclear giant resonances. On the top are three samples of strip energy spectra for ^{58}Ni beam at 100 MeV/u, and on the bottom at 150 MeV/u.

On the top, for the 100 MeV/u simulations, there are three samples of energy spectra for different strips: the two edges of the detector (strips 0 and 31) and the middle one (strip 15). As can be seen, the δ -ray component is at the left hand of the energy spectra, below 200 keV, and its intensity exceeds the giant resonances contribution by more than two orders of magnitude. In the first strips (starting from number 0) the separation of the δ -rays and the ISGMR peak is problematic since more than one standard deviation of the resonance peak is immersed in the detection of the δ -electrons. However, this separation becomes more evident for the last strips due to the kinematics of both δ -rays and recoils from ISGMR excitation. For the case of 150 MeV/u beam energy, the situation is rather different, the detected electron energies reach up to 300 keV which affects the extraction of ISGMR events in all strips of the detector severely. Therefore, only the measurement of recoils from excitation of states above 25 MeV would be

free from being mixed with the δ -electrons. Hence, the δ -rays can be assumed as an important source of contamination at low energies which can even interfere with the identification of the giant resonance excitation. Besides this contribution, we must take other nuclear direct reactions into account which are kinematically allowed in the DSSD2 angular range in order to estimate the physical background in the detection energies of the giant resonances. In particular, for knockout reactions (unlike the two-body kinematic ones) two light particles are generated in the output channel in a wide range of kinetic energies and angles. So, these knockout products can be detected also in the DSSD2 because they can deposit energies from 100 keV up to 3 MeV in our detector. Then, if we assume that these type of reactions are the main source of background for the giant resonances measurement, it would be interesting to simulate some specific cases in order to study the expected response of the DSSD2. For instance, the reaction channels $^{58}\text{Ni}(\alpha, p\alpha)$ and $^{58}\text{Ni}(\alpha, 2\alpha)$ can be simulated by using the three-body kinematics function that was implemented in the *Primary Event Generator* class. The two light particles are generated at the same event with the respective angles and energies provided by the kinematics function. In Fig. 4.17(a) the simulated detector response for these two reaction channels at 100 MeV/u are shown. These plots are the sum of all strip spectra for the detection of one of the particles of the output channel. The dotted line, that represents the energy loss of the proton produced by the $^{58}\text{Ni}(\alpha, p\alpha)$ reaction, is an asymmetric distribution covering mainly the same range of the ISGMR event detection. In this reaction channel, the α -particle component is shifted to higher recoil energies (above 600 keV), because these particles deposit more energy in the detector. Similarly, the solid line shows the energy spectrum of an α particle of the reaction $^{58}\text{Ni}(\alpha, 2\alpha)$. In analogy to the observation in the previous case, the energy loss distributions for α particles are more relevant for energies above 1 MeV, which corresponds to an excitation energy of ^{58}Ni of about 40 MeV (assuming a two body kinematics transformation).




(a) Detected energy for all strips of the DSSD2. The dotted line corresponds to the proton energy loss from the reaction $^{58}\text{Ni}(\alpha, p\alpha)$. The solid line is the energy spectrum of only one of the α particles of $^{58}\text{Ni}(\alpha, 2\alpha)$.

(b) Transformation of the proton energy loss to the excitation energy of ^{58}Ni assuming a two-body kinematics reaction.

Figure 4.17.: Simulated DSSD2 response for the knockout reactions $^{58}\text{Ni}(\alpha, p\alpha)$ and $^{58}\text{Ni}(\alpha, 2\alpha)$ at 100 MeV/u. The histograms represent the energy loss detection of only one of the knockout products.

Then, if we want to investigate the background induced by knockout reactions at the region of the ISGMR detection, the contribution of protons to the spectrum may be sufficient to estimate the background shape. In this way, the proton spectrum of Fig. 4.17(a) is transformed to the excitation energy of ^{58}Ni assuming two particles in the output channel (inelastic scattering). This distribution starts approximately at 8 MeV, which corresponds approximately to the nucleon separation energy, and grows rapidly till an energy of about 15 MeV. After this value, the distribution becomes decreasing for an extended excitation



energy range. The present simulations will be useful during the data analysis in order to understand the parameterization of the experimental background.



Theoretical concepts

Nuclear reactions are an important method to investigate the complex microscopic properties of the nucleus. Usually, a projectile particle (a) with a certain kinetic energy impinges on a target one (A) and, the energies and scattering angles of the collision products are measured. When one of the collision partners (or both) have relevant internal degrees of freedom, the intrinsic states of the projectile-target system may change from an initial state $|\alpha\rangle \equiv |a, A\rangle$ to a different final one $|\beta\rangle \equiv |b, B\rangle$. Such states are called the reaction channels [66]. The most important is the entrance or elastic channel, corresponding to $|\beta\rangle = |\alpha\rangle$. Also, the projectile can excite the target nucleus (or vice-versa) from its ground state to some higher energy state, thus losing some kinetic energy and at the same time being deflected in angle. This is an inelastic scattering reaction channel. The cross section for such processes yields information on spin and parity of the nuclear states, and is sensitive to the wave functions of the nucleons that are excited [67]. When the detector angle is fixed and the energy of the ejectile (b which remains in its ground state) is measured, a spectrum for the energy transferred to the heavier particle is obtained. A typical result for such a spectrum is illustrated schematically in Fig. 5.1.

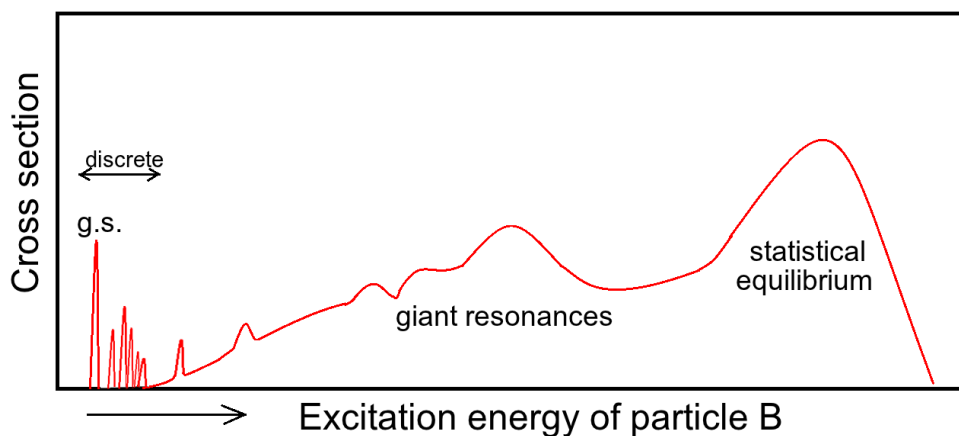


Figure 5.1.: Schematic representation of the spectrum of excitation energies resulting from a reaction $A(a, b)B$. (Adapted from Ref. [68])

We can observe a group of discrete peaks at the low energy part (left edge) which correspond to the excitation of the low-lying states, starting from the ground state component (elastic scattering, if $b = a$). At higher transferred energies, approximately from 10 to 30 MeV, the system exhibits broad resonances. These are the giant resonances. Such states can be excited by a predominantly one-step direct process [68]. The giant resonances correspond to a collective motion involving many if not all the particles in

the nucleus [5]. At even higher energies is a continuous spectrum of energies that corresponds to the formation of a compound nucleus is found. This continuous spectrum is the result of evaporation from a compound system that has reached the statistical equilibrium [68].

In general, a nuclear collision is a complicated many-body process with strong interactions in which a very large degrees of freedom may contribute. Thus, from an initial state $|\alpha\rangle$, many final reaction channels can be involved in a nuclear collision. In particular, our interest in the present work is the investigation of channels coming from direct reactions. These reactions are characterized to occur by a one-step process only. For instance, elastic scattering, transfer reactions and excitation of giant resonances can be studied under this supposition. Along this chapter fundamentals of this reaction theory will be revised.

5.1 Elastic scattering by a short-range potential

The scattering of two particles can be assumed as a wavefunction problem from the quantum mechanics point of view. In this case, the nuclear interaction of the two particles is described by the scattering of a plane wave on a short-range potential $V(r)$, where $r = |\mathbf{r}_1 - \mathbf{r}_2|$ is the relative distance between the two nuclei. Such a potential is supposed to vanish at large distances beyond the nuclear range. An illustrative cartoon of the problem can be seen in Fig. 5.2. Here, a plane wave is propagated in the direction of the potential $V(r)$, where the wave is diffracted isotropically.

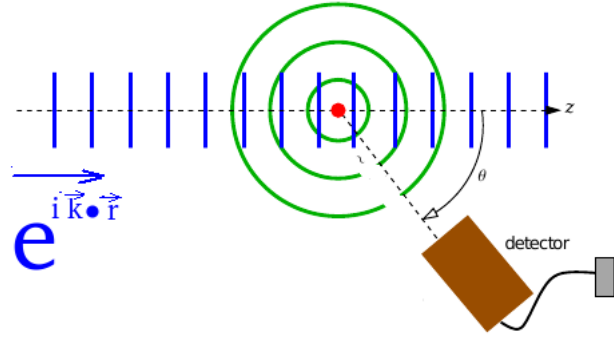


Figure 5.2.: Illustrative cartoon of a plane wave scattering by a short-range potential. A spherical wave emerges from the interaction point. An observer (or detector) is placed at large distance from the source.

Now the problem consists in finding the relative contribution seen by an observer placed at a certain position away from the diffractive source. In order to solve this problem, we can assume a wavefunction $\psi(\mathbf{r}, t)$ that satisfies the Schrödinger equation. The wavefunction with energy E can be written as [66]

$$\psi(\mathbf{r}, t) = \psi(\mathbf{r})e^{-iEt/\hbar} \equiv \psi(\mathbf{r})e^{-i\omega t}. \quad (5.1)$$

This means, also the stationary equation is satisfied

$$(\nabla^2 + k^2) \psi(\mathbf{r}) = U(r)\psi(\mathbf{r}), \quad (5.2)$$

where

$$\omega = \frac{E}{\hbar}, \quad k = \frac{\sqrt{2\mu E}}{\hbar}, \quad U(r) = \frac{2\mu}{\hbar^2} V(r)$$

and μ is the reduced mass of the projectile-target system. Now we can look for a solution for eq. (5.2) corresponding to a distortion of the incident plane wave

$$\phi_{\mathbf{k}}(\mathbf{r}) = Ae^{i\mathbf{k}\cdot\mathbf{r}}, \quad (5.3)$$

where A is an arbitrary normalization constant. Treating the right-hand side of eq. (5.2) as a source (see Fig. 5.2), the desired solution for the wavefunction form can be written as

$$\psi_{\mathbf{k}}^{(+)}(\mathbf{r}) = \phi_{\mathbf{k}}(\mathbf{r}) + \psi_{\mathbf{k}}^{\text{sc}}(\mathbf{r}), \quad (5.4)$$

where $\psi_{\mathbf{k}}^{\text{sc}}(\mathbf{r})$ is a particular solution given by the boundary conditions. Similar to the experiment, the distance between an observer (detector) and the scattering center is much larger than the potential range. Therefore, our interest is limited to the asymptotic solution of the problem (i.e. for $r \rightarrow \infty$). In the present case, this solution consists of an outgoing spherical wave emerging from the scattering center. So, near to the detector, the asymptotic form of the wavefunction is

$$\psi_{\mathbf{k}}^{(+)}(\mathbf{r}) \rightarrow A \left(e^{i\mathbf{k}\cdot\mathbf{r}} + f(\theta, \phi) \frac{e^{ikr}}{r} \right), \quad (5.5)$$

where $f(\theta, \phi) \equiv f(\Omega)$ is called *scattering amplitude*, which describes the dependence of the amplitude of the outgoing spherical wave. In this amplitude, all information about the projectile-target interaction can be found, and physically it can be related to the scattered particles flux in a solid angle $\Delta\Omega$. Thus, one can use the probability current density (probability current per area or flux) [66, 69]

$$\mathbf{j}_{\text{sc}} = \frac{\hbar}{2\mu i} \left((\psi^{\text{sc}})^* \nabla \psi^{\text{sc}} - \psi^{\text{sc}} \nabla (\psi^{\text{sc}})^* \right), \quad (5.6)$$

in order to obtain the count rate $N(\Omega, \Delta\Omega)$ through the detector surface $\Delta\mathbf{S} = \Delta\Omega r^2 \hat{\mathbf{r}}$. Hence, it can be shown that by using the asymptotic form of the scattered wavefunction in eq. (5.6) (in spherical coordinates), the count rate is given by [66, 69]

$$N(\Omega, \Delta\Omega) = (\Delta\Omega r^2) \hat{\mathbf{r}} \cdot \mathbf{j}_{\text{sc}} = v |f(\Omega)|^2 |A|^2 \Delta\Omega, \quad (5.7)$$

where $v = \hbar k / \mu$ is the classical velocity of the particle with momentum $\hbar k$. On the other hand, the probability current density of the incident plane wave can easily be deduced: $\mathbf{j}_{\text{in}} = |A|^2 \mathbf{v}$. Therefore, by the definition of the differential cross section [69], one finally obtains

$$\frac{d\sigma}{d\Omega} = \frac{r^2 \hat{\mathbf{r}} \cdot \mathbf{j}_{\text{sc}}}{|\mathbf{j}_{\text{in}}|} = |f(\Omega)|^2. \quad (5.8)$$

This result shows that the problem for the scattering of two particles is reduced to the derivation of the corresponding scattering amplitude. Eventually, this task is done assuming a scattering potential. Such a potential can be taken as a complex

$$U_{\text{opt}}(r) = V(r) + iW(r), \quad (5.9)$$

where the imaginary part, $W(r)$, accounts the absorption from the elastic flux, in analogy to the imaginary part of the refraction index in wave optics [70]. For this reason the present potential is called *optical potential* [69]. In order to see the effect of introducing an imaginary part in the potential, we can easily extract the divergence of the current density (eq. (5.6)) using the eqs. (5.2) and (5.9).

$$\nabla \cdot \mathbf{j}_{\text{sc}} = \frac{1}{\hbar} \left[(\psi^{\text{sc}})^* W \psi^{\text{sc}} + \psi^{\text{sc}} W (\psi^{\text{sc}})^* \right] = \frac{2}{\hbar} |\psi^{\text{sc}}|^2 W, \quad (5.10)$$

with the probability density $\rho^{\text{sc}} = |\psi^{\text{sc}}|^2$ we then obtain the equation of continuity [69]

$$\nabla \cdot \mathbf{j}_{\text{sc}}(\mathbf{r}) = \frac{2}{\hbar} \rho^{\text{sc}}(\mathbf{r}) W(\mathbf{r}). \quad (5.11)$$

This relation shows absorption, corresponding to a current sink (loss of flux, $\nabla \cdot \mathbf{j} < 0$), requires a negative imaginary part of the optical potential, $W(r) < 0$, at the range where this absorption occurs. In principle, this absorption process is related to the reduction of the probability current of the elastic scattering due to the influence of other reaction channels.

5.1.1 Scattering amplitude

There are different procedures to deduce the scattering amplitude, but one of the most *direct* methods is through the formalism with Green's functions. The principle of the method is the definition of a Lippmann-Schwinger equation for the scattering problem [66–69], as discussed before

$$|\psi_{\mathbf{k}}^{(\pm)}\rangle = |\phi_{\mathbf{k}}\rangle + G_0^{(\pm)}(E_k)V_0|\psi_{\mathbf{k}}^{(\pm)}\rangle, \quad (5.12)$$

where the projection in the coordinate space of the state $|\phi_{\mathbf{k}}\rangle$ corresponds to the wavefunction of a free particle (eq. (5.3)), and the asymptotic scattered wavefunction is described by the state $|\psi_{\mathbf{k}}^{(\pm)}\rangle$. Until now we can see the similarity of this equation with the solution proposed in eq. (5.4), but also including the incoming and outgoing wavefunctions with the notation (\pm) . The operator $G_0^{(\pm)}(E_k)$ corresponds to the Green's function for a free particle with kinetic energy E_k [66]

$$G_0^{(\pm)}(E_k; \mathbf{r}, \mathbf{r}') = - \left(\frac{2\mu}{\hbar^2} \right) \frac{1}{4\pi} \frac{e^{\pm ik|\mathbf{r}-\mathbf{r}'|}}{|\mathbf{r}-\mathbf{r}'|}. \quad (5.13)$$

Within the asymptotic limit, approximations for the terms

$$\lim_{|\mathbf{r}' \rightarrow \infty} \frac{1}{|\mathbf{r}-\mathbf{r}'|} = \frac{1}{r} \quad \text{and} \quad \lim_{|\mathbf{r}' \rightarrow \infty} \exp(\pm ik|\mathbf{r}-\mathbf{r}'|) = \exp(\pm i(kr - \hat{\mathbf{k}} \cdot \mathbf{r}')),$$

can be employed to deduce the form for the asymptotic wavefunction. Thus, inserting eqs. (5.3) and (5.13) into the coordinate projection of eq. (5.12), is finally obtained

$$\left[\psi_{\mathbf{k}}^{(\pm)}(\mathbf{r}) \right]_{|\mathbf{r}' \rightarrow \infty} \rightarrow \frac{1}{(2\pi)^{3/2}} \left[e^{i\mathbf{k} \cdot \mathbf{r}} + \frac{e^{\pm ikr}}{r} \left(-2\pi^2 \left(\frac{2\mu}{\hbar^2} \right) \langle \phi_{\pm \mathbf{k}'} | V_0 | \psi_{\mathbf{k}}^{(\pm)} \rangle \right) \right]. \quad (5.14)$$

A comparison with eq. (5.5) leads to the relation

$$f(\theta) = -2\pi^2 \left(\frac{2\mu}{\hbar^2} \right) \langle \phi_{\mathbf{k}'} | V_0 | \psi_{\mathbf{k}}^{(+)} \rangle. \quad (5.15)$$

Additionally, it can be shown that the same result is achieved for the incoming-state solution ($|\psi_{-\mathbf{k}}^{(-)}\rangle$) by applying the principle of micro-reversibility and the Green's-function properties [69]. This result shows that the scattering amplitude depends on the matrix element of the optical potential between an initial free state and the full scattering state. Usually, the set of these matrix elements is called *T-matrix* [66, 69]. Each matrix element, $T_{k',k}$, describes the transformation of an initial plane-wave state (of momentum $\hbar\mathbf{k}$) into the scattering final state ($\hbar\mathbf{k}'$) through the presence of a potential V_0 .

5.1.2 The optical limit of the Glauber theory

At intermediate and high energy collisions a convenient way to deduce the elastic scattering amplitude is the eikonal approximation. The conditions for the validity of this approximation are: scattering in forward directions (i.e. $\theta \ll 1$ rad) and small energy transfers from the projectile kinetic energy to the internal degrees of freedom of the target (or projectile) [66]. In this approach, the asymptotic wavefunction can be given by

$$\psi_{\mathbf{k}}^{(+)}(\mathbf{r}) \approx \exp [ikz + i\chi(\mathbf{r})], \quad (5.16)$$

where z is the coordinate along the beam direction and $\mathbf{r} = (\mathbf{b}, z)$ (with \mathbf{b} the impact parameter). Hence, the scattered wave can be interpreted as an incident wavefunction with a phase shift $\chi(\mathbf{b}, z)$ given by the integral of the total nuclear potential [71]

$$\chi(\mathbf{b}, z) = -\frac{1}{\hbar v} \int_{-\infty}^z V(\mathbf{b}, z') dz'. \quad (5.17)$$

Such a phase shift is also called *eikonal phase*. The present approximation is the foundation of the Glauber theory [72, 73]. In this model, the phase shift can be represented as a sum of the individual nucleon-nucleon phase shifts involved in the collision. This theory takes multiple-scattering effects for the nucleon-nucleon interaction into account. However, for heavy nuclei and for nucleus-nucleus collisions, a complete deduction of the Glauber scattering amplitude is not a trivial task. Usually, Monte-Carlo methods are needed to integrate the complex expressions in the full description [74, 75]. Nevertheless, a first order approximation (one-step process) of the multiple-scattering operator can be performed to simplify the problem [66]. This method is called *optical-limit approximation* (OLA). The OLA is a very popular method that has been used in the past for describing successfully intermediate and high energy nucleus-nucleus collisions [76–79]. In this approach, the microscopic nucleon-nucleon scattering amplitude (in the momentum space) is often parametrized as [80]

$$f_{NN}(\mathbf{q}) = \frac{k_{NN}}{4\pi} \sigma_{NN} (i + \alpha_{NN}) e^{(-\beta_{NN} q^2)}, \quad (5.18)$$

where k_{NN} is the nucleon momentum, and σ_{NN} , α_{NN} and β_{NN} are average free nucleon-nucleon parameters extracted from experimental p - p and p - n cross sections at different energies [77, 80]. A way to connect this parametrization with the nuclear eikonal phase is through the t - $\rho\rho$ potential [66, 81]. In this model the nuclear ground state densities are assumed to be spherically symmetric, what in turn simplifies the calculation of projectile-target folding with the elementary scattering amplitude. So, the nuclear eikonal phase reduces to the expression

$$\chi_N(b) = \int_0^\infty dq q \tilde{\rho}_P(q) f_{NN}(q) \tilde{\rho}_T(q) J_0(qb), \quad (5.19)$$

where $\tilde{\rho}_i(q)$ are the Fourier transform of projectile and target densities, and $J_0(qb)$ is the zero-order Bessel function. Finally, this phase shift is employed to deduce the total elastic scattering amplitude

$$f(\theta) = -ik \int db b J_0(qb) [e^{i\chi(b)} - 1], \quad (5.20)$$

which also contains the Coulomb phase-shift and must be calculated separately (a detailed explanation can be found in Ref. [66]).

5.2 Distorted waves

In the description of inelastic scattering it is convenient to split the total potential in two parts:

$$U = V_0 + V_1, \quad (5.21)$$

an average interaction (optical potential) V_0 , and V_1 that involves inhomogeneous effects [68]. In principle, the part of the problem with the V_0 potential has a known solution, whereas V_1 poses a too difficult

problem which has to be approximated. Similar to the explanation in Section 5.1.1, the state $|\phi_{\mathbf{k}}\rangle$ corresponds to the incident plane waves, and the distorted waves due to the potential V_0 are now represented by the state $|\chi_{\mathbf{k}}^{(\pm)}\rangle$. Hence, these wave functions satisfy the homogeneous differential equation

$$(E - K - V_0) |\chi_{\mathbf{k}}^{(\pm)}\rangle = 0, \quad (5.22)$$

with K being the kinetic energy operator. The solution of this problem is already known, and leads to the Lippmann-Schwinger equation

$$|\chi_{\mathbf{k}}^{(\pm)}\rangle = |\phi_{\mathbf{k}}\rangle + G_0^{(\pm)}(E)V_0|\chi_{\mathbf{k}}^{(\pm)}\rangle. \quad (5.23)$$

On the other hand, we are interested in a special solution of the inhomogeneous problem

$$(E - K - V_0) |\psi_{\mathbf{k}}^{(\pm)}\rangle = V_1|\psi_{\mathbf{k}}^{(\pm)}\rangle, \quad (5.24)$$

where $|\psi_{\mathbf{k}}^{(\pm)}\rangle$ are the waves distorted by the total potential U . So, the present problem is reduced to the solution of the integral equation [67]

$$|\psi_{\mathbf{k}}^{(\pm)}\rangle = |\chi_{\mathbf{k}}^{(\pm)}\rangle + G^{(\pm)}(E)V_1|\psi_{\mathbf{k}}^{(\pm)}\rangle, \quad \text{where} \quad G^{(\pm)}(E) = \frac{1}{E - T - V_0 \pm i\epsilon}. \quad (5.25)$$

With the help of some identities of the Green's functions and an expansion of this operator [67, 68], it is possible to derive an expression for the transition amplitude [66]

$$T_{k',k} = \langle \phi_{k'} | V_0 | \chi_k^{(+)} \rangle + \langle \chi_{k'}^{(-)} | V_1 | \psi_k^{(+)} \rangle. \quad (5.26)$$

This result is known as the *two potential formula* or the Gell-Mann-Goldberger relation [68]. Usually, V_0 is chosen to describe the elastic scattering (optical potential) while V_1 is the interaction which induces the non-elastic transition. In particular, V_1 is assumed to be weak in comparison to V_0 . Therefore, it is valid to approximate the solution taking the *Born expansion* in powers of the interaction potential V_1 in eq. (5.25) [82]

$$|\psi_{\mathbf{k}}^{(\pm)}\rangle = |\chi_{\mathbf{k}}^{(\pm)}\rangle + G^{(\pm)}V_1|\chi_{\mathbf{k}}^{(\pm)}\rangle + G^{(\pm)}V_1G^{(\pm)}V_1|\chi_{\mathbf{k}}^{(\pm)}\rangle + G^{(\pm)}V_1G^{(\pm)}V_1G^{(\pm)}V_1|\chi_{\mathbf{k}}^{(\pm)}\rangle + \dots \quad (5.27)$$

Therefore, using the eqs. (5.15) and (5.26), with the first order of the Born expansion, the scattering amplitude can be approximated to [66]

$$f(\theta) = f_0(\theta) - 2\pi^2 \left(\frac{2\mu}{\hbar^2} \right) \int d^3r \chi_{k'}^{(-)*}(\mathbf{r}) V_1(\mathbf{r}) \chi_k^{(+)}(\mathbf{r}). \quad (5.28)$$

The present result is called *Distorted Wave Born Approximation* (DWBA). It got its name because of the first order Born approximation in the potential V_1 , and also due to the use of the distorted waves, $\chi_k^{(\pm)}$, instead of incident plane waves. The DWBA is valid as long as the inelastic reaction is sufficiently weak, i.e., the elastic scattering is the most important reaction channel, so that the inelastic scattering events can be treated as perturbations. For stronger transitions, the coupled channel formalism offers the most useful means of going beyond the first order in the interaction causing the transition [67]. The corresponding inelastic scattering amplitude for the reaction $A(a, b)B$ can be generalized to [66]

$$f_{\text{DWBA}}^{\text{inel}}(\theta) = -2\pi^2 \left(\frac{2\mu}{\hbar^2} \right) \int \chi_{\beta}^{(-)*}(\mathbf{k}_{\beta}, \mathbf{r}_{\beta}) \langle b, B | V_{\text{tran}} | a, A \rangle \chi_{\alpha}^{(+)}(\mathbf{k}_{\alpha}, \mathbf{r}_{\alpha}) d^3r_{\alpha} d^3r_{\beta}. \quad (5.29)$$

Here, function χ_{α} describes the elastic scattering in the $\alpha = a + A$ entrance channel arising from an optical potential V_{α} , while χ_{β} describes the elastic scattering in the $\beta = b + B$ exit channel arising from a potential V_{β} . The transition potential U_{tran} which describes the non-elastic transition depends on the type of reaction and the model chosen to describe it. In this work, the DWBA calculations will be of great importance for the description of transfer reactions and inelastic scattering like the excitation of giant resonances.

5.3 Giant resonances

A nuclear giant resonance, as mentioned before, is a collective excitation of the internal degrees of freedom of the nucleus. In quantum-mechanical terms a giant resonance corresponds to a transition from the ground state to an unbound collective one, and its strength is described by a transition amplitude. Intuitively it is clear that the strength of the transition will depend on the basic properties of the system such as the number of particles participating in the response and the size of the system. This implies that the total transition strength should be limited by a sum rule which depends only on the ground state properties. If the transition strength of an observed resonance exhausts a major part, i.e. greater than 50% of the corresponding sum rule, we call it a giant resonance [5].

Giant resonances can be excited principally by the strong (nuclear) and the electromagnetic interactions. There are different methods from which giant resonances can be studied, e.g., γ -ray absorption, coulex, light-ion scattering, charge-exchange reactions, etc [5]. In particular, light-ion inelastic scattering is one of the most common methods employed for the investigation of giant resonances. In this sense, the ingredients of the hadronic interaction can provide an intuitive idea about the internal degrees of freedom involved in this collective transition. The most general form of the central part of the effective nucleon-nucleon interaction may be written as [68]

$$\nu_{12}^{\text{central}} = \nu_{00} + \nu_{10}\sigma_1 \cdot \sigma_2 + \nu_{01}\tau_1 \cdot \tau_2 + \nu_{11}\sigma_1 \cdot \sigma_2 \tau_1 \cdot \tau_2, \quad (5.30)$$

where the vectors σ_i and τ_i correspond to the spin and isospin of the nucleon, respectively. This representation is useful because the subscript of terms ν_{ST} gives rise to a spin transfer (S) and an isospin transfer (T). At low momentum transfer, where the excitation of giant resonances takes place, the non-central components of the nucleon-nucleon interaction are negligible compared to the central term [83]. Therefore only the central part of the effective nucleon-nucleon interaction has a significant contribution to the excitation of giant resonances by light-ion inelastic scattering. An immediate result is that giant resonance excitations involve electric ($\Delta S = 0$) or magnetic ($\Delta S = 1$) transitions, in different isoscalar ($\Delta T = 0$) or isovector ($\Delta T = 1$) modes. For instance, in case of an even-even nucleus the spin-dependent terms of the central interaction (ν_{10} and ν_{11}) are zero in a spin-saturated nucleus [84]. So, exclusively electric isoscalar or isovector resonances might be excited. However, due to the dominant tendency of the isoscalar term (ν_{00}) [83], the most likely excited resonances are the different isoscalar multipolarity modes. Similarly, when giant resonances are studied through α inelastic scattering, isoscalar transitions are excited predominantly because of the $T = 0$ nature of the α -particle.

Another common way to classify the giant resonance modes is from a macroscopic point of view. In this picture a giant resonance can be seen as a high-frequency, damped, harmonic shape vibration around the equilibrium density of the nuclear system. The vibration amplitude is small, only a few percent of the nuclear radius. The restoring forces for these resonances are directly related to bulk properties of the nucleus such as compression modulus, symmetry energy, etc [5]. As it was intuitively seen before, the resonance modes can be classified by the multipolarity L , spin S and isospin T quantum numbers. In Fig. 5.3 few schematic examples of vibration modes resulting from the excitation of different giant resonances are shown. In the present representation the monopole ($\Delta L = 0$), dipole ($\Delta L = 1$) and quadrupole ($\Delta L = 2$) resonances are divided in different spin (S) and isospin (T) modes. Under this supposition it is clear that the center-of-mass position of the nucleus remains constant during the vibration.

In the $\Delta S = 0$, $\Delta T = 0$ case, the resonances correspond to electric isoscalar vibrations in which the protons and neutrons oscillate in phase according to the multipole pattern defined by $\Delta L = 0, 1, 2, \dots$. The $\Delta S = 0$, $\Delta T = 1$ modes are electric isovector vibrations in which the protons and neutrons oscillate out of phase against each other according to a multipole pattern defined by ΔL . The $\Delta S = 1$, $\Delta T = 0$ modes correspond to magnetic isoscalar vibrations in which the nucleons with spin \uparrow vibrate against nucleons with spin \downarrow , again with the multipole pattern given by ΔL . Finally, the $\Delta S = 1$, $\Delta T = 1$ modes are

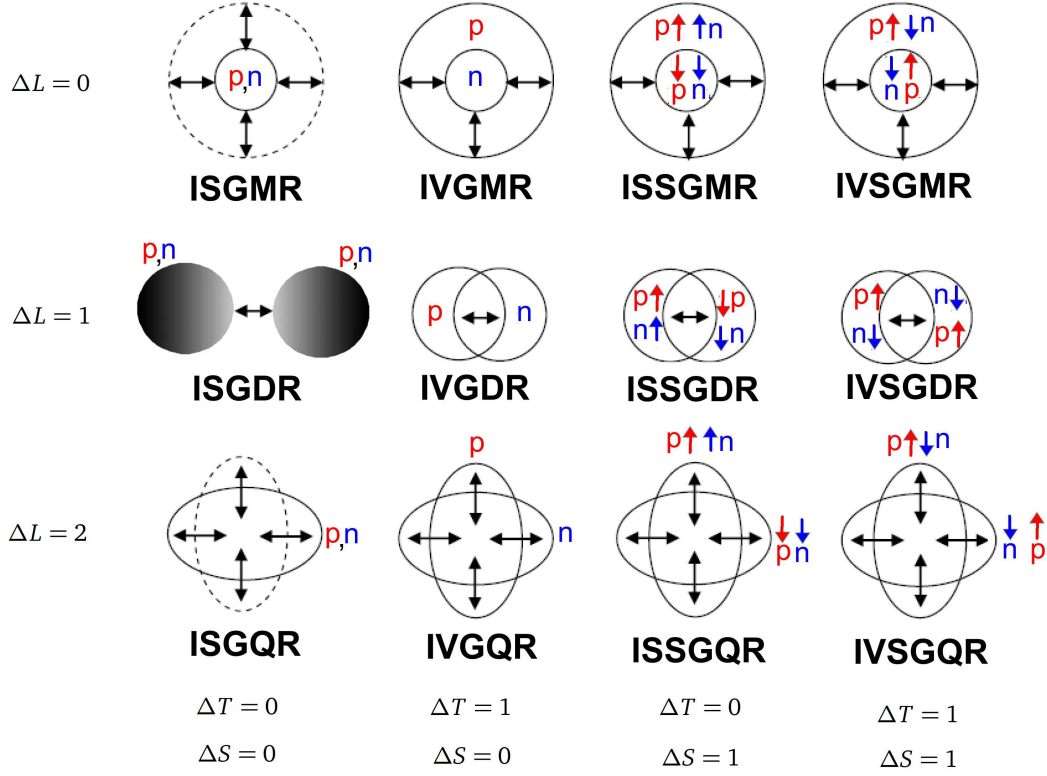


Figure 5.3.: Schematic representation of various collective nuclear modes: monopole ($\Delta L = 0$), dipole ($\Delta L = 1$) and quadrupole ($\Delta L = 2$), for different cases of spin and isospin transfer. The abbreviation of the resonance names are given by the following manner. The first two letters, *IS* or *IV*, correspond to Iso-Scalar and Iso-Vector, respectively. If the following letter is a *S*, it means the resonance mode involves a spin-flip transition. Finally, the last three letters represent the multipolarity of the resonance: Giant Monopole Resonance (GMR), Giant Dipole Resonance (GDR), Giant Quadrupole Resonance (GQR), etc. (Adapted from Ref. [5])

magnetic isovector vibrations where the protons with spin \uparrow (\downarrow) oscillate against neutrons with spin \downarrow (\uparrow).

Specifically, our interest in the present work is the investigation of electric isoscalar giant resonances. The Iso-Scalar Giant Monopole Resonance (ISGMR) is usually associated with a vibration similar to a *breathing mode*. The respective radial compression is related to the nuclear incompressibility. Similarly, the Iso-Scalar Giant Dipole Resonance (ISGDR) can be seen as nuclear vibration in a *squeezing mode*. This mode only exists at the second order approximation of the multipole expansion because the first term corresponds to a translation of the nucleus as whole [5]. For giant resonances of multiplicities up to $\lambda \geq 2$ (here for practicality, $\lambda = \Delta L$), the collective nuclear oscillations are the usual multipole vibrations and their respective transition operators are proportional to the nuclear radius to the λ th power. In a more general way, the electric isoscalar transition operator can be written as [68]

$$F_{\mu}^{\lambda} = \sum_{i=1}^A f^{\lambda}(r_i) Y_{\lambda\mu}(\Omega_i), \quad (5.31)$$

where the summation runs over all nucleons i and the $Y_{\lambda\mu}(\Omega_i)$ are the well known spherical harmonics. The functions $f^{\lambda}(r_i)$ are defined as: r^2 for $\lambda = 0$, r^3 for $\lambda = 1$ and r^{λ} for $\lambda \geq 2$. This transition operator allow us to deduce the strength of a giant resonance from the so-called Energy Weighted Sum Rule (EWSR). The EWSR is determined model independently and is based only on the ground state

properties of the nucleus. A sum rule can be derived from algebraic relations between the transition operators and the Hamiltonian as [5, 85]

$$S_\lambda = \sum_n (E_n - E_0) |\langle n | F^\lambda | 0 \rangle|^2, \quad (5.32)$$

with $|\langle n | F^\lambda | 0 \rangle|^2$ the reduced transition rate from the ground state $|0\rangle$ to a final state $|n\rangle$ which has a corresponding energy E_n . Hence, the EWSR can be deduced for different multiplicities to be [5]

$$S_\lambda = \begin{cases} \frac{\hbar^2}{2m} A \langle r^2 \rangle, & \text{if } \lambda = 0 \\ \frac{\hbar^2}{8\pi m} \frac{3}{4} A \left[11 \langle r^4 \rangle - \frac{25}{3} \langle r^2 \rangle^2 - 10\epsilon \langle r^2 \rangle \right], & \text{if } \lambda = 1 \\ \frac{\hbar^2}{8\pi m} \lambda (2\lambda + 1)^2 A \langle r^{2\lambda-2} \rangle, & \text{for } \lambda \geq 2 \end{cases} \quad (5.33)$$

where $\epsilon = (4/E_2 + 5/E_0)\hbar^2/(3mA)$, with E_0 and E_2 the centroid energies for the ISGMR and ISGQR, respectively. As can be seen, these EWSRs are given in terms of the nuclear mass number A , the nucleon mass m and the i -th radial moment of the ground-state density distribution, $\langle r^i \rangle$. Additionally, assuming that only one of the giant resonance states of multipolarity λ exhausts the respective EWSR, the transition density for such λ -pole can be given by [5]

$$\rho^{(\lambda)}(r) = \begin{cases} -\beta_0 \left[3 + r \frac{d}{dr} \right] \rho_0(r), & \text{if } \lambda = 0 \\ -\frac{\beta_1}{R\sqrt{3}} \left[3r^2 \frac{d}{dr} + 10r - \frac{5}{3} \langle r^2 \rangle \frac{d}{dr} + \epsilon \left(r \frac{d^2}{dr^2} + 4 \frac{d}{dr} \right) \right] \rho_0(r), & \text{if } \lambda = 1 \\ -\frac{\beta_\lambda R}{\sqrt{2\lambda+1}} \left(\frac{r}{R} \right)^{\lambda-1} \frac{d}{dr} \rho_0(r), & \text{for } \lambda \geq 2. \end{cases} \quad (5.34)$$

The advantage of describing the transition densities in the present way is that they only depend on the ground-state density distribution of the nucleus, $\rho_0(r)$. Here, β_λ corresponds to the collective coupling parameter for the isoscalar λ -pole giant resonance which is taken as

$$\beta_\lambda^2 = \begin{cases} \frac{2\pi\hbar^2}{mAE_x} \frac{1}{\langle r^2 \rangle}, & \text{if } \lambda = 0 \\ \frac{2\pi\hbar^2}{mAE_x} \frac{3R^2}{11\langle r^4 \rangle - (25/3)\langle r^2 \rangle^2 - 10\epsilon\langle r^2 \rangle}, & \text{if } \lambda = 1 \\ \frac{2\pi\hbar^2}{mAE_x} \frac{\lambda R^{2\lambda-4}}{\langle r^{2\lambda-2} \rangle}, & \text{for } \lambda \geq 2 \end{cases} \quad (5.35)$$

where E_x is the excitation energy. The present representation of the transition densities permits us to derive the transition potential from a folding model procedure explicitly, as it will be performed in the analysis chapter of this work. In principle, such a transition potential can be employed to describe the angular distribution of a λ -pole giant resonance. As seen in the last section, DWBA calculations are useful to deduce the inelastic scattering cross section (eq. (5.29)).



Data analysis and results

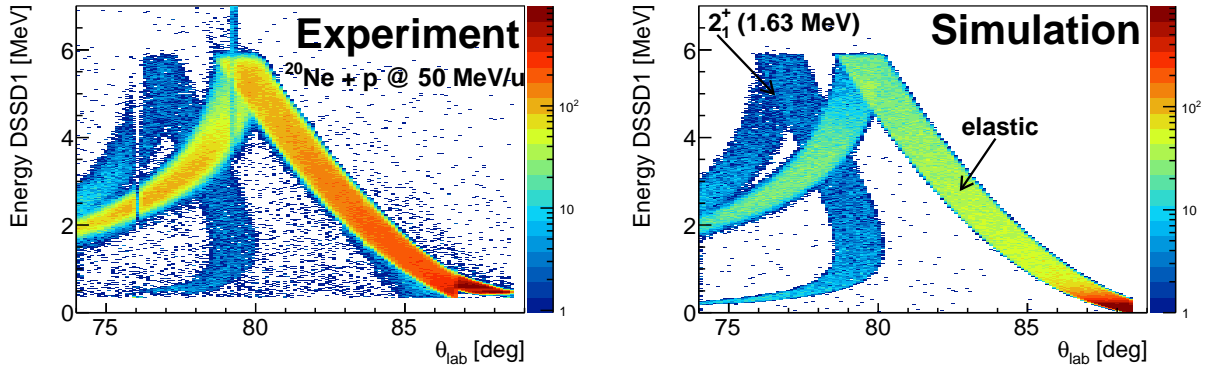
In this chapter, the identification and analysis of the reaction channels measured in the experiments of $^{58}\text{Ni} + \alpha$ (100 and 150 MeV/u) and $^{20}\text{Ne} + p$ (50 MeV/u) will be explained. In the first section, the elastic scattering data and the excitation of low-lying states observed in DSSD1 for different runs will be studied. In the second part, the excitation of isoscalar giant resonances from α inelastic scattering on ^{58}Ni will be investigated with the measurements of low energy recoils in DSSD2. In the third and last part, we will focus on the analysis of the (p, d) transfer reaction measured during the commissioning runs with $^{20}\text{Ne} + p$. The characterization of these reaction channels and the theoretical descriptions of the results will be presented below.

6.1 Elastic scattering and excitation of low-lying states

6.1.1 $^{20}\text{Ne} + p$

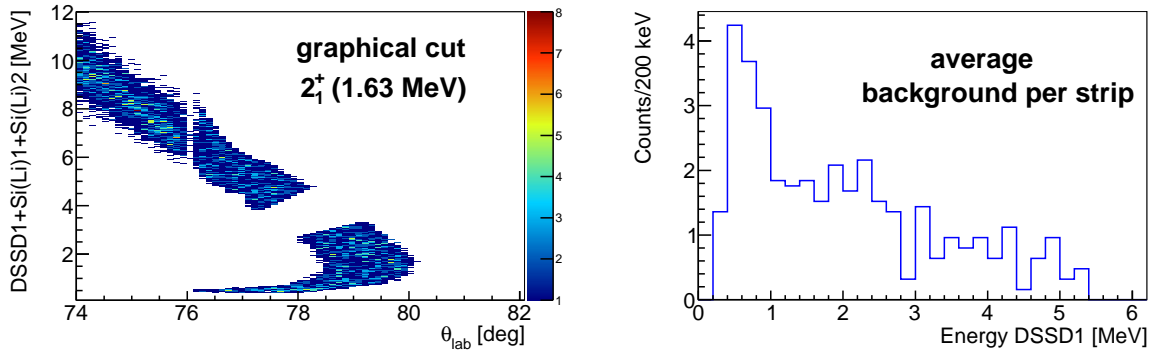
During the commissioning of the experimental setup with the stored ^{20}Ne beam at 50 MeV/u and the hydrogen internal gas-jet target, the slit plate was not included for the measurements. As it was studied in Chapter 4, for these measurements the angular resolution per strip was around 1° (in the laboratory system). However, the corresponding solid angle acceptance was enhanced by about one order of magnitude with respect to the runs with the slit plate. Figs. 6.1(a) and 6.1(b) show a comparison of experimental and simulated DSSD1 spectra for the run with ^{20}Ne beam. Here, the spectra are composed of the energy deposited in each p -side strip which was previously calibrated in laboratory angles, as explained in Section 4.2. As seen in the simulation results, the most intense kinematic band corresponds to the contribution of elastically scattered protons. In the angular range of DSSD1 these recoil particles have kinetic energies up to 20 MeV. As explained before, protons with energies above 6 MeV punch through our DSSDs (285 μm thick), e.g., the elastically scattered recoils at angles smaller than 80° . Although the angular resolution in this case was not improved by the slit plate, the reaction kinematics allows a very good separation of the first excited state of ^{20}Ne (at $E_x = 1.63$ MeV). Fig. 6.1(c) shows the reconstructed energy from the whole detector telescope. For the simulation, in contrast to the real experiment, the scattering on residual-gas particles was not taken into account, what results in less background in the simulated spectrum. Therefore, a direct comparison of experiment and simulation suggests that one of the main sources of the experimental background is the scattering on such residual particles.

Moreover, elastic and inelastic events were discriminated with graphical cuts. As an example, Fig. 6.1(c) shows a cut employed to select the counts from the excitation of the first excited state of ^{20}Ne . The respective graphical cuts were also included as a condition into the analysis routines to obtain the individual strip spectra. Similarly, the background component was selected from the regions out of the



(a) Experiment.

(b) Simulation.



(c) Experiment. Graphical cut of the inelastic scattering events.

(d) Experiment. Average background component in each strip.

Figure 6.1.: Comparison between experiment and simulation results for $^{20}\text{Ne} + p$ at 50 MeV/u. The spectra correspond to the correlation between the p -side strips of DSSD1 calibrated to laboratory polar angle and the deposited energy. The elastic scattering kinematic line and the first excited state of ^{20}Ne are clearly identified. Graphical cuts are employed for the analysis of the individual contributions.

kinematic curves in the 2D histogram. This contribution was projected on the energy axis of DSSD1 to obtain the respective profile. The average background profile per strip can be seen in Fig. 6.1(d). As can be noticed, the background at large energy values (close to 5 MeV) is about one event per 200 keV energy bin, and the most significant component is in the energy range below 1 MeV. On average, less than 40 events in total correspond to the background contribution in the energy spectrum for each strip. Thereby, the present energy distribution is employed to subtract the background in each spectrum. Finally, the total amount of events for different reaction channels are extracted from each strip. Then, the differential cross section is deduced, as explained in Section 3.3. Below, the resulting angular distributions will be studied.

Elastic scattering

The experimental angular distribution of elastically scattered protons by the stored ^{20}Ne beam is shown in Fig. 6.2(a). Here, the differential cross section (in the center-of-mass system) is presented as the ratio of the Rutherford cross section, as it is usually done to overcome the strongly decreasing Coulomb dependence at forward angles. As seen in Figs. 6.1 and 6.2, the laboratory angular range from 72° to 88° represents the center-of-mass region between 10° and 30° . Because of the present laboratory

angular resolution, the corresponding uncertainty for each data point after the transformation to the center-of-mass system is about 1° . Notwithstanding, with this *large* angular resolution it is possible to see the first maximum of the cross section (around 24°) in the clear tendency of the experimental data. For the analysis of this experimental angular distribution we employed three different optical model potentials (OMP): the global potential for protons of Koning-Delaroche [86], one obtained from Ref. [6], and a fit to the present data set using a density-folding potential. The global Koning-Delaroche potential comes from systematics of proton elastic scattering data at different energies and diverse targets. The parametrization is given by

$$U_{\text{opt}}(r) = U_0(r) + U_{\text{so}}(r)\mathbf{L} \cdot \mathbf{S} + U_C(r), \quad (6.1)$$

where

$$U_0(r) = V_V f_R(r) + iW_V f_I(r) + iW_D f_I(r), \quad (6.2)$$

and

$$U_{\text{so}}(r) = \left(\frac{\hbar}{m_\pi c} \right)^2 V_{\text{so}} \frac{1}{r} \frac{d}{dr} f_{\text{so}}(r) \quad (6.3)$$

are the central and the spin-orbit parts of the optical potential, respectively, and $U_C(r)$ is the Coulomb potential. The function $f_i(r)$ is usually taken as a Woods-Saxon shape

$$f_i(r) = \left(1 + \exp \left[(r - R_i)/a_i \right] \right)^{-1}, \quad (6.4)$$

where R_i and a_i are the half-density radius and the diffuseness parameter, respectively. The central potential (eq. (6.2)) is composed of a main complex volume part and a surface term that increases the probability of the nucleon-nucleon collisions at the nuclear surface. The spin-orbit interaction (eq. (6.3)) has a Thomas form parametrization and is expressed in terms of the pion-exchange range ($\hbar/m_\pi c$). In the present case, the optical potential parameters from the Koning-Delaroche systematics are shown in Table 6.1. The second OMP used for the analysis corresponds to a fit of the elastic scattering cross section, $^{20}\text{Ne}(p, p)$ at 42.6 MeV, where the adopted potential form is similar to eq. (6.1), but excluding the spin-orbit interaction. Also, the respective OMP parameters are presented in Table 6.1.

OMP Ref.	V_V [MeV]	r_R [fm]	a_R [fm]	W_V [MeV]	r_I [fm]	a_I [fm]	W_D [MeV]	r_D [fm]	a_D [fm]	V_{so} [MeV]	r_{so} [fm]	a_{so} [fm]	r_C [fm]
[86]	39.17	1.15	0.68	5.56	1.15	0.68	4.33	1.30	0.53	4.74	0.94	0.59	1.38
[6]	36.33	1.20	0.75	11.31	1.20	0.79	0.18	1.20	0.79	-	-	-	1.25

Table 6.1.: Optical model potential parameters used for the description of the elastic proton scattering on ^{20}Ne at 50 MeV/u. All radii are given in the reduced form $R_x = r_x A_t^{1/3}$.

The third model used for this analysis is constructed from a folding potential

$$U_F(\mathbf{r}) = \int d\mathbf{r}_1 \int d\mathbf{r}_2 \rho_T(\mathbf{r}_1) \rho_P(\mathbf{r}_2) t(\mathbf{s} = \mathbf{r} + \mathbf{r}_2 - \mathbf{r}_1), \quad (6.5)$$

where ρ_T and ρ_P are the target and projectile ground state densities. The projectile density (^{20}Ne) was assumed to have a Fermi shape with parameters deduced from electron scattering experiments [87], and the proton (target) form-factor parametrization was taken from Ref. [88, 89]. The function $t(\mathbf{s})$ is the very popular M3Y interaction which has extensively been used for the description of elastic and inelastic scattering at low and intermediate energies [90, 91]. The M3Y parametrization employed for the present work is (in MeV) [91]

$$t(\mathbf{s}) = \left[7999 \frac{e^{-4s}}{4s} - 2134 \frac{e^{-2.5s}}{2.5s} \right] + J_0 \delta(\mathbf{s}), \quad (6.6)$$

where the zero-range factor is $J_0 = -276 \text{ MeV fm}^3$. In order to calculate this potential, it was necessary to solve eq. (6.5) numerically by making use of the convolution theorem [92]. Finally, with this folding potential it is possible to create an OMP by applying the same form for the real and imaginary part

$$U_{\text{opt}}(r) = (N_R + iN_I)U_F(r), \quad (6.7)$$

with N_R and N_I factors that are adjusted to fit the experimental data.

As discussed in Chapter 5, with these OMPs it is possible to calculate the respective elastic cross section. In the present work, these calculations are performed with the coupled channels reaction code FRESKO[58]. The results for these three OMPs are also presented in Fig. 6.2.

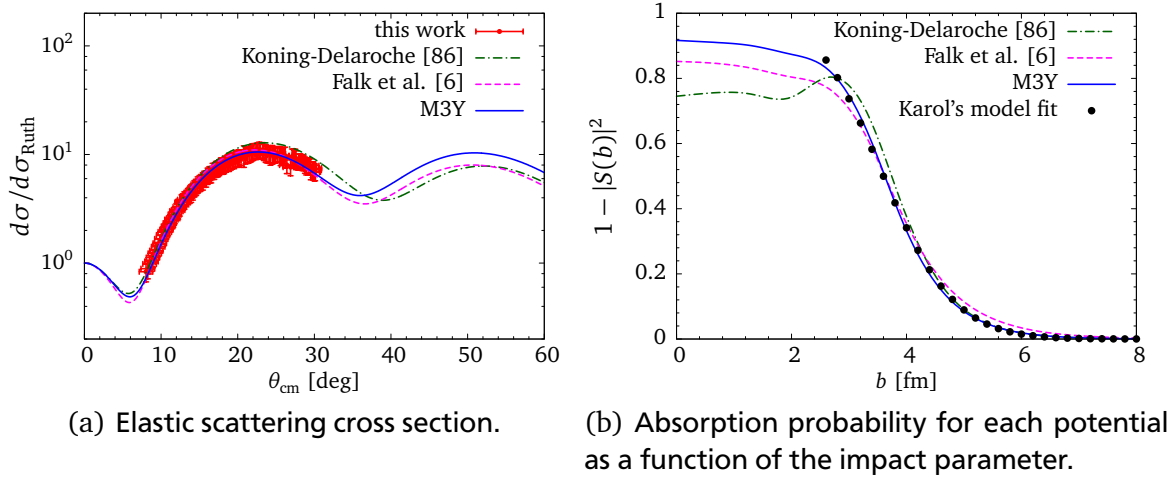


Figure 6.2.: Results from proton elastic scattering on ^{20}Ne at 50 MeV/u. The angular cross section is presented as the ratio of the Rutherford cross section. The experimental data is analyzed with three different optical potentials.

The OMP deduced by Falk et al. and the M3Y (fitted to the present data) are very successful in the description of all experimental points. The differential cross section deduced from the global Koning-Delaroche potential describes the experimental data below 15° , at higher angles this model overestimates the elastic cross section by about 20%, but still agrees with the overall tendency of the experimental data. In principle, these three models seem to be equivalent, but a better comparison can be done by extracting the S-matrix for each elastic scattering calculation, as presented in Fig. 6.2(b). The quantity $T(b) = |S(b)|^2$ is also called the transparency function, therefore the factor $1 - |S(b)|^2$ represents the absorption probability of the optical model, i.e., the reaction channels [93]. The most absorptive OMP in the nuclear centre ($b \rightarrow 0$) is M3Y, while the global Koning-Delaroche is lower by about 20%. At the surface of the absorption probability, above 4 fm, the potential deduced by Falk et al. is more extended due to the larger diffuseness parameters. An immediate result from this analysis is the total reaction cross section that can be expressed as

$$\sigma_{\text{rea}} = 2\pi \int_0^\infty db (1 - T(b))b. \quad (6.8)$$

As it was expected, the total reaction cross section is very similar for these three models: 525 mb for Koning-Delaroche potential, 536 mb for the one of Falk et al., and 535 mb for the M3Y potential. At medium and high energy collisions this quantity is well approximated by the geometric interaction of the target and projectile, $\sigma_{\text{rea}} \propto \pi(r_p + r_T)^2$, with r_x the individual nuclear radius [94–96]. Therefore, one can also extract the nuclear size information from the analysis of the experimental total reaction cross section. A simple method to derive the matter radius is from the approximation of soft-spheres

described by Karol [94]. By fitting the absorption probability at the surface, the density shape can be obtained, since the reaction cross section is slightly dependent on the smaller values of the impact parameter and only the absorption at the surface (out of the total $1 - T(b)$) is relevant for the total σ_{rea} . Thus, the soft-spheres approximation is quite useful, and an expression for the transparency function at the surface can be deduced to be [66, 94]

$$T(b) = \exp \left[-\sigma_{\text{NN}} \int_{-\infty}^{\infty} dz \int \rho_{\text{P}}(\mathbf{r}) \rho_{\text{T}}(\mathbf{r} + \mathbf{R}) d^3\mathbf{r} \right], \quad (6.9)$$

where σ_{NN} is the average nucleon-nucleon cross section at a given kinetic energy and $\mathbf{R} = (\mathbf{b}, z)$ can be conveniently expressed in polar coordinates (with b the impact parameter and z the beam direction) for the integration. The previous expression can be solved analytically assuming Gaussian forms for the densities [94]. However, for consistency with the ^{20}Ne density, the equation is solved numerically assuming a two parameters Fermi distribution (eq. (6.4)). Eventually, the half-density radius (R) and diffuseness (a) of the ^{20}Ne density shape are varied to describe the absorption probability extracted from the analysis of the experimental elastic scattering cross section (Fig. 6.2(b)). For the present case, the average free nucleon-nucleon cross section, taken from Ref. [66], was scaled by using a parametrization suggested for proton-nucleus collisions [97]. The normalization was performed in order to overcome the significant in-medium effects at the present kinetic energy. In the fitting procedure, a weighted difference between the Karol's model calculation $K_i(R, a)$ and the result from a given OMP analysis M_i is performed as ¹

$$w(R, a) = \sum_i \frac{(K_i(R, a) - M_i)^2}{M_i}, \quad (6.10)$$

where i denotes the different discrete points used for the fit. The best (R, a) parameters are extracted from the global minimum of the two-dimensional grid $w(R, a)$. This procedure also permits us to obtain the probability distribution of the fit. Thus, the uncertainties of the parameters R and a are extracted by assuming a 68% confidence interval in the respective probability distribution.

Usually, the nuclear radius is given by the root-mean-square (rms) value

$$R_{\text{m}} = \left[\frac{\int_0^{\infty} f(r, R, a) r^4 dr}{\int_0^{\infty} f(r, R, a) r^2 dr} \right]^{1/2}, \quad (6.11)$$

where $f(r, R, a)$ is the density shape which in the present case corresponds to a Fermi distribution. Besides, the uncertainty of this rms value is deduced from the first order error propagation of the two fitted parameters through eq. (6.11)

$$\Delta R_{\text{m}} = \sqrt{\sigma_R^2 \left(\frac{\partial R_{\text{m}}}{\partial R} \right)^2 + \sigma_a^2 \left(\frac{\partial R_{\text{m}}}{\partial a} \right)^2 + 2\sigma_{(R,a)} \frac{\partial R_{\text{m}}}{\partial R} \frac{\partial R_{\text{m}}}{\partial a}}, \quad (6.12)$$

where σ_R and σ_a are the uncertainties of R and a , respectively, and $\sigma_{(R,a)}$ is the covariance of these two parameters which is also deduced from the probability distribution. The derivatives and integrals of the previous equations are performed numerically. The results of the analysis with the M3Y and the Falk et al. potentials are presented in Table 6.2.

In order to compare our results with the available values from literature, the nucleon size has to be unfolded. For this, the adopted proton radius $r_p = 0.8775$ fm is employed [98]. With the rms radii, the unfolding of the nucleon size is reduced to the relation $\langle r_{\text{m}}^2 \rangle = R_{\text{m}}^2 - r_p^2$, where $\langle r_{\text{m}}^2 \rangle^{1/2}$ is the rms point-matter radius. The resulting rms point-matter radius in the analysis of the M3Y OMP is

¹ Similar to the χ^2 , but with a standard deviation equal to $\sqrt{M_i}$.

OMP	R [fm]	a [fm]	R_m [fm]	$\langle r_m^2 \rangle^{1/2}$ [fm]
M3Y	2.73(14)	0.57(3)	2.99(8)	2.86(8)
Falk et al. [6]	2.28(20)	0.69(3)	3.11(9)	2.99(9)

Table 6.2.: Results from the Karol's model fit to the analysis of the ^{20}Ne data. R and a are the half-density radius and diffuseness of the fitted Fermi distributions. The rms radius R_m is derived from eq. (6.11). The value $\langle r_m^2 \rangle^{1/2}$ corresponds to the point-matter radius (see the text for details).

2.86(8) fm, which is in perfect agreement with the result of a measurement of the interaction cross section, $\langle r_m^2 \rangle^{1/2} = 2.87(3)$ fm [99]. The same procedure was employed with the OMP from Falk et al. to deduce the matter radius. However, the result is larger, 2.99(9) fm, because of the extended diffuseness of this potential. The same problem was observed in Ref. [99] when applying Karol's model. Apparently, the results are considerably influenced by the diffuseness of the absorption probability. So, a method that involves a direct fit of the experimental angular distribution would be preferred for deducing the nuclear matter radius.

Inelastic scattering

As shown in Fig. 6.1, the first excited state of ^{20}Ne (2_1^+ state at $E_x = 1.63$ MeV) was also measured in this experiment. The proton scattering (as has been investigated in the past) is an important probe to determine the radial structure of excited states of the target nucleus [3, 100, 101]. The hadronic projectiles are equally sensitive to both protons and neutrons, while electromagnetic probes, like electrons, are only sensitive to protons. The combination of these two techniques permits to observe deviations from the collective model, where it is assumed that protons and neutrons move in phase with the same amplitude (isoscalar limit) [3]. So, the ratio between neutron and proton multipole matrix elements would be

$$\frac{M_n(\lambda)}{M_p(\lambda)} = \frac{N}{Z}, \quad \text{with} \quad M_{n(p)}(\lambda) = \int \rho_{\text{fi}}^{n(p)}(r) r^{\lambda+2} dr, \quad (6.13)$$

N and Z are the neutron and charge number of the target and $\rho_{\text{fi}}^{n(p)}$ are the neutron or proton transition densities. This implies that the deformation lengths measured from hadron scattering and with an electromagnetic probe are the same, $(\beta R)_{h,h'} = (\beta R)_{\text{EM}}^2$. Thus, for the analysis of our experimental angular distribution of $^{20}\text{Ne}(p, p')$, DWBA calculations assuming the vibrational model can be performed in order to investigate the respective nuclear deformation. The Bohr-Mottelson prescription for the nuclear transition density [102]

$$\rho_\lambda(r) = -\delta_\lambda \frac{d}{dr} \rho_{\text{gs}}(r), \quad (6.14)$$

is used to calculate the transition potential from the folding of eq. (6.5) explicitly, where δ_λ is the multipole deformation length and ρ_{gs} the ground-state density. As usual, the contribution from Coulomb excitation is included using the measured $B(E2)$ value [103], and the nuclear deformation is varied to fit the experimental data. In Fig. 6.3 the experimental angular distribution of the inelastic scattering of ^{20}Ne with the respective DWBA fit is shown.

² $(\beta R)_{h,h'}$ is the deformation length deduced from an inelastic hadron scattering experiment. $(\beta R)_{\text{EM}}$ is the deformation length obtained from a measurement with an electromagnetic probe.

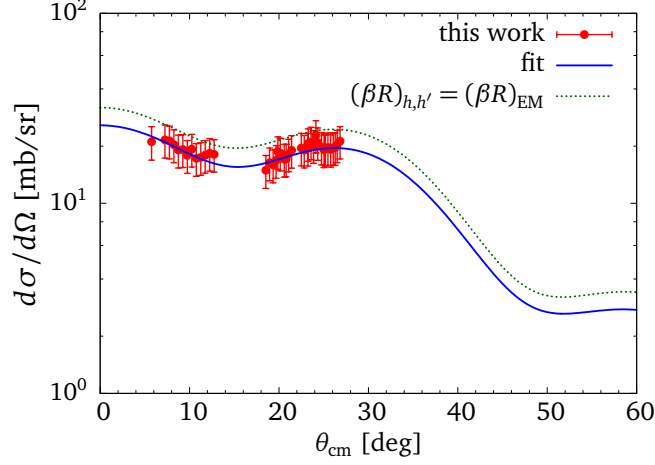


Figure 6.3.: Experimental angular distribution of $^{20}\text{Ne} + p$ inelastic scattering for the first excited state. The solid line corresponds to the DWBA fit. The dotted line is the result assuming the same measured electromagnetic deformation for the nuclear component.

The calculation assuming the same nuclear deformation as the measured electromagnetic deformation, $\beta_2 = 0.73(3)$ [104], overestimates the present experimental cross section by about 20%. From the present DWBA fit, a nuclear deformation $\beta_2 = 0.68(6)$ was extracted, which is about 7% lower than the deformation from a measurement with an electromagnetic probe. A better comparison of these values can be performed with the empirical relation for the ratio of neutron and proton transition matrix elements [3, 105]

$$\frac{M_n}{M_p} = \frac{b_p^p}{b_n^p} \left[\frac{(\beta R)_{h,h'}}{(\beta R)_{EM}} \left(1 + \frac{b_n^p N}{b_p^p Z} \right) - 1 \right] = 0.89(12), \quad (6.15)$$

where the ratio of proton-proton and proton-neutron interaction strengths is $b_n^p/b_p^p = 3$ for proton inelastic scattering at 50 MeV [3]. As can be noted, this result (within the error bars) is in agreement with the unity predicted from the isoscalar limit (eq. (6.13)) for ^{20}Ne , and also consistent with the expectation for a symmetric system, $\rho_p \approx \rho_n$.

6.1.2 $^{58}\text{Ni} + \alpha$

In the runs with the stored ^{58}Ni beam (at 100 and 150 MeV/u), helium was employed as a internal gas-jet target, but in contrast to the previous case, the slit plate was placed in front of DSSD1. Certainly, the price of including the slit was a reduction in the solid angle acceptance, besides a significant amount of background from multiple scattering on the plate. For example, in Figs. 6.4(a) and 6.4(b) a comparison of the experimental and the simulated spectra for the run at 150 MeV/u can be seen. In this case, two excited states of ^{58}Ni were included in the simulation: 2_1^+ at 1.45 MeV and 3_1^- at 4.47 MeV. Moreover, the elastically scattered alpha recoils are seen in DSSD1 only in angles from 86° to 89° , because of the fast increase of the kinetic energies with the polar angle. This reaction channel is easily identified in the experimental data due to the good intensity. The position of the inelastic scattering events from the transitions to the 2_1^+ and 3_1^- states are suggested by the dashed lines. These kinematic lines are still visible in certain regions where the accumulation of data points is more intense than the background. However, the separation of such reaction channels is rather difficult, since the background subtraction plays a critical role.

On the other hand, the elastic scattering contribution was easily separated from the background due to the good signal-to-noise ratio, as can be seen in the graphical cut in Fig. 6.4(c). Similarly, as explained

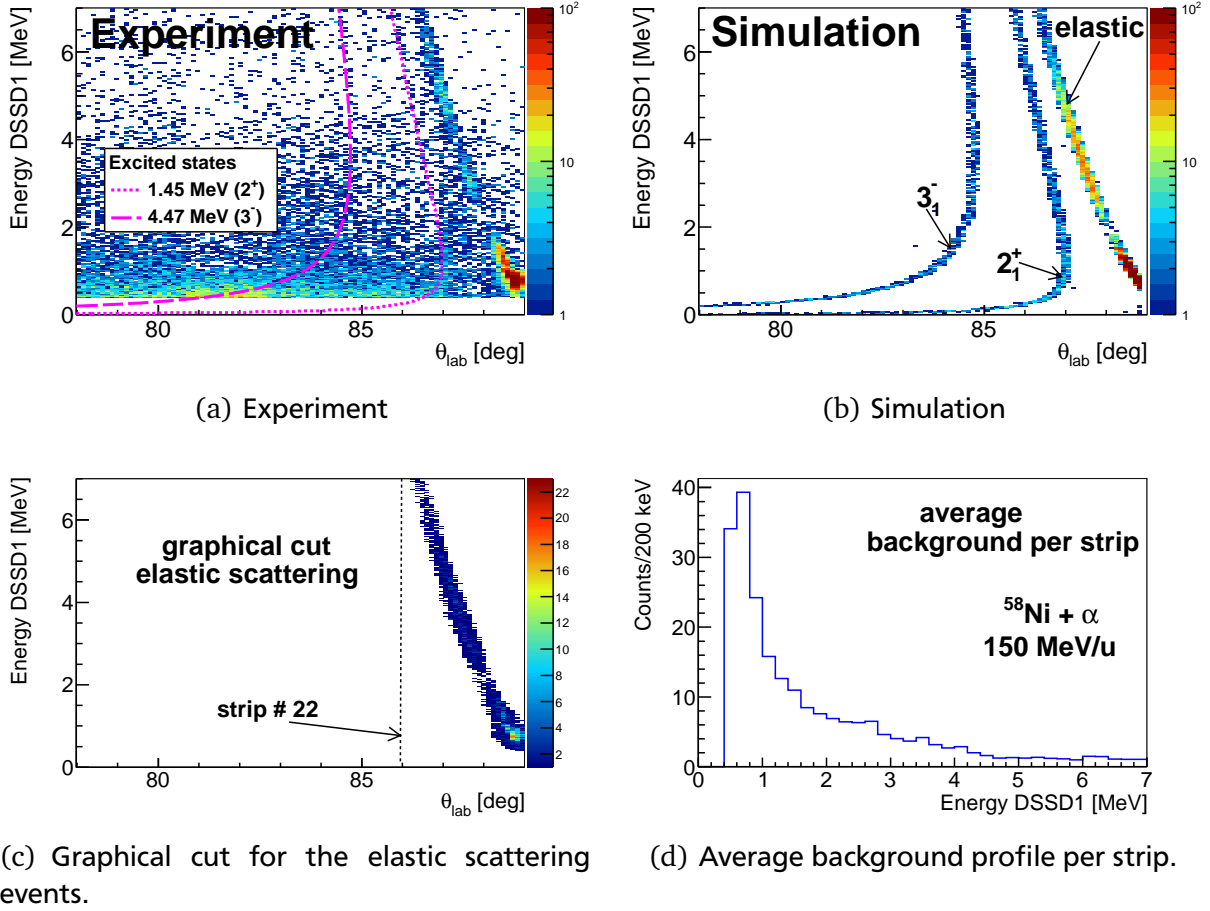


Figure 6.4.: Same as Fig. 6.1, but for $^{58}\text{Ni} + \alpha$ at 150 MeV/u. In this case the slit plate was placed in front of DSSD1. The dashed lines highlight the inelastic scattering kinematic lines.

in the previous section, the average background profile per strip was obtained from energy projection of the regions without contribution of the principal reaction channels. By comparing Figs. 6.4(d) and 6.1(d), it is possible to note the significant influence of the scattering on the slit plate on the average background distribution per strip. In the same way of the previous analysis, the present background profile was subtracted to each strip spectrum of DSSD1. After this background subtraction, the elastic angular distributions were extracted for the runs of 100 and 150 MeV/u. In Fig. 6.5 the experimental angular distributions as the ratio of the Rutherford cross section are shown. The laboratory angular range from 86° to 89° represents angles in the center-of-mass system between 2° to 8° , in both cases. In this angular range, the cross section measurement around the first minimum was achieved for these two distributions. At 100 MeV/u the angular position of this minimum is around 4.2° , while at 150 MeV/u its position was shifted by about 0.5° . It is also important to note the significant improvement in the angular resolution due to the slit plate and kinematics. As seen in the analysis of the ^{20}Ne elastic scattering, the angular uncertainty in the center-of-mass system was around 1° , however, in the ^{58}Ni runs this value was improved by almost one order of magnitude.

For the analysis of these distributions, in contrast to the one of ^{20}Ne which was at much lower energy, the amount of OMPs available in literature is reduced and the global potentials are not as reliable due to the scarce experimental data at such energies. Therefore, the most consistent way to obtain an OMP is from folding potentials that have been tested successfully for a large range of heavy ion collisions and energies. One of the folding potentials employed in this analysis was already studied in the previous section, the

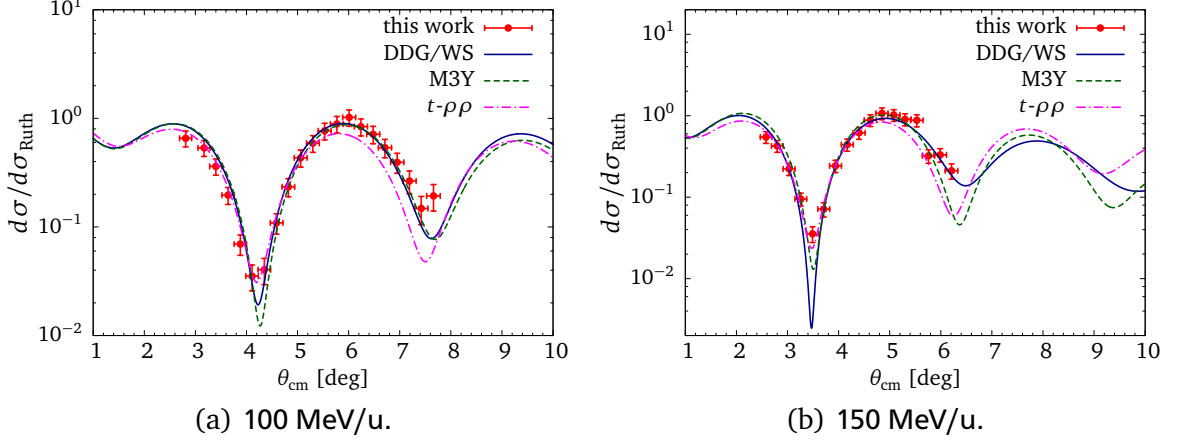


Figure 6.5.: Elastic scattering angular distributions for $^{58}\text{Ni} + \alpha$ at 100 and 150 MeV/u. Similar to Fig. 6.2(a), the distribution is presented as the ratio of the Rutherford cross section. The experimental data was fitted with three different potentials: double-folding M3Y, density-dependent Gaussian (DDG) real interaction and Woods Saxon (WS) imaginary part, and t - $\rho\rho$ in the eikonal approximation.

double folding with the M3Y interaction. The normalizations for real and imaginary depths of the OMP were fitted to the present experimental data by using the program SFRESCO [58]. At 100 MeV/u the M3Y folding potential was normalized to $N_R = 0.824(4)$ and $N_I = 0.603(8)$, where the uncertainties are extracted from the fitting procedure by assuming a 70% confidence interval which corresponds to the hypercontour inside $\chi^2 = \chi_{\min}^2 + 2.41$ [106]. Similarly to the data at 150 MeV/u, the best parameters found were $N_R = 0.755(2)$ and $N_I = 0.80(7)$. The respective depths for this potential can be found in Table 6.3. As can be seen, the analysis with the M3Y potential underestimates the total reaction cross section (σ_{rea}) at 150 MeV/u, which may be due to the reduced angular range for the fit. In principle, this potential describes quite well the present experimental data, but for backward angles the model can lead to an *unrealistic* behavior.

Another potential which in the past has shown good results for describing the angular distributions for α scattering, and in particular to calculate the correct transition potentials³, is the hybrid potential of a single folding with a density-dependent interaction in the real part of the OMP and a Woods-Saxon for the imaginary one [107]. The single folding is reduced to solve eq. (6.5) by replacing the α density by a Dirac-delta function, $\rho_T(r) = A_T\delta(r)$, with $A_T = 4$. The Gaussian interaction employed in this case is [107]

$$v_G(\mathbf{s}) = -v_0 \exp\left(-\mathbf{s}^2/t^2\right), \quad (6.16)$$

with $t = 1.88$ fm and the strength v_0 that is adjusted to optimize the agreement with the experimental data. A density-dependent scaling function is included in this interaction in order to reduce the strength in the interior of the folded potential while leaving the peripheral values unchanged. So, the effective density-dependent interaction used for the folding potential is [107]

$$v_{\text{DDG}}(\mathbf{s}, \rho) = v_G(\mathbf{s})f(\rho), \quad \text{with} \quad f(\rho) = 1 - \alpha\rho(\mathbf{r}')^\beta, \quad (6.17)$$

where $\rho(\mathbf{r}')$ is the ground state density of the target at the position \mathbf{r}' , $\alpha = 1.9 \text{ fm}^2$ and $\beta = 2/3$. Moreover, the imaginary part has a Woods-Saxon potential shape (eq. (6.4)) where its three variables were used as free parameters to fit the experimental angular distributions. In Table 6.3 the best fitting parameters for each case can be found.

³ This will be studied in more detail in the next section, i.e., in the analysis of the angular distributions of the giant resonances.

Energy MeV/u	OMP	V_R [MeV]	W_I [MeV]	r_I [fm]	a_I [fm]	σ_{rea} [mb]
100	M3Y	96.65	70.73	-	-	1431
100	DDG/WS	111.49	40.59	1.39	0.69	1463
150	M3Y	88.56	93.25	-	-	1456
150	DDG/WS	91.46	39.52	1.20	1.19	1706

Table 6.3.: Optical model potential parameters fitted to the α elastic scattering on ^{58}Ni at 100 and 150 MeV/u. The Coulomb radius was fixed as $r_c = 1.2$ fm. All radii are given in the reduced form $R_x = r_x A_t^{1/3}$.

Reasonably good results were achieved with this OMP, and even the reaction cross section deduced from this analysis is in better agreement with the expectation for collisions at such energies. However, the imaginary part at 150 MeV/u is still quite diffuse. As seen in the previous section, this may bring problems when deducing the matter radius by fitting the absorption probability at the surface. In the present case, since the beam energies are much higher, the best way to deduce the nuclear matter radius is to fit the angular distribution directly by adjusting the projectile ground-state density parametrization. This can be done in the optical limit of the Glauber theory with the microscopic t - $\rho\rho$ potential [66, 81]. As seen in Chapter 5, in this model the nuclear scattering amplitude is expressed in terms of the average free nucleon-nucleon parameters extracted from experimental p - p and p - n cross sections at different energies [80, 81]. This means, under the **Optical Limit Approximation (OLA)**, the elastic cross section can be calculated from the average nucleon-nucleon interaction and the folding of the projectile and target ground-state densities. Thus, the density form of the light particle is fixed, while the parameters of the heavy particle density are varied to fit the experimental data. The matter density of the α particle was taken with the same distribution deduced from electron scattering experiments as [87]

$$\rho_T(r) = \frac{A_T}{(a\sqrt{\pi})^3} e^{-\frac{r^2}{a^2}}, \quad \text{with} \quad a = 1.37 \text{ fm.} \quad (6.18)$$

In the case of ^{58}Ni , a two parameters Fermi distribution was assumed, where its half-density radius R and the diffuseness a are optimized to fit the model to the experimental angular distribution. The present calculations were performed with the code DWEIKO [108], where it was necessary to implement routines for the variation of the density distributions and minimization. The result of each calculation was stored in a two dimensional χ^2 matrix for a later analysis. From this matrix, the probability distribution is calculated by transforming each element as [109]

$$P(R_i, a_j) \propto (\chi^2)^{(v/2-1)} \exp\left(-\frac{\chi^2}{2}\right), \quad (6.19)$$

where v is the number of degrees of freedom. Eventually, this 2D grid is normalized, $\sum_{i,j} P(R_i, a_j) = 1$, to represent a probability distribution. As an example, the result for the fit of the ^{58}Ni data at 150 MeV/u is shown in Fig. 6.6. The best (R, a) fitting parameters maximize the probability distribution. The final results are obtained from the marginal distributions, assuming a confidence interval of 68%. The respective fits of the t - $\rho\rho$ potential (optical limit of the Glauber theory) are also presented in Fig. 6.5, and the corresponding parameters can be found in Table 6.4.

As can be seen, this model is quite successful in describing the angular distribution at forward angles where the angular distribution is sensitive to the nuclear matter radius. The component at backward angles is more sensitive to the nuclear interior, and therefore the in-medium effects have more influence on the measured angular distribution. In this case, a renormalization of the free nucleon-nucleon

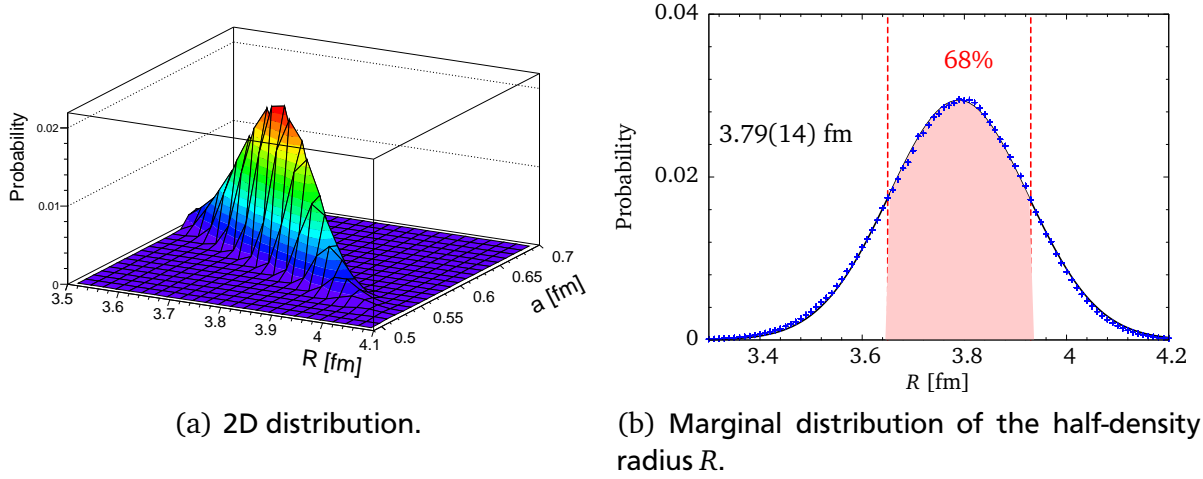


Figure 6.6.: Probability distribution obtained from the fit of the ^{58}Ni data at 150 MeV/u. The most probable value of this distribution corresponds to the parameters with the best agreement to the experimental data. From the marginal distributions ($P(R_i) = \sum_j P(R_i, a_j)$ and $P(a_j) = \sum_i P(R_i, a_j)$), the uncertainties of the parameters are extracted assuming a confidence interval of 68%.

parameters is required [66, 81]. Nevertheless, in the present fits the matter density surface, given by the half-density radius and diffuseness, is very well described. The total root-mean-square radius (see eq. (6.11)) of ^{58}Ni deduced from the fit of run at 100 MeV/u is 3.78(10) fm, and 3.74(9) fm for the one at 150 MeV/u. These values are in perfect agreement with the result of an α scattering experiment in normal kinematics: 3.74(10) fm [1], and also with the reported value from a proton scattering experiment: 3.74(5) fm [2].

Energy MeV/u	R [fm]	a [fm]	R_m [fm]	$\langle r_m^2 \rangle^{1/2}$ [fm]	$\langle r_n^2 \rangle^{1/2}$ [fm]	Δr_{np} [fm]
100	3.81(16)	0.63(3)	3.78(10)	3.68(10)	3.69(20)	0.02(20)
150	3.79(14)	0.62(3)	3.74(9)	3.64(9)	3.61(17)	-0.07(17)

Table 6.4.: Results from the Glauber fit of the ^{58}Ni angular distributions. R and a are the half-density radius and diffuseness of the Fermi shape density. The rms radius: R_m (total matter), $\langle r_m^2 \rangle^{1/2}$ (point-matter) and $\langle r_n^2 \rangle^{1/2}$ (point-neutron). The neutron skin is calculated as: $\Delta r_{np} = \langle r_n^2 \rangle^{1/2} - \langle r_p^2 \rangle^{1/2}$, with $\langle r_p^2 \rangle^{1/2} = 3.68$ fm (point-proton) [87].

From this analysis, the extracted total matter-density distribution, ρ_m , also contains the finite-size of the nucleon. In order to unfold this contribution, the operation

$$\rho_m^{\text{point}}(\mathbf{r}) = \mathcal{F}^{-1} \left[\frac{\mathcal{F}[\rho_m]}{\mathcal{F}[\rho_N]} \right], \quad (6.20)$$

is employed, where the operator \mathcal{F} represents the Fourier transform and ρ_N is the nucleon matter-density which can be assumed to be the same as the proton charge density [88, 89]. Moreover, the (point) neutron density distribution can also be deduced in our analysis by subtracting the (point) proton density of ^{58}Ni . Similar to the unfolding of the nuclear matter distribution, the total charge density (deduced from an electron scattering experiment [87]) is transformed using eq. (6.20) to calculate the point-proton density distribution. In this procedure, the nucleon form factors are taken from the

popular phenomenological parameterizations of Ref. [88, 89]. In Fig. 6.7 the (unfolded) point density distributions deduced from the present analysis are shown.

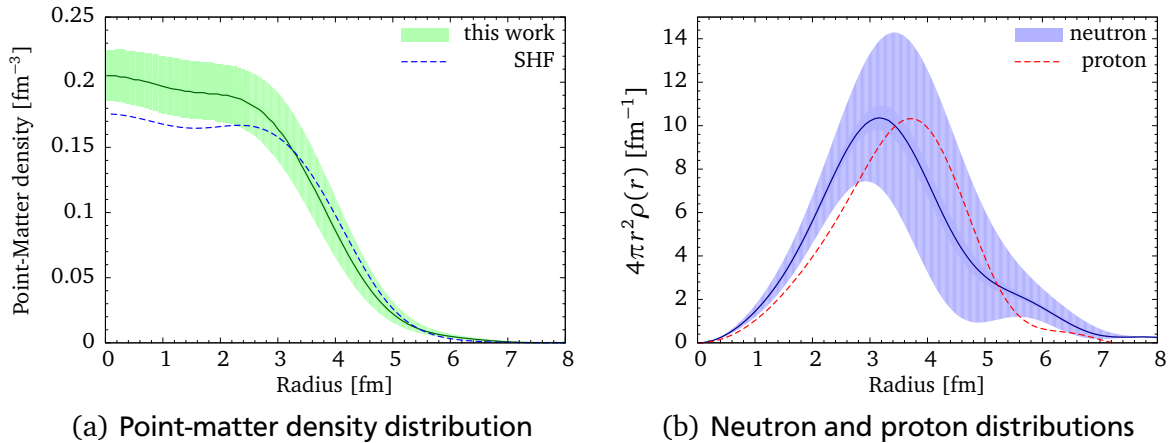


Figure 6.7.: Point-density distributions of ^{58}Ni deduced from the results of this work. The solid lines are the results from the present experiments and the color band are the respective error bands. The point-matter radius is compared with the prediction of a Skyrme-Hartree-Fock calculation (SHF). The neutron and proton contributions are multiplied by $4\pi r^2$ in order to see the distributions at the surface in more detail.

The point-matter density from this experiment is presented within an error band. The nuclear density at low radii has a large uncertainty, since the elastic scattering at backward angles was not measured. However, the density distribution is much better defined at the surface and consistent with the prediction from a Skyrme-Hartree-Fock (SHF) calculation. The SHF was generated with the code SKYRME_RPA [110], including the interaction Sk0' [111]. The rms value from this calculation is 3.68 fm, which is in very good agreement with our experimental results (see Table 6.4). The neutron density was also deduced by subtracting the proton density [87] from the matter distribution. These two distributions are shown in Fig. 6.7(b), where $\rho(r)$ was multiplied by a factor $4\pi r^2$ to emphasize the density at the surface. The proton radius is slightly higher than the neutron radius. However, the neutron density seems to be more extended at large radii. This is in consistence with the neutron skin radius extracted in the present experiments, $|\Delta r_{np}| < 0.07$ fm, and with the literature values which range from -0.05 to 0.01 fm [112, 113].

6.2 Isoscalar giant resonances excitation

The second main part of this work is concerning the excitation of isoscalar giant resonances in an α scattering experiment. As discussed in the previous chapters, the idea of this experiment was to employ DSSD2 which was centered at a laboratory angle of 32° . Given that the present experiment was performed in inverse kinematics, the inelastically scattered α recoils are restricted to laboratory angles below 90° . The kinematic curve of the scattered recoils, for the excitation of the heavy particle, comprises two solutions for a given laboratory angle: at low and high energy regions. In particular, the low energy region of the inelastic scattering kinematics corresponds to the forward angles in the center-of-mass system. In Fig. 6.8 the expected recoil kinematics for an excitation energy of 19 MeV can be seen. As previously mentioned (Section 4.3), the excitation of the ISoscalar Giant Monopole Resonance (ISGMR) of ^{58}Ni is located around this energy value with a standard deviation of 3 MeV [4, 65]. It can be noticed that for the run with a stored ^{58}Ni beam at 100 MeV/u the recoiling α s are expected to be measured in DSSD2 with energies smaller than 1 MeV, where the main component is generated from scattering at very forward θ_{cm} angles.

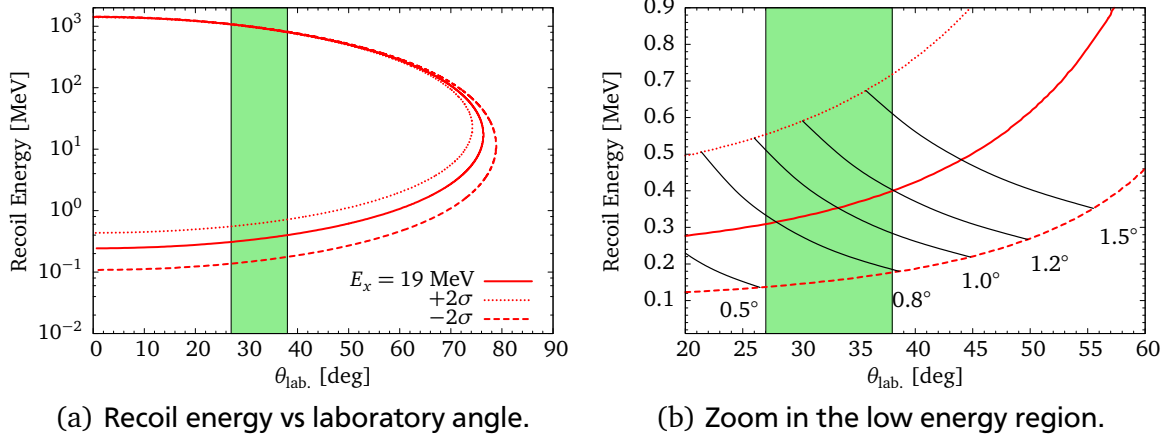
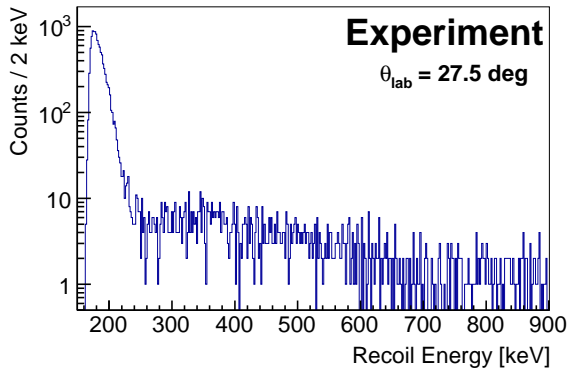


Figure 6.8.: Recoil kinematics for the reaction $^{58}\text{Ni}(\alpha, \alpha')$ at 100 MeV/u. The green vertical band shows the angles covered by DSSD2. The kinematic curves corresponding to an excitation energy of 19 MeV $\pm 2\sigma$ (6 MeV) are plotted with dashed lines.

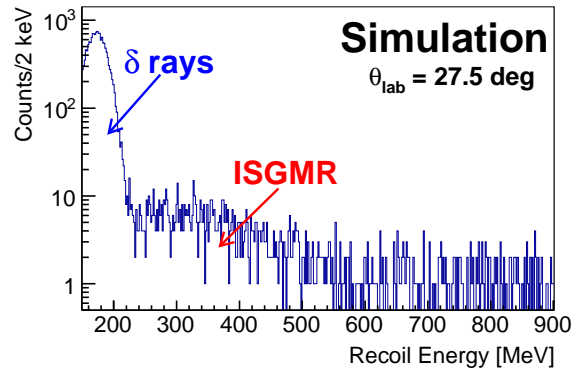
For the resonance range of $\pm 2\sigma$ (6 MeV), DSSD2 covered the angles $0.5^\circ \lesssim \theta_{\text{cm}} \lesssim 1.5^\circ$, corresponding to recoil energies from 100 to 700 keV. Each center-of-mass angle is represented by a transverse curve in the $E_{\text{recoil}}-\theta_{\text{lab}}$ frame. For a single detector strip (which has a well defined laboratory angle), several center-of-mass angles are measured and the only way to identify them is from the detected energy. For instance, in the strip 31 ($\bar{\theta}_{\text{lab}} = 37.5^\circ$) recoil energies around 200 keV belong to scattered angles below 1° , and for energies higher than 500 keV the respective angles are closer to 1.5° .

As studied in Chapter 4, one of the main limitations in the identification of inelastically scattered recoils at low energies in DSSD2 was the presence of atomic reactions, like for example δ -rays produced in the internal gas-jet target. For the experiment with $^{58}\text{Ni} + \alpha$ at 100 MeV/u, the δ -rays were observed at energies below 200 keV. Similarly, the elastic scattering and many direct nuclear reactions generate high energy recoils in the angular range of DSSD2. However, the respective energy losses are also much lower than 200 keV where the δ -rays detection is dominant. Then, in order to identify the energy region in which the recoils originating from the excitation of giant resonances are detected, both elastically scattered electrons and the ISGMR excitation were simulated. The relative ratio of these reaction channels was normalized to the experimental data. Thereby, the different p -side spectra from DSSD2 can be compared with the respective experimental ones in order to associate the main contributions of the energy bumps. Fig. 6.9 shows a comparison for two strips at the edges of the detector, around $\theta_{\text{lab}} = 27.5^\circ$ and 37.5° . In the simulation the ISGMR contribution can be identified as a small energy bump between 200 and 600 keV, as studied in Section 4.3. The kinematics of the δ -electrons contribution is more visible in the angular range of DSSD2, its peak position changed about 100 keV in the angles between 27.5° and 37.5° . The separation of the ISGMR component in the first strips (close to 27.5°) is limited by the δ -rays threshold. However, at higher angles the giant resonance bump is better resolved because the nuclear excitation is the most relevant reaction channel that is kinematically allowed in this energy range. From a direct comparison with the experimental spectra, we can realize that the events produced from the excitation of the giant resonance are the main component of the bump above 200 keV.

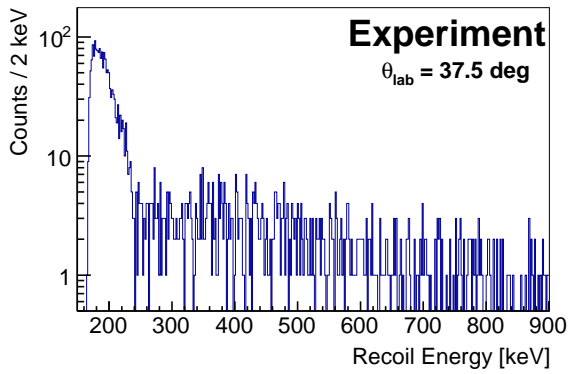
Now, the question is how to remove this significant background of low energy δ -rays. This subtraction should be done before the transformation to the excitation energy-frame. This is important due to the important dependence of the angular distribution (in center-of-mass system) on the recoil energy. Initially, low energy thresholds ($E_{\text{th}}^{\text{low}} \approx 150$ keV) were applied to all strip spectra in order to cut the whole electronic noise and the main part of the δ -rays contributions. Above this threshold, the remaining δ -rays components were fitted to a superposition of three Gaussians to reproduce the tails of these peaks.



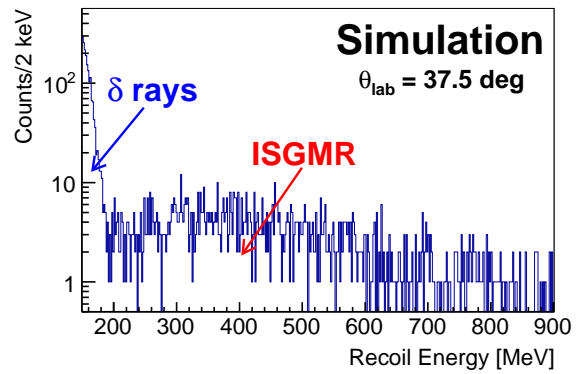
(a) Experiment, strip number 0



(b) Simulation, strip number 0.



(c) Experiment, strip number 31



(d) Simulation, strip number 31

Figure 6.9.: p -side energy spectra of DSSD2 for $^{58}\text{Ni} + \alpha$ at 100 MeV/u. Here, the comparison of strips 0 and 31 is done in order to identify the excitation of the isoscalar giant resonance (see also Fig. 4.16).

After this subtraction, the events from energies between 200 and 250 keV were recovered. Fig. 6.10 shows three samples of strip spectra after the subtraction of the low energy background. In all strips the energy threshold was around 150 keV, i.e., in the two-body-reaction frame the corresponding range of sensitivity is above 15 MeV of the ^{58}Ni excitation energy. As one can note from the comparison of the strip spectra and their respective transformations, recoil energies around 300 keV are correlated to excitation energies around 20 MeV. In all cases the energy bump below 1 MeV (in the laboratory frame) was transformed to a resonance distribution that covers excitation energies up to 35 MeV. This is consistent with the expected peak position of the ISGMR excitation in ^{58}Ni [4, 65]. Nevertheless, the event rate per strip was rather low and therefore, the statistical fluctuations are a big constraint for the individual analysis of each strip signal.

The best option in this case is to add all contributions from the individual strips of DSSD2 in the transformed frame (θ_{cm}, E_x). The double-differential cross section can also be extracted from this spectrum by applying the respective Jacobians of the transformation to each ($\theta_{\text{lab}}, E_{\text{recoil}}$). Fig. 6.11 shows the resulting double-differential cross section as a function of the excitation energy of ^{58}Ni . A clear peak in the energy distribution is obtained with a centroid below 20 MeV. The peak is extended at high energies to almost 40 MeV, but limited towards low energies due to the δ -rays cut around 15 MeV. The present result shows great similarity to experimental cross sections from experiments in normal kinematics [4, 65]. However, we should keep in mind that this cross section contains contributions from different multipoles (but only $L \leq 3$ are contributing in reality) and a component of background produced mostly from direct reactions.

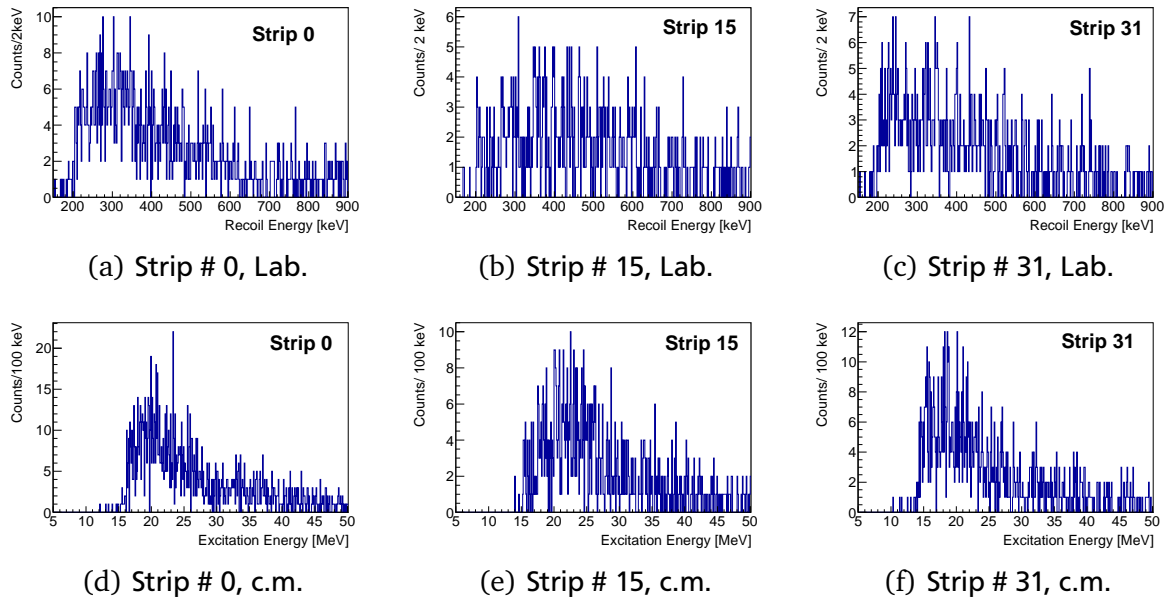


Figure 6.10.: Strip energy spectra after δ -rays subtraction. In the upper part are three samples of recoil energy spectra. On the bottom are the respective transformations to the rest frame of the projectile.

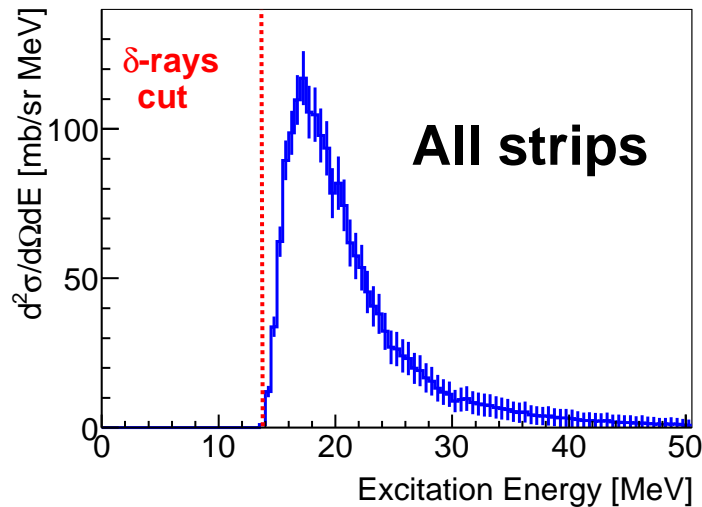


Figure 6.11.: Experimental double-differential cross section for the excitation of the giant monopole resonance in the ^{58}Ni . All spectra from strips of the p -side of DSSD2 were summed up. The sensitivity below 15 MeV was constrained because of the δ -rays cut.

As we can remember from Chapter 4 (Fig. 4.17), in the present experiment, knock-out reactions (in contrast to other direct reactions) are kinematically able to produce recoils in the whole energy range of the giant resonances (GR) detection. Fortunately, this type of reaction channel is less probable than the GR excitation and therefore, its contribution is only seen in the continuous background [5, 114]. This is also consistent with the background parametrization employed in many works [4, 65, 115]. In particular, the most convenient background parametrization in the present case is the one studied in Ref. [115]. The total contribution of the background is divided in a low and a high energy part. The low part arises from an energy about 7 to 8 MeV (E_{thr}) which is approximately the threshold energy for nucleon

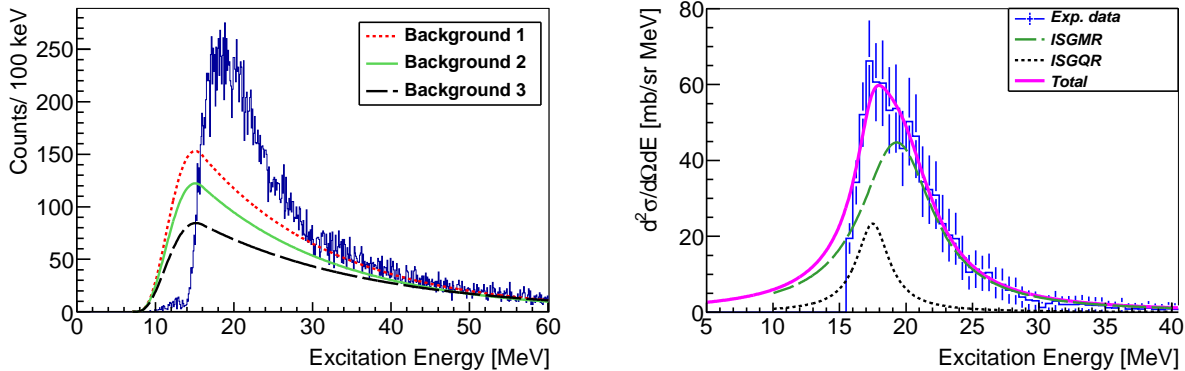
separation. From this point the contribution grows until a maximum value, located at 15 MeV (E_0), where the excitation of the giant resonances starts. The parametrization for the low energy component of the background is given by

$$y_1(E) = \exp [a_1 - b_1(E - E_{\text{thr}}) + c_1 \ln(E - E_{\text{thr}})], \quad (6.21)$$

where a_1 , b_1 and c_1 are free parameters. At high energy, the cross section decays rapidly, so it is reasonable to assume an exponential function for its parametrization

$$y_2(E) = \exp [a_2 - b_2E], \quad (6.22)$$

where a_2 and b_2 are directly fitted to the experimental data in the range above 45 MeV. Finally, the functions y_1 and y_2 are connected by taking care of the continuity using the first derivative criterion. In this way, the other set of variables (a_1 , b_1 and c_1) can be automatically fixed by the definition of the fitted ones (a_2 and b_2). The resulting shape of this parametrization is in agreement with the simulation results of Fig. 4.17(b), which takes into account the proton detection from the knockout reaction $^{58}\text{Ni}(\alpha, p\alpha)$. Because the most possible source for this background is originating from a three-body output channel, it is more convenient to deal with the respective subtraction before the conversion to the double-differential cross section, which includes the Jacobians assumed from a two-body kinematics reaction. For the present analysis, we have studied three different background parameterizations which can be seen in Fig. 6.12(a). The first parametrization has been chosen to cut the contribution above 30 MeV completely. The second parametrization allows more events in this energy region, where the second mode of the ISGDR contributes [4]. Finally, the third parametrization is aimed to subtract less strength from the whole region than the two previous functions. In the following subsection, the effect of the background choice on the strength of the giant resonances will be investigated.



(a) The three different backgrounds studied.

(b) Double-differential cross section after the background 2 subtraction.

Figure 6.12.: Background parametrization and subtraction.

Until this point we can assume naively the second parametrization as the background contribution. After the respective subtraction, the double-differential cross section is obtained, as presented in Fig. 6.12(b). Here, two Lorentz functions are employed to fit the experimental energy distribution in the range between 15 and 40 MeV. These peaks are assumed to describe the two most important resonance contributions at forward angles: isoscalar giant monopole resonance and the isoscalar giant quadrupole resonance. Given that our experimental data is limited to energies higher than 15 MeV, the centroid of the ISGQR was fixed at 17 MeV (as measured in other experiments [4, 65]) during the fitting procedure. The resulting Lorentzian function for the ISGMR component has a centroid in 19.27(61) MeV and a width of 6.45(51) MeV. These values are comparable with results from other experiments performed

in normal kinematics, which are also listed in Table 6.5. In particular, the results from Ref. [4], corresponding to an experiment performed at the same kinetic energy (center-of-mass system), show a great similarity to the present ISGMR contribution not only in the centroid but also in the height of the cross section peak. A more dedicated analysis can be performed including also the analysis of the angular distributions, which allows a decomposition of the different multipole contributions. This procedure is explained below.

6.2.1 Multipole Decomposition Analysis

The Multipole Decomposing Analysis (MDA) has extensively been used by many authors [4, 65, 115, 116] in order to disentangle the individual resonance modes in a given energy range. In this method the resonance region of the double differential cross section is divided in energy bins, and from each of them the respective angular distribution is extracted and analyzed. In the present case, an energy bin size of 1 MeV was chosen in order to reduce statistical fluctuations. For the individual angular distributions, multipole fits were performed by employing theoretical angular cross sections obtained from DWBA calculations. This means that for each energy bin the experimental angular distributions are decomposed using

$$\left(\frac{d^2\sigma}{d\Omega dE} \right)^{\text{exp}} = \sum_{L=0}^2 a(E_x, L) \left(\frac{d^2\sigma}{d\Omega dE} \right)_L^{\text{cal}}, \quad (6.23)$$

where the coefficients $a(E_x, L)$ are related to the fraction of the energy-weighted sum rule (EWSR) of the L^{th} multipole. The DWBA calculations were performed with the code CHUCK3 [59]. In each case, 100% exhaustion of the respective multipole EWSR was assumed. Also, particular care is taken when deducing the right transition potentials. In the past there have been many controversies about how to obtain the proper transition potentials, because a *wrong* assumption can lead to an underestimation of the strengths of the giant resonances. For instance, no evidence was found for the excitation of the giant monopole resonance in $\alpha + {}^{58}\text{Ni}$ experiments in the early 80's [117]. Even a decade later, a reanalysis with incorrect transition potentials resulted in strengths smaller than 30% of the EWSR [118]. The issue of the missing monopole strength in ${}^{58}\text{Ni}$ was resolved at the end of the 90's in the work of Satchler and Khoa [107], where it was suggested to calculate the transition potentials directly from a folding procedure in order to account the strong absorption in the nuclear interior. This procedure has been applied successfully by many authors [4, 65, 119], resulting in monopole strengths in ${}^{58}\text{Ni}$ larger than 70% of the EWSR. In the present work we follow the same method for the analysis of our experimental data. The transition potential corresponding to the multipole λ is obtained from the explicit folding of the transition densities defined in Section 5.3 as:

$$U_\lambda = \int \rho^\lambda(r') v_{\text{DDG}}^\lambda(r, r', \rho) dr'^3, \quad (6.24)$$

where v_{DDG}^λ is the transition interaction which can be taken as a density-dependent Gaussian type (see eq. (6.16) and eq. (6.17)), but with a dynamical correction in the density-dependent term to account the weakening of the folded potential in the interior [107]

$$f(\rho) \rightarrow f'(\rho) = 1 - \alpha(1 + \beta)\rho(r')^\beta. \quad (6.25)$$

As already explained for the analysis of elastic scattering, this single-folding potential was employed with a Woods-Saxon shape in the imaginary part to successfully describe the angular distributions. In addition, the imaginary potential was deformed in the same way as the transition densities to construct the total transition potential included in the DWBA calculations. The deformation parameters of these potentials were also calculated numerically with the expressions presented in Chapter 5.

Moreover, the isovector giant dipole resonance (IVGDR) can also be excited via α inelastic scattering

[120]. This small contribution had to be removed from each angular distribution before performing the multipole fit. The IVGDR cross sections were calculated in the Goldhaber-Teller model [5] and by using the strength distribution $B(E1)$ obtained from an electron scattering experiment [121]. Thus, the multipole decomposition of the isoscalar contributions is applied to every energy bin with the corresponding DWBA calculations for a given excitation energy. Since the angular range of the experimental angular distributions is quite limited, two assumptions were applied in the fitting procedure in order to reduce the ambiguities in the results: one multipole contribution should not exhaust the whole sum rule in a single bin, and the extracted strength (for a given multipole) from two adjacent bins have smooth changes ($\Delta(\text{EWSR})_{i \rightarrow i+1} \leq 5\%$). With this criteria, each fit is performed by minimizing the χ^2 distribution. As an example, the results from the MDA for some energy bins are presented in Fig. 6.13.

The monopole strength is dominant for excitation energies smaller than 30 MeV, where the most significant contribution was found around 20 MeV. Also, the angular distribution of the quadrupole component has a slight effect on the total cross section for excitation energies below 20 MeV. Meanwhile, the dipole contribution increases at high energies where the scattered angles correspond to the minimum of the monopole distribution. As seen in eq. (6.23), the coefficients of the fits are directly related to the percentage of the exhausted EWSR in each energy bin. Thus, the energy distributions for each single multipole component can be extracted from these values. In Fig. 6.14 the results for the monopole contribution are presented. Similar as before, because of the cuts in the double-differential cross section the sensitivity of this energy distribution is constrained to excitation energies higher than 15 MeV. Each histogram bar corresponds to the respective fraction of the EWSR assuming the background parametrization 2. For the monopole distribution, the exhausted EWSR in the energy range from 15 to 30 MeV is about $79^{+12}_{-11}\%$, which is in agreement with the results reported from other experiments, as seen in Table 6.5.

A theoretical prediction from a RPA calculation is also plotted in Fig. 6.14 with the dotted line. This strength distribution was calculated with the code SKYRME_RPA [110], applying the interaction SkO' [111]. The present experimental data shows a very good consistence with the theoretical prediction in the whole energy range of the ISGMR. The energy position of the maximum of the ISGMR distribution is well described by this model. Similarly, the width of this theoretical distribution is in very good agreement with the experimental data. In the MDA such comparisons are performed through the moments of the energy distributions [5]

$$m_k = \sum_k a_L E_x^k, \quad (6.26)$$

where a_L is the fraction of the EWSR for the L^{th} multipole. Thereby, the centroid of the distribution can also be expressed in terms of these moments, namely m_1/m_0 or $\sqrt{m_3/m_1}$. In Table 6.5 the centroids deduced from the present experimental data can be found. The same MDA has been performed for the other background parameterizations presented in Fig. 6.12(a). The centroids deduced for these three cases are similar. However, they are about 1 MeV larger than the values from the literature and from the RPA calculation. The reason for this offset is the asymmetric shape of the experimental energy distributions because of the absence of data points below 15 MeV.

Nevertheless, the good agreement of the RPA calculations with the experimental distribution (in Fig. 6.14) supports the consistence of our results with respect to the reported values in the literature.

Besides the monopole strength, the dipole and quadrupole contributions were also extracted in the MDA, as shown in Fig. 6.15. Similar to the results of Fig. 6.12(b), the quadrupole component has the most important contribution below 20 MeV. However, the large error bars are a consequence of the small strength in the investigated angular range compared to the monopole contribution. On the another hand, the dipole distribution seems to have no sensitivity in the whole energy range. The reason is that the dipole angular distribution is significant only after the first minimum of the monopole cross section, i.e., center-of-mass angles above 2° . In fact, the efficiency of the MDA for the multipoles $L \geq 1$ depends on the angular range which is covered for the fit. For future experiments it would be quite

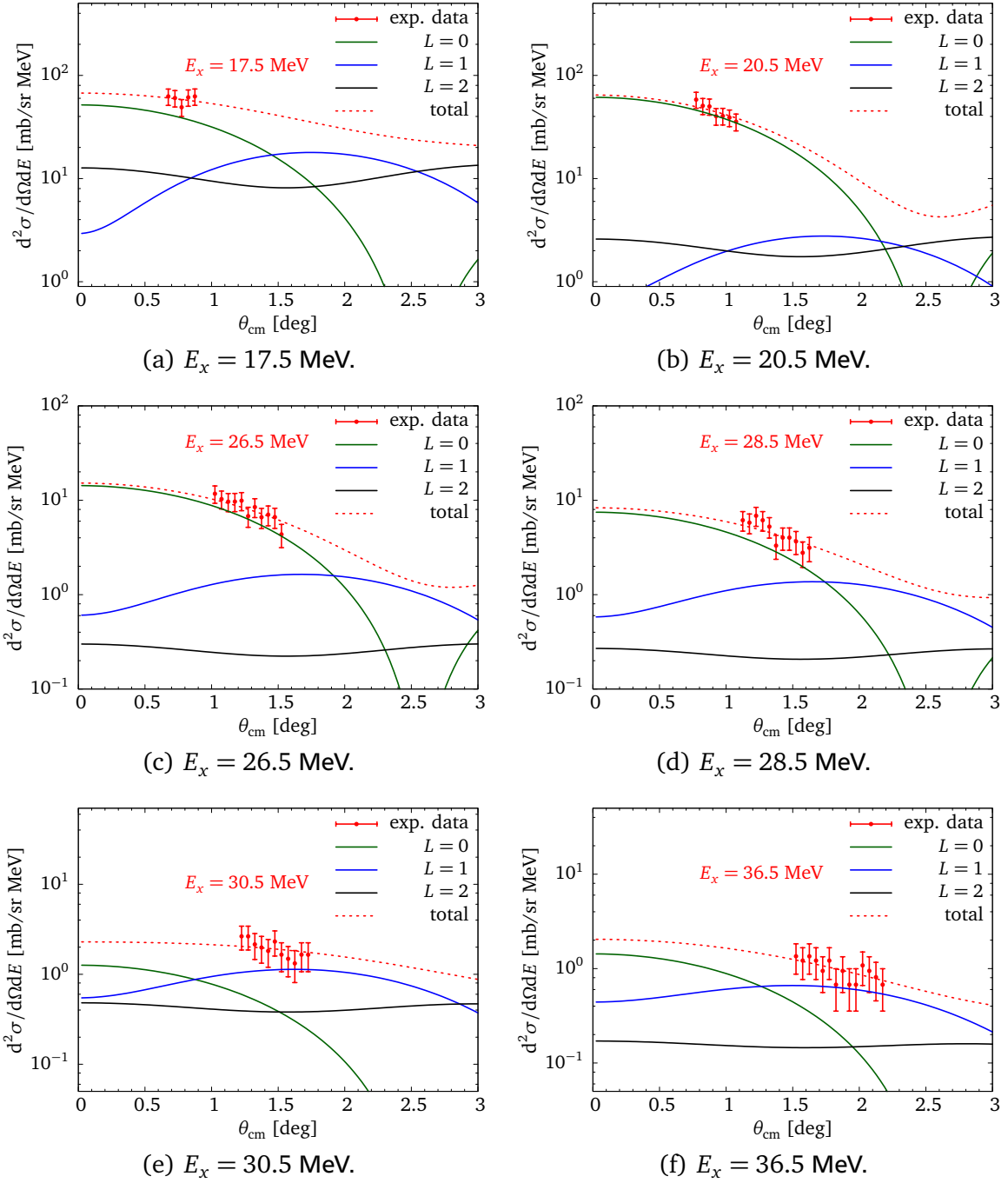


Figure 6.13.: Multipole decomposition analysis for different energy bins of 1 MeV width. The points correspond to the experimental angular distributions and the solid lines are the DWBA calculations for the L^{th} multipole. The dashed line is the total fitted angular distribution.

important to perform measurements in an angular range from 1 to 5° , which has proven great success in the decomposition of the contributions up to $L = 7$ [4, 65].

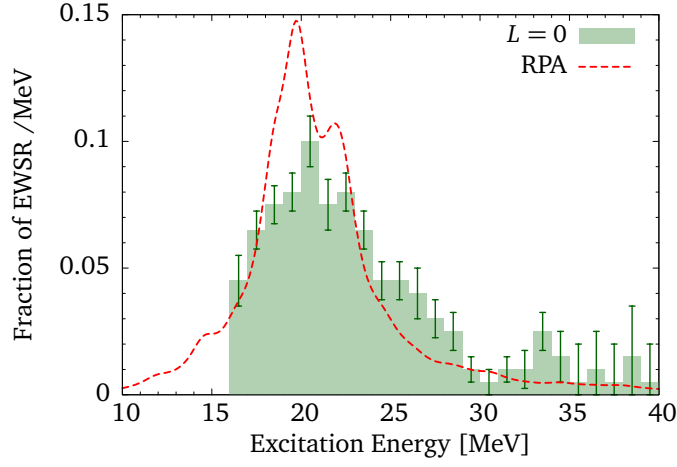
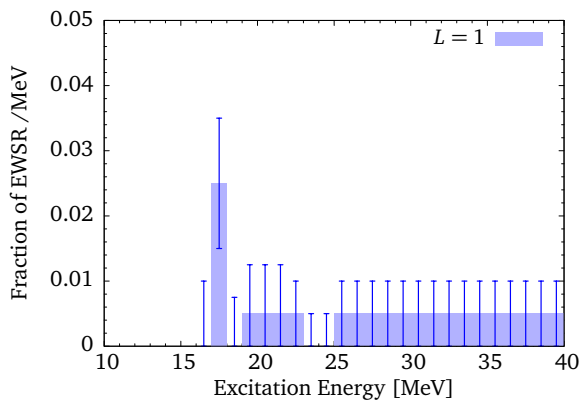


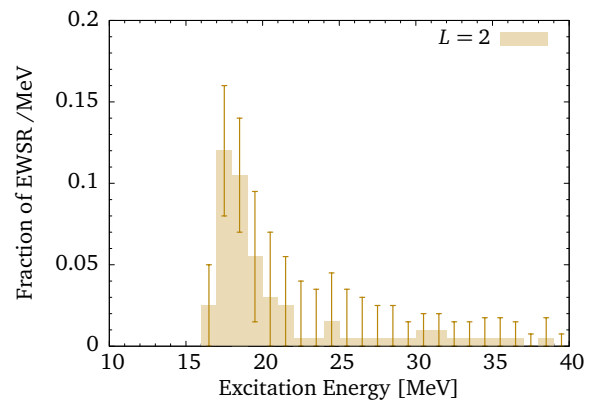
Figure 6.14.: Fraction of the EWSR for the monopole contribution assuming the background parametrization 2. The histogram bars are the coefficients from the fit of each excitation energy bin. The dashed line is the prediction by a RPA calculation for this multipole with the Skyrme interaction Sk0'.

Reference	m_1/m_0 [MeV]	$\sqrt{m_3/m_1}$ [MeV]	Width _{rms} [MeV]	EWSR [%]
this work ¹	21.1(5)	21.6(6)	3.0(5)	53(8)
this work ²	21.4 ^{+0.5} _{-0.6}	21.9 ^{+0.8} _{-1.1}	3.4 ^{+0.5} _{-0.6}	79 ⁺¹² ₋₁₁
this work ³	21.5 ^{+0.8} _{-0.9}	22.3(1.0)	3.5(6)	106(12)
RPA	20.04	21.20	3.24	109
[119]	20.30 ^{+1.69} _{-0.14}	21.48 ^{+3.01} _{-0.32}	4.25 ^{+0.69} _{-0.23}	74 ⁺²² ₋₁₂
[65]	19.20 ^{+0.44} _{-0.19}	20.81 ^{+0.90} _{-0.28}	4.89 ^{+1.05} _{-0.31}	85 ⁺¹³ ₋₁₀
[4]	19.9 ^{+0.7} _{-0.8}	-	-	92 ⁺⁴ ₋₃

Table 6.5.: ISGMR parameters extracted from the multipole decomposition analysis. The index number are for the results of this work for the different background parameterizations shown in Fig. 6.12(a). The present values correspond to the analysis of the distributions in the energy range from 10 to 30 MeV only.



(a) Dipole.



(b) Quadrupole.

Figure 6.15.: Fraction of EWSR for the dipole and quadrupole contributions from the MDA.

6.3 Transfer reaction

The last type of nuclear reactions studied in this work is a neutron transfer observed in the run $^{20}\text{Ne} + p$. In this experiment, deuteron recoils were produced through a neutron pick-up by the hydrogen target, what also turns the ejectile particle into ^{19}Ne . The minimum energy required for the occurrence of this reaction is -14.6 MeV (Q value), which is fully covered by the center-of-mass energy of 48 MeV. Due to the kinematics of the reaction, the scattering angles of these deuterons are limited to the forward region in the laboratory system, namely below 35° for the present experiment. This means that the angles covered by DSSD2 are adequate for the measurement of such transfer reactions. However, the kinetic energy at which these recoils are produced is much higher than 30 MeV, and therefore, only an energy loss is deposited in the detector. A way to identify this reaction channel is by a comparison with a simulation that takes the respective kinematics and the deuteron energy loss in the detector into account. In a first approximation, we can assume a transfer to the ground state of ^{19}Ne , although a transfer could also happen to an excited state. In Fig. 6.16(b) the simulated energy loss of these deuterons for the respective laboratory angles is shown. The maximum scattering angle (in lab.) is about 35° which corresponds to a center-of-mass angle of 50° . In strips at more forward angles, the deuteron energy loss is splitted in two parts because two different center-of-mass angles are measured at the same θ_{lab} . Similarly, this trend is visible in the experimental spectrum, shown in Fig. 6.16(a), where the dashed line was included to show the deuteron kinematics. At energies larger than 1 MeV the transfer products are easily distinguishable, but below this value the separation of the transfer reaction channel becomes more difficult due to the overlap with inelastically scattered recoils. In this case, depending on a good background parametrization, the deuteron events are still separable at the low energy region.

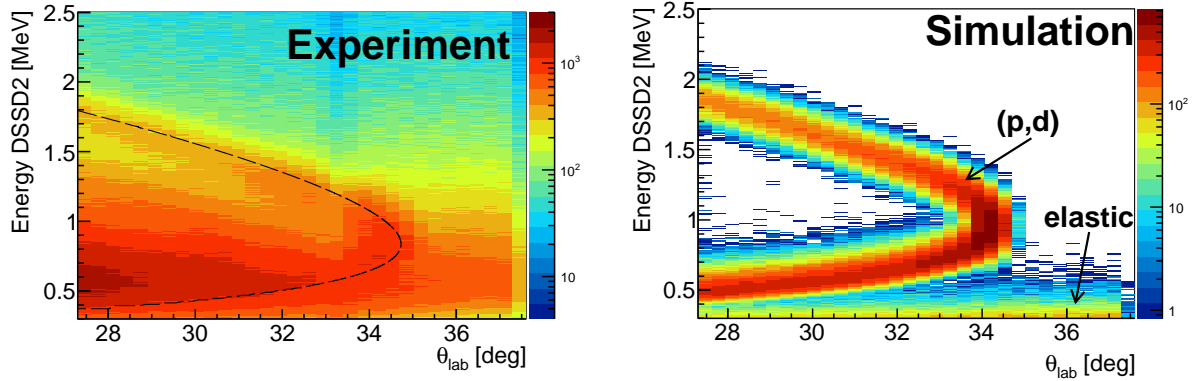
The analysis of this reaction channel is performed from the individual energy spectra of the p -side strips. For an optimal identification, the energy peak position deduced from kinematics and energy loss is required for each spectrum. For instance, in strip #0 ($\theta_{\text{lab}} = 27.5^\circ$) the most predominant peak from the transfer reaction is located around 1850 keV, while at more backward angles the (p, d) contribution is found at lower energies, as seen in Figs. 6.16(c), 6.16(d) and 6.16(e). The experimental spectra of strips 25 to 31, which correspond to scattering angles larger than 35° (in lab.), are free of a transfer reaction component. So, the shape of these spectra can give us an idea of the type of background component to be subtracted for the analysis of this reaction. As an example, in Fig. 6.16(e) the spectrum of strip #30 is shown. In order to fit this spectrum, a superposition of a log-normal and a Gaussian function was employed

$$B(x) = A \left[\frac{a}{x} \exp \left(-\frac{(\ln(x) - \mu_1)^2}{2\sigma_1^2} \right) + \exp \left(-\frac{(x - \mu_2)^2}{2\sigma_2^2} \right) \right], \quad (6.27)$$

where $a = 949.3$, $\sigma_1 = 0.5$, $\mu_2 = 538.5$ keV and $\sigma_2 = 189.0$ keV were found by fitting the background component of the last strips. These parameters were fixed during the fit for the rest of strips. Thus, given this parametrization, only the amplitude A and the value μ_1 were varied to fit each spectrum. Besides, this parametrization was employed to determine the background contribution for each strip of the detector. In Figs. 6.16(c), 6.16(d) and 6.16(e) the very good results in the fitting of the experimental data are illustrated.

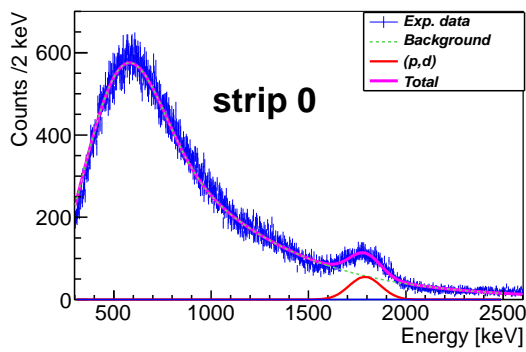
Another important aspect during the data reduction was the identification of possible excited states. As commented before, the transfer reaction does not populate only the ground state but also some of the low-lying states of ^{19}Ne . However, we must know the peak position of the possible excited states in order to fully identify the states populated by the transfer reaction. In Fig. 6.17 the level scheme of ^{19}Ne up to 2 MeV excitation energies is shown.

As can be noticed, the spin and parity of the ground state is $J^\pi = 1/2^+$. The first two excitation levels ($5/2^+$ and $1/2^-$) are separated by less than 300 keV from the ground state, and the next levels are at excitation energies above 1.5 MeV. This information can be employed to perform simulations of the

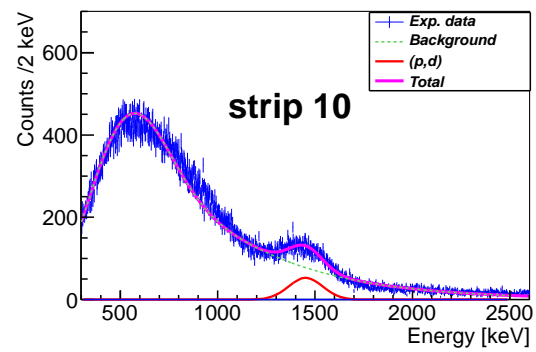


(a) Experiment.

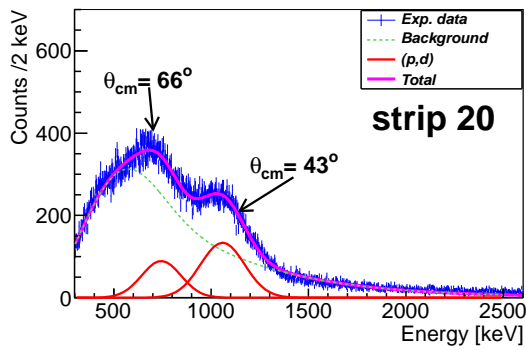
(b) Simulation.



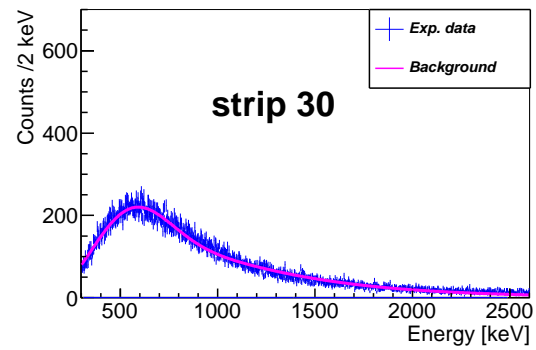
(c) Experimental spectrum, strip 0.



(d) Experimental spectrum, strip 10.



(e) Experimental spectrum, strip 20.



(f) Experimental spectrum, strip 30.

Figure 6.16.: Comparison of experimental and simulation results for the transfer reaction $^{20}\text{Ne}(p,d)$ at 50 MeV/u in DSSD2. The kinematic line for this reaction channel is visible in the energy loss spectrum, and it is highlighted by the dotted line. On the bottom there are four samples of experimental strip spectra.

transfer reaction and the respective population of excited states. The idea is to obtain the expected widths and peak positions for each excited state in the energy spectra. For this task, we can also assume the same probability for each transition. The simulation results for strip number 0 at $\theta_{\text{lab}} = 27.5^\circ$ are presented in Fig. 6.18.

The resulting energy spectrum from the population of the ground state is centered around 1850 keV with a standard deviation $\sigma \simeq 77$ keV. Also, the contributions from the two first excited states of ^{19}Ne are just separated by 25 keV from the ground state peak. Even the contribution from the $5/2^-$ state at 1507 keV

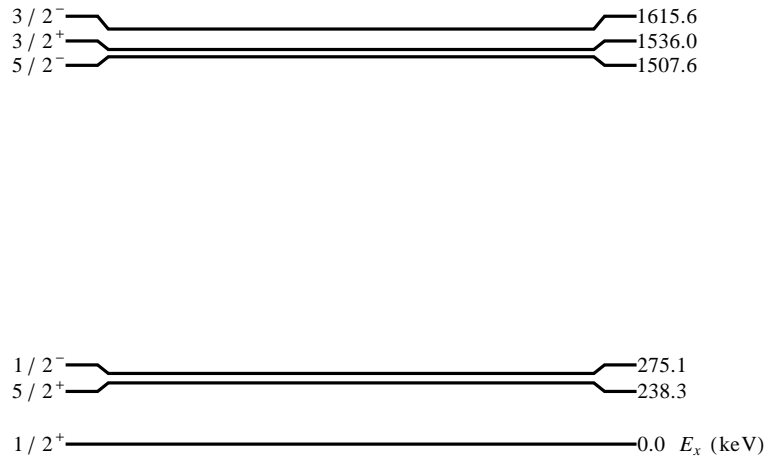
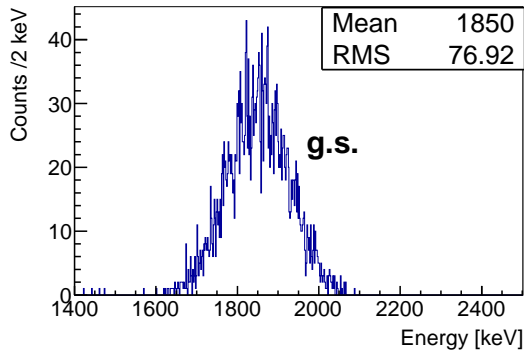
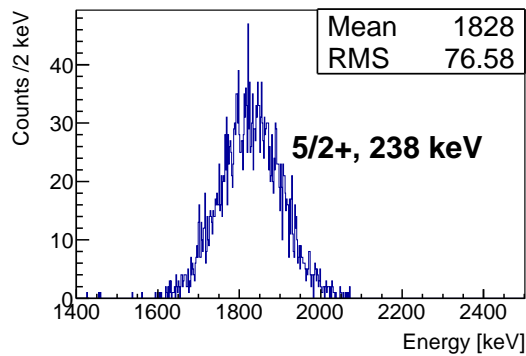


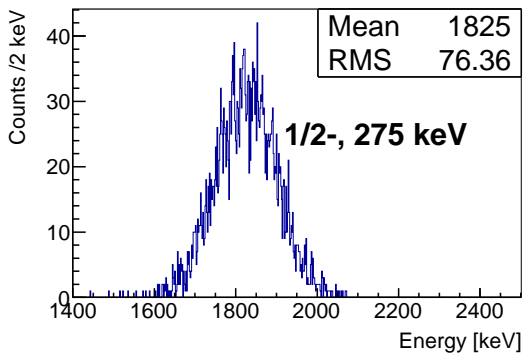
Figure 6.17.: Level scheme of ^{19}Ne for states up to 2 MeV. Data extracted from Ref. [103]. (This figure was created with the code LevelScheme [122])



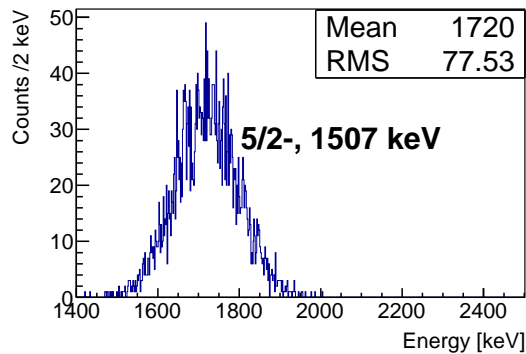
(a) Population of the ground state. The peak is centered around 1850 keV.



(b) Population of the $5/2^+$ state at 238 keV. The peak is centered around 1828 keV.



(c) Population of the $1/2^-$ state at 275 keV. The peak is centered around 1825 keV.



(d) Population of the $5/2^-$ state at 1507 keV. The peak is centered around 1720 keV.

Figure 6.18.: Simulation results of the transfer reaction to different final states. The spectra correspond to the strip number 0 of DSSD2 ($\theta_{\text{lab}} = 27.5^\circ$).

overlaps with the other peaks because its separation is lower than two 2σ of the distribution. The same behavior was observed in the energy spectra of the other strips. A direct consequence of these results is that the experimental peaks from this transfer reaction (see Fig. 6.16) can be a mixture of more than

one final state. For this reason, the best way to study this experimental data is from a decomposition of the angular distribution, as shown in the previous section. The decomposition allows an optimal identification of the individual final configurations and the possibility to extract important information about the nuclear structure of the ^{19}Ne hole-states. Therefore, in the present analysis we describe the experimental angular cross section as a superposition of the final configurations [68]

$$\left(\frac{d\sigma}{d\Omega}\right)^{\text{exp}} = \sum_{\ell sj} S_{\ell sj} \left(\frac{d\sigma}{d\Omega}\right)_{\ell sj}^{\text{cal}}, \quad (6.28)$$

where only one value each of s and ℓ are allowed. For the present (p, d) reaction, this is $s = 1/2$ and $\ell = 0, 1, 2, 3$, i.e., for the ground state orbital $2s_{1/2}$ and the excited states $1d_{5/2}$, $1p_{1/2}$, $1f_{5/2}$, $1d_{3/2}$ and $1p_{3/2}$. The coefficients $S_{\ell sj}$ are the corresponding spectroscopic factors which relate our experimental results with the calculated angular distributions. Now the problem is to obtain consistent theoretical angular distributions to describe the different configurations. One common method is to perform DWBA calculations [7, 123]. Nevertheless, as the deuteron recoil has a relative low separation energy (2.2 MeV), the breakup channel of this particle can have some effect in the total measured angular distribution, what in turn can lead to imprecise results for the spectroscopic factor [124]. A popular method to take the breakup into account is by the definition of an adiabatic potential for the usual deuteron OMP in the exit channel [125]. This adiabatic potential is an effective interaction of $^{19}\text{Ne}-d$, which accounts the effects of coupling to the continuum states of the deuteron nucleus. When such interaction is included in a standard DWBA calculation, the method is called **Adiabatic Distorted Wave Approximation (ADWA)** [126]. There are different ways to obtain the adiabatic potential, but in this work we used CDCC (**Continuum Discretized Coupled Channel**) calculations to deduce the continuum coupling effects explicitly [127]. The principle of the CDCC method is explained in Appendix C. Under this approximation, the adiabatic potential is composed by three terms

$$U_{\text{adia}} = U_{\text{C}} + U_{\text{bare}} + U_{\text{DPP}}, \quad (6.29)$$

where U_{C} is the Coulomb potential and U_{bare} the cluster-folding interaction of the proton and neutron (components of the deuteron) particles with the ^{19}Ne nucleus, i.e.

$$U_{\text{bare}} = \langle \phi_{\text{gs}} | V_{19\text{Ne}-p} + V_{19\text{Ne}-n} | \phi_{\text{gs}} \rangle,$$

with the deuteron ground-state wave function ϕ_{gs} . The last term U_{DPP} is the dynamical polarization potential which simulates all effects of coupling with the continuum [127]. The code **FRESCO** provides an average output of this interaction which is known as **Trivial Local Polarization (TLP)** potential, that can be regarded as a simplified local approximation of a complicated coupled channel system [128].

In order to test the consistence of the adiabatic potentials, CDCC calculations have been performed for the system $^{20}\text{Ne} + d$ at 52 MeV, where the respective experimental elastic cross section is reported in Ref.[129]. In this case, the bare interaction was built from the proton and neutron global OMPs from Koning-Delaroche [86]. The deuteron continuum was discretized up to 50 MeV in bins of 5 MeV, for each of the S and D waves. The result of the elastic scattering is presented in Fig. 6.19(a). As can be noted, the deuteron breakup effect (included in the full coupling) is not too strong compared to the result taking into account the bare interaction only. These effects are mostly visible at backward angles, above 20° . In terms of the reaction cross section, the analysis with only the bare potential results in $\sigma_{\text{rea}} = 1112$ mb, while this value increases to $\sigma_{\text{rea}} = 1167$ mb by using the full coupling. This means the cross section of the deuteron breakup is about 55 mb, which is an effect of only 5% in all reaction channels. For the system $^{19}\text{Ne} + d$ at 36 MeV (Fig. 6.19(b)), which is of interest for our ADWA calculations, the trend is quite similar. The breakup channel plays a moderate role only at backward angles. In this case, the deuteron breakup cross section is $\sigma_{\text{breakup}} = 74$ mb, about 7% of the reaction cross section.

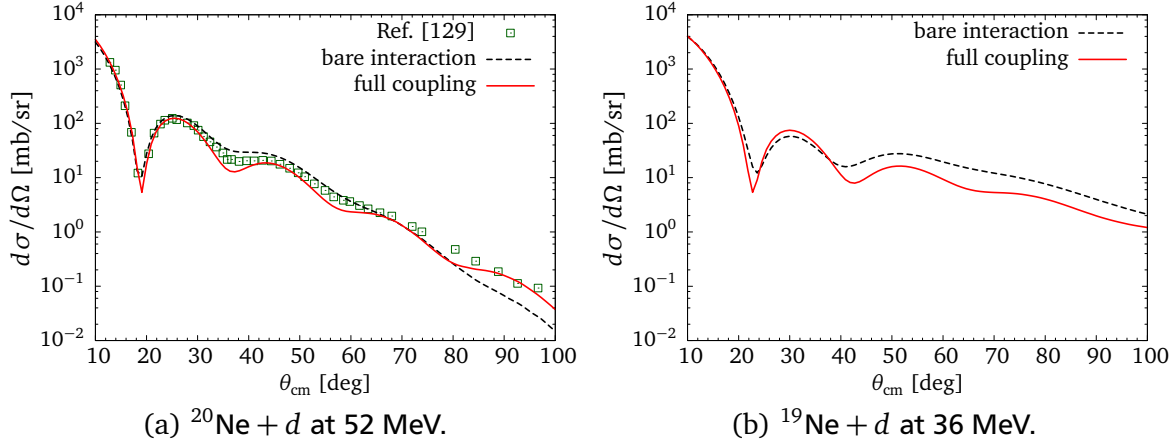


Figure 6.19.: CDCC calculations to account the deuteron breakup effect in the systems: $^{20}\text{Ne} + d$ at 52 MeV and $^{19}\text{Ne} + d$ at 36 MeV. The respective elastic cross sections are shown in the cases of full continuum coupling and bare interaction.

As commented before, the effective interaction of the breakup channel is obtained from the previous calculation. In Fig. 6.20 the result for the different components of the adiabatic potential is shown. As in the nuclear interior the bare interaction has a stronger contribution, the polarization potential (which contains the continuum coupling) is almost insensitive. Therefore, the most significant contribution of this potential is located at the peripheral region. The real part presents a repulsive effect neighboring to the reaction radius, what is a natural characteristic of the breakup channel [127]. Moreover, the imaginary part of the polarization potential is absorptive at the surface, which also enhances a reduction in elastic cross section due to the inelastic channels.

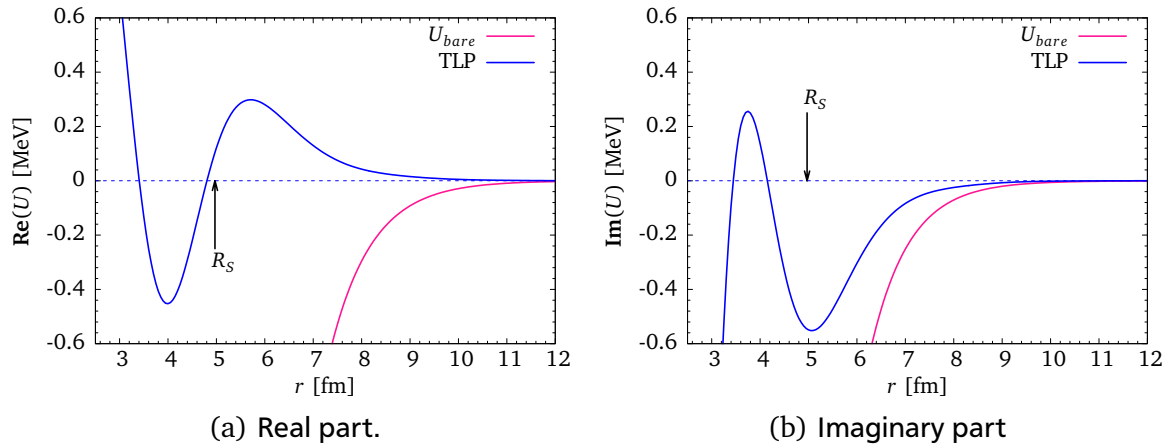


Figure 6.20.: Peripheral region of the bare and polarization potentials for the system $^{19}\text{Ne} + d$. The arrow corresponds to the radius of the reaction, $R_S = 1.25(A_T^{1/3} + A_P^{1/3})$.

Besides this interaction, other potentials, which are also needed for the ADWA calculations, can be found in Table. 6.6. In the entrance channel ($^{20}\text{Ne} + p$) the OMP employed is the same that was used to successfully describe the elastic scattering in first section of this chapter [6]. The core-core interaction ($^{19}\text{Ne} + p$) is the global potential from Koning-Delaroche [86], the same used to calculate the bare interaction for the CDCC calculations. The binding potential of the deuteron was assumed as a Gaussian shape with the parametrization suggested in Ref. [130].

The present finite-range ADWA calculations were performed in the prior representation where the ^{20}Ne bound state potential was taken as a Woods-Saxon type. Its radius and diffuseness were kept fixed while

System	V_V [MeV]	r_R [fm]	a_R [fm]	W_V [MeV]	W_D [MeV]	r_D [fm]	a_D [fm]	V_{so} [MeV]	r_{so} [fm]	a_{so} [fm]	r_C [fm]
$^{20}\text{Ne} + p$	36.33	1.20	0.75	11.31	0.18	1.20	0.79	-	-	-	1.25
$^{19}\text{Ne} + p$	38.44	1.15	0.67	5.58	4.10	1.30	0.53	4.74	0.94	0.59	1.39
$n + p$ (*)	72.15	-	1.48	-	-	-	-	-	-	-	-
$^{19}\text{Ne} + n$ (†)	adjusted	1.25	0.65	-	-	-	-	-	-	-	-
$^{19}\text{Ne} + d$ (‡)	81.50	1.17	0.80	-	20.39	1.33	0.58	3.70	1.23	0.81	1.70

Table 6.6.: Optical model potential parameters used for the ADWA calculations. All radii are given in the reduced form $R_x = r_x A_t^{1/3}$. (*) is a Gaussian-shape potential. (†) the depth was adjusted while keeping the shape fixed until the binding energy is matched by FRESKO. (‡) potential employed only for the DWBA calculation.

the potential depth was adjusted by the code to match the binding energy. As commented before, six final states were included in our calculations: $2s_{1/2}$, $1d_{5/2}$, $1p_{1/2}$, $1f_{5/2}$, $1d_{3/2}$ and $1p_{3/2}$. Eq. (6.28) was used to fit the experimental angular distribution to the theoretical cross sections for these six states. The minimization code employed for this procedure was the same as the one utilized for the MDA. The result of this analysis, together with the experimental angular distribution, is presented in Fig. 6.21(a). The negative parity states ($1p_{1/2}$, $1f_{5/2}$ and $1p_{3/2}$) have no contribution to the total angular distribution (fitted coefficients were zero). Only the ground and the $1d$ excited states were populated in the measured angular range. The angular distribution for $\ell = 0$ has the most significant contribution at forward angles, below 35° .

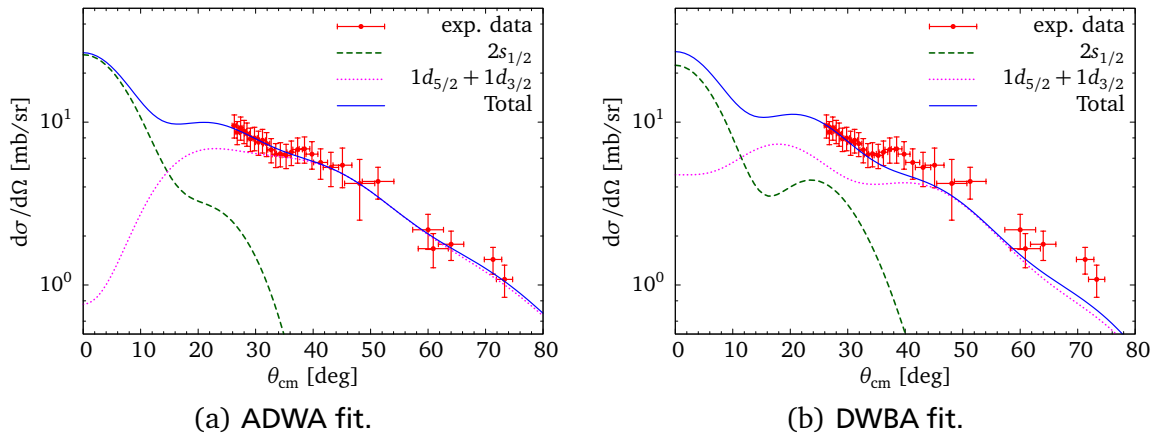


Figure 6.21.: Experimental angular distribution for the transfer reaction $^{20}\text{Ne}(p, d)^{19}\text{Ne}$. The data is described by a superposition of the orbitals $2s_{1/2}$, $1d_{5/2}$ and $1d_{3/2}$. It was not possible to separate the contribution from the angular momentum $\ell = 2$ in the spin orientations $5/2^+$ and $3/2^+$. An alternative analysis was performed using DWBA calculations (see the text for details).

The states with the transferred angular momentum $\ell = 2$ are favored at backward angles, above 40° . However, as the angular distribution from the states $1d_{5/2}$ and $1d_{3/2}$ are equivalent, a separation of these two contributions was not possible. Therefore, only information about the total shell $1d$ was available. Eventually, from the present analysis the corresponding spectroscopic factors are extracted. The respective can be found results in Table 6.7.

For the ground state the spectroscopic factor found in the fit analysis with the ADWA angular distributions is 0.48(9). This value is in perfect agreement with the prediction from a shell model calculation performed with the code ANTOINE [131]. For this calculation, a sd valence space (^{16}O core) configura-

ℓ	Orbital	Spectroscopic Factors		
		SM	ADWA	DWBA
0	$2s_{1/2}$	0.48	0.48(9)	0.49(7)
	$1d_{5/2}$	1.24		
2	$1d_{3/2}$	0.27		
	Total	1.51	1.53(20)	1.98(19)

Table 6.7.: Spectroscopic factors obtained in the analysis of the angular distribution with ADWA and DWBA calculations. The values are compared with the predictions from a shell-model calculation (SM).

tion was assumed, with the very popular interaction USDB [132]. On the another hand, the spectroscopic factor from the population of the $1d$ states is given by the sum over the two possible j values

$$S_\ell = \sum_j S_{\ell j}, \quad (6.30)$$

with $\ell = 2$ and $j = \{5/2, 3/2\}$. The total contribution extracted from the ADWA analysis is 1.53(20), which is also in perfect agreement with the shell model prediction. Additionally, one should note that the sum of these experimental spectroscopic factors already exhaust the occupancy number

$$\sum_{\ell j} S_{\ell j} = 2.01(22). \quad (6.31)$$

Finally, the present results can also be compared with an analysis performed from DWBA calculations in Fig. 6.21(b). In this case, the exit channel OMP was taken from a global systematics for deuterons of Ref.[133], for which the corresponding parameters can also be found in Table. 6.6. Due to some inconsistencies in the extraction of the spectroscopic factors, only angles up to 35° were fitted. The result of the population of the ground state is in very good agreement with the shell model prediction and with the result from the ADWA analysis. However, the total contribution from the $1d$ shell is about 31% larger than the other two cases. This effect could be related with the deuteron breakup contribution, but also an OMP dependence in the output channel is expected. For a more conclusive analysis it would be preferred to fit experimental data at more forward angles.

Summary and conclusions

In this thesis, nuclear reactions are investigated in experiments performed with the stored ^{58}Ni and ^{20}Ne beams at the storage ring ESR. For these experiments, internal gas-jet targets of hydrogen and helium were employed with densities in the order of 10^{12} and 10^{13} part./ cm^2 , respectively. These low target densities were compensated by the revolution frequency of the stored beam, which was in the range of MHz. Eventually, significant luminosities of up to 10^{27} $\text{cm}^{-2}\text{s}^{-1}$ were achieved in the present experiments.

From the technical point of view, one of the most challenging parts in the execution of the experiments was the detector setup operation. On the one hand, during the preparation of the experiments the detector system was adapted to tolerate temperatures of up to 150 °C (for a week) in order to reach the ultra high vacuum conditions. On the other hand, the detector setup included double-sided silicon-strip detectors (of 285 μm thickness) operating as active barriers between the ultra high vacuum of the storage ring and an auxiliary vacuum of internal pockets of the experimental chamber. This detector setup permitted us to measure low energy recoils (hundreds of keV) successfully, since both target and detectors were windowless. These type of measurements are essential for the investigation of nuclear reactions in inverse kinematics at very low momentum transfer. The satisfactory performance of this detector configuration is of great importance for the research of detector compatibility with ultra high vacuum conditions and, in particular, for future applications within the EXL project.

Parallel to the experiments, dedicated simulations with the GEANT4 toolkit were performed. These simulations helped us to understand detector properties which were investigated in preparatory in-beam experimental tests. Also, simulations of the detector setup utilized for the present work were essential in the analysis of the experimental data. These simulations were applied for the reaction channel identification as well as to obtain the angular calibrations and solid angle acceptance of the detector system. Moreover, extended versions of detector setups for upcoming experiments are studied with our simulations. For instance, the full ESPA detector recoil of EXL was implemented in this work and was tested with some reaction channels foreseen for future experiments with EXL (see Appendix B). The present simulations routines are the starting point of a full simulation framework for the EXL collaboration.

In the experimental data of this thesis different reaction channels were identified. The analysis of this data was divided in three main parts which are discussed below:

Elastic scattering and excitation of low-lying states

- The angular distribution of elastically scattered protons by the stored ^{20}Ne beam (at 50 MeV/u) was measured in the center-of-mass range from 7° to 30° . The respective differential cross section

was analyzed with three distinct optical potentials, where the most successful in the description of the experimental data was a density-folding potential with the M3Y interaction. By studying the absorption probability deduced from the analysis of each potential, a RMS point-matter radius of 2.86(8) fm was obtained, which is in very good agreement with experimental results found in literature. However, the method employed for deducing the RMS radius in this work is dependent on the optical potential shape. In this case, a folding model potential is recommended to reduce the number of free parameters of the optical potential.

- In the same experiment, $^{20}\text{Ne} + p$, the first excited state of ^{20}Ne (2_1^+ state at $E_x = 1.63$ MeV) was measured. DWBA calculations were performed to fit the experimental angular distribution of the excited state. A nuclear deformation $\beta_2 = 0.68(6)$ was extracted. This result is consistent with the deformation parameter deduced from experiments with electromagnetic probes.
- Elastic scattering of $^{58}\text{Ni} + \alpha$ was measured at 100 and 150 MeV/u. The experimental angular distributions were successfully described with theoretical differential cross sections deduced from three distinct folding potentials. Since at the present energies and measured angles the eikonal approximation is already valid, a fit of the experimental data was done with the optical limit of the Glauber theory. In this case, a Fermi shape was assumed for extracting the ^{58}Ni matter density-distribution. The resulting RMS point matter-radii are 3.68(10) fm and 3.64(9) fm for the measurements at 100 and 150 MeV/u, respectively. The presented values are in very good agreement with results from several experiments with proton and alpha scattering which were done in normal kinematics in the past.

Isoscalar giant resonances excitation

The excitation of isoscalar giant resonances was studied in the experiment $^{58}\text{Ni} + \alpha$ at 100 MeV/u. In this case, inelastically scattered α recoils in excitation energies above 15 MeV were measured. The angular coverage of the detector setup permitted measurements in the center-of-mass angles from 0.5° to 1.5° . In the double-differential cross section, a well-defined peak in the energy range from 15 to 30 MeV was obtained. A fit with a Lorentz function for the ISGMR component resulted in a centroid in 19.27(61) MeV and a width of 6.45(51) MeV. Moreover, a multipole decomposition analysis was done by fitting the angular distributions of different energy bins. The theoretical angular distributions for the fits were derived with DWBA calculations where transition potentials explicitly deduced from a folding-model were used. The extracted strength of the ISGMR exhausts 79_{-11}^{+12} % of the Energy-Weighted Sum Rule (EWSR). The results are consistent with the analysis of other experiments performed in the past in normal kinematics as well as theoretical predictions. This is a clear demonstration for the feasibility of prospective studies with stored radioactive beams. New experiments are already planned with an extended detector setup for the investigation of isoscalar giant resonances in the doubly magic nucleus ^{56}Ni .

Transfer reaction

A neutron transfer reaction was measured in the experiment with the stored ^{20}Ne beam. Deuteron transfer-products were observed in laboratory angles from 27° to 35° , which corresponded to the center-of-mass region between 26° and 72° . In this experiment, the contribution of the transfer to the ground state and low-lying states of ^{19}Ne were kinematically not separable. In order to disentangle the different components, a multipole decomposition analysis was applied to the experimental data. In this analysis, the deuteron breakup channel also was taken into account. The result shows that the most significant contribution at angles up to 35° is from the $2s_{1/2}$ orbital. At more backward angles a superposition of the orbitals $1d_{5/2}$ and $1d_{3/2}$ ($\ell = 2$) is dominant. The spectroscopic factors deduced in this analysis are

in very good agreement with the predictions from shell model calculations.

Overall, the results of this work demonstrate the feasibility of nuclear reaction studies with stored ion-beams by using an in-ring detector system. This also provides a proof of principle of the EXL project which in the future will apply these experimental techniques to investigate nuclei far away from the valley of stability. A first step to implement this technique with a stored radioactive beam was already demonstrated in an experiment from the same EXL campaign [23, 36].



Preparatory works for EXL

On the way to the construction and development of the detection system for the EXL project, an in-beam demonstrator test was done at the cyclotron accelerator at KVI [134]. For this test, three types of detectors were employed: DSSDs (Double sided Silicon Strip Detector) of $285\ \mu\text{m}$ thickness, Si(Li) with a thickness of 6.5 mm and CsI scintillation crystals. The experimental setup consisted of two DSSDs and Si(Li) detectors which were placed in sequence inside of a vacuum chamber in order to record the energy deposited by the proton beam that impinges the detector system. Eventually, two CsI crystals were mounted at the rear part of the chamber to stop the protons completely. In the Fig. A.1 is shown a schematic illustration of the experimental setup.

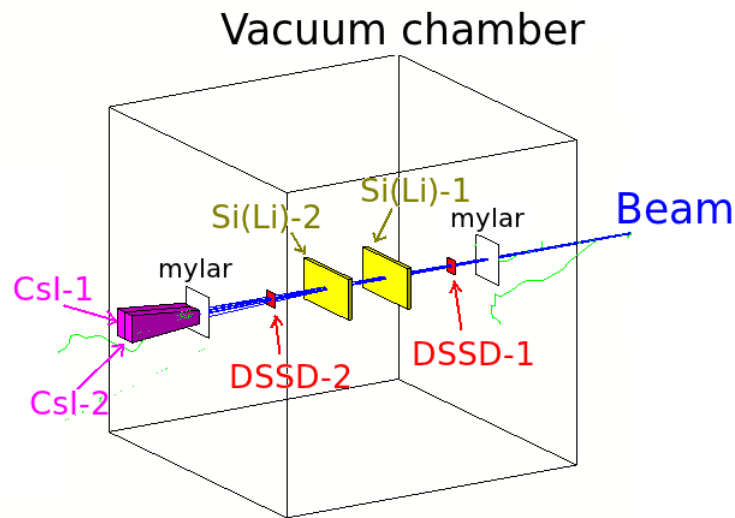


Figure A.1.: Schematic illustration of the experimental setup used for the in-beam test at KVI. The silicon detectors are placed inside of a vacuum chamber while the CsI crystals are placed outside for stopping the beam particles completely.

The beam energy was set to 133 MeV, which is sufficient to punch through the chamber windows, silicon detectors and to be stopped in the CsI crystals.

Many questions arose when the experimental results were compared to simple simulations, which did not take into account the correlations between neighboring detectors and cross-talk (signal-partitioning) effects. In principle, these simulations were done under the assumption that all detectors are independent, i.e., that there is no signal correlation between a couple of neighboring detectors. Then, the only

possible correlation are leaked particles among them. For comparison, Fig. A.2 shows two examples of experimental energy spectra and these simple simulations.

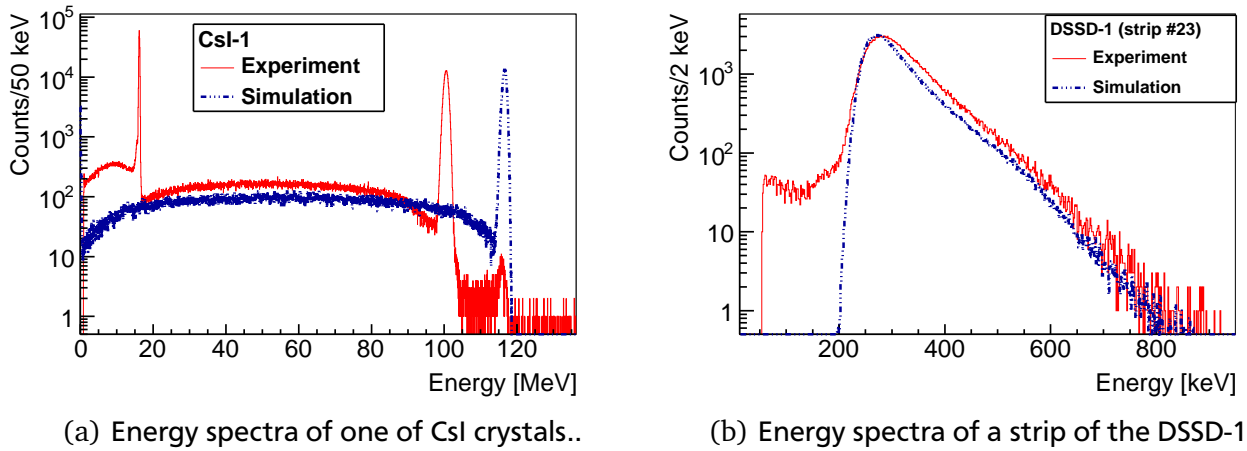


Figure A.2.: Example of the experimental results in comparison with the simulations. In this case the simulations are performed without signal correlation.

Surprisingly, the experimental spectra for the CsI detector (Fig. A.2(a)) show two peaks and it seems that the position of the total energy absorption peak is reduced by about 20 MeV. In principle, only one peak (total absorption) and a smooth background at lower energies due to proton inelastic scattering and not completely absorbed particles in the crystals was expected. Similarly, the experimental energy spectra for the individual strips of the DSSDs present a different peak shape than the ones expected by these simple simulations (Fig. A.2(b)). The experimental peak seems to be wider than the simulated one, mainly at low energies where the experimental spectrum has a large extension, probably because charge partitioning between neighboring strips in the DSSD.

Below, these two cases will be studied in more detail.

A.0.1 Crystal correlation (Light leakage)

In this demonstrator test a two-channels Photonis XP14D5 square photomultipliers [135]. In Fig. A.3 a couple of pictures of this double-photomultiplier and the CsI crystals can be seen.

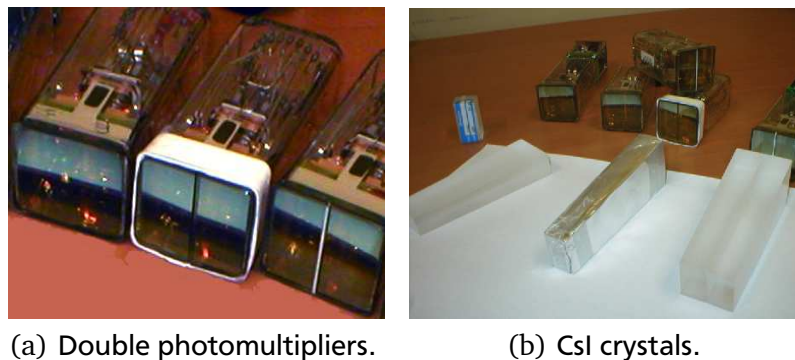


Figure A.3.: Pictures of the CsI crystals and the double photomultipliers used in the demonstrator test. With this device, two crystals can be coupled in a side by side mode.

However, this arrangement could bring light leakage problems, e.g., due to bad gluing or simply from light transmission through the boundary between the crystals and photocathodes. This could mean that

not all optical photons created in one of the crystals are detected on its respective photocathode. Thus, a certain percentage of them could also arrive at the neighboring photocathode. In order to gain a better understanding of this PMT prototype, we made a simulation of the PMT-crystals coupling. For this simulation, the *Scintillation process class* of GEANT4 was employed. This routine permits to create optical photons when the ionizing particles deposit energy in the scintillator material. Then, these particles are transported inside the crystal using light optical properties until they reach the photocathode. For the present simulation, realistic geometries and materials are assumed. Likewise to the experiment, the crystals were wrapped in aluminum to prevent the escape of photons and coupled to the frontal window of the PMT. This window is made of an optical borosilicate-glass that has a refractive index compatible to the CsI crystal (at the wavelength of the photons produced in the crystals). On the other side of the window, the two photocathodes, made of a bialkali material (Sb-Rb-Cs), were placed for the collection of the light. In Fig. A.4(a) an illustration of the simulated setup is shown.

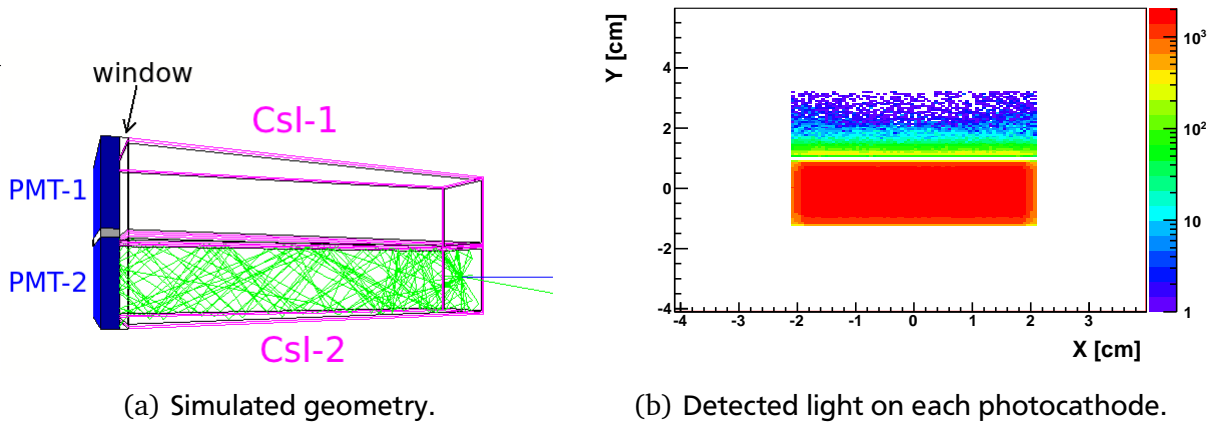


Figure A.4.: Simulation using the *Scintillation process class*. Two CsI crystals are wrapped with aluminum and connected by the same window to the double photomultiplier. The green lines correspond to optical photons. On the left side the detected light intensity in each photocathode is shown when only one of the crystals is illuminated.

The aim of this simulation is to quantify the number of photons that are detected on the photocathodes when only one crystal is illuminated. One of the results of this simulation can be seen in Fig. A.4(b), which is a plot of the light intensity detected in each photocathode. As one can see, even with a “perfect” gluing there is still a certain amount of photons that are detected in the neighboring photocathode. About 2% of the total light intensity produced in one crystal is leaked. This value might also change depending on the thickness of the PMT window, but it does not explain the experimental results shown in Fig. A.2(a) completely.

To simulate higher order correlations between neighboring crystals, it is convenient to manipulate the ADC signals at every event. The problem can be described as a linear transformation

$$\begin{pmatrix} N'_1 \\ N'_2 \end{pmatrix} = \begin{pmatrix} 1 - \alpha & \alpha \\ \alpha & 1 - \alpha \end{pmatrix} \begin{pmatrix} N_1 \\ N_2 \end{pmatrix}, \quad (\text{A.1})$$

where N_1 and N_2 are the processed digits per event (proportional to the number of detected photons) in each detector, and α is the light cross-talk percentage that can be calculated by the ratio (R) of the channel position for the two experimental peaks of Fig. A.2(a)

$$\alpha = \frac{R}{1 + R}. \quad (\text{A.2})$$

For example, in the present case a value $R = 0.15$ was obtained. This implies a cross-talk of 13% of the total signal amplitude. The transformation of eq.(A.1) is then applied for each event in the simulation.

Finally, our results are in very good agreement with the experiment, as we can see in Fig. A.5 and Fig. A.6.

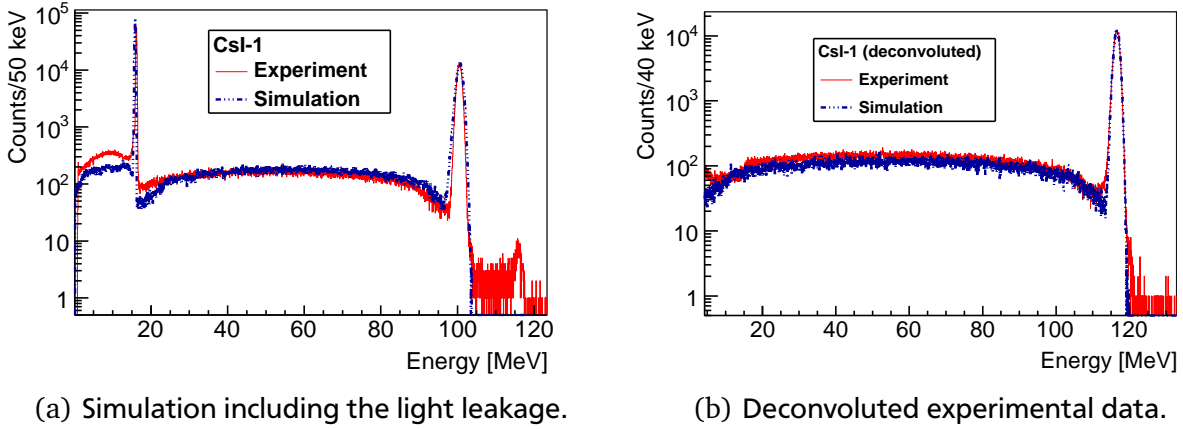


Figure A.5.: Comparison of simulation and experiment of the CsI energy spectrum. The simulation was done using the linear transformation of eq.(A.1) for each event. For the deconvolution of the experimental data the respective inverse transformation was applied.

This explains that the positive correlations (below 20 MeV) are mainly caused by light leakage between neighboring crystals. Such effect can also be seen in a bi-parametric spectrum (Fig. A.6) as lines with a positive slope. The line with the negative slope corresponds to the proton leakage from one crystal to another (anticorrelation).

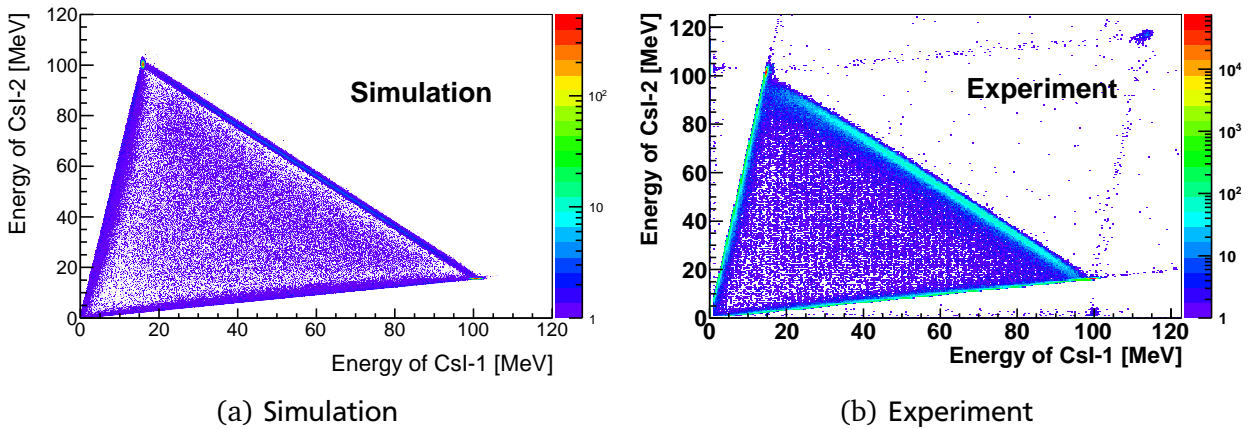


Figure A.6.: Energy spectra correlation of the two CsI crystals. The correlation effect, due to the light leakage, is seen as lines with positive slope. The anticorrelation (line with negative slope) shows the proton leakage.

The present linear transformation can also affect the energy resolution by a certain reduction factor, similar as observed in the experiment. A simple explanation of this effect is obtained by assuming the matrix variance

$$\mathbb{V} = \begin{pmatrix} \sigma^2 & \rho\sigma^2 \\ \rho\sigma^2 & \sigma^2 \end{pmatrix},$$

with σ^2 the variance of the total absorption peak and ρ the correlation factor between the two detectors due the proton leakage (close to -1). Then, it is possible to calculate the variance matrix after the transformation

$$\mathbb{V}' = \beta^T \mathbb{V} \beta,$$

where β is the matrix transformation of eq.(A.1). Thus, the new variance is given by

$$\sigma_{\text{trans.}}^2 = \sigma^2 \left((1 - \alpha)^2 + 2\rho\alpha(1 - \alpha) + \alpha^2 \right).$$

For instance, assuming $\rho = -0.9$, we get $\sigma_{\text{trans.}} \simeq 0.74\sigma$.

An immediate consequence from our simulation results is that the experimental correlations in the crystals are highly linear. Therefore, a similar procedure can be applied to perform the experimental data deconvolution. For that the inverse transformation of eq.(A.1) is needed

$$\begin{pmatrix} N_1 \\ N_2 \end{pmatrix} = \frac{1}{(1 - \alpha)^2 - \alpha^2} \begin{pmatrix} 1 - \alpha & -\alpha \\ -\alpha & 1 - \alpha \end{pmatrix} \begin{pmatrix} N'_1 \\ N'_2 \end{pmatrix},$$

which is applied for each event. Thus, as is shown in Fig. A.5(b), this procedure can be useful for the correction of light cross-talk in the experimental data if similar problems with double-photomultiplier occurred, as is shown in Fig. A.5(b).

A.0.2 DSSD interstrip signals

In order to perform a realistic simulation for the DSSD, we built the detector in two parts: p and n side. Each part is a single-sided strip detector, rotated by 90° relative to the other. The thickness of each segment was $142.5 \mu\text{m}$ ($285 \mu\text{m}$ total detector thickness) and an area of $(21 \times 21) \text{mm}^2$. At every detector hit (p or n side), two identical digits are created, and later assigned to the p(n)-side digit collection class. In this part, special care was taken at the boundary of these two geometries in order to not over count or miss the digits. In Fig. A.7(a) the DSSD geometry in the simulation is shown.

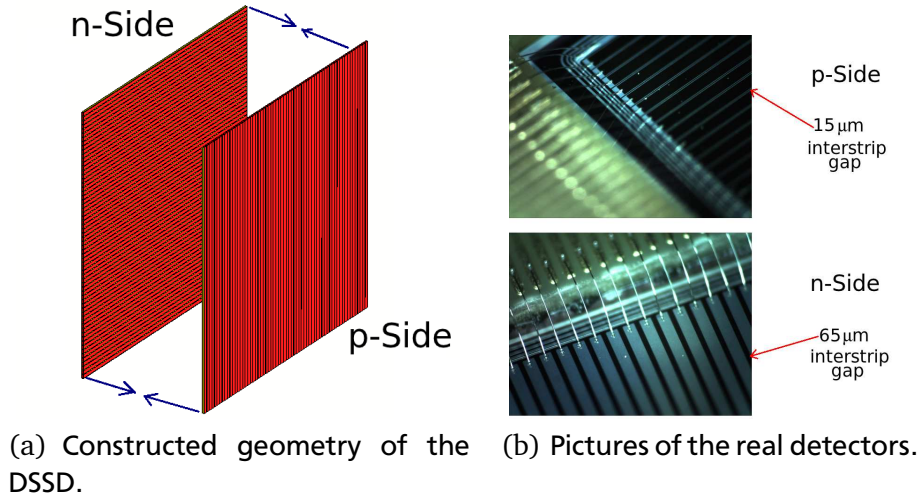


Figure A.7.: Simulated geometry for the DSSD detector. The detector was assumed as a junction of p- and n-side SSDs. On the right side pictures of the real detectors are presented.

Both parts were divided in 64 strips with an interstrip gap of $15 \mu\text{m}$ for the p-side and $65 \mu\text{m}$ for the n-Side. In Fig. A.7(b) pictures of the real detector are shown. Here, it is possible to observe the strip division and the interstrip gaps for each case.

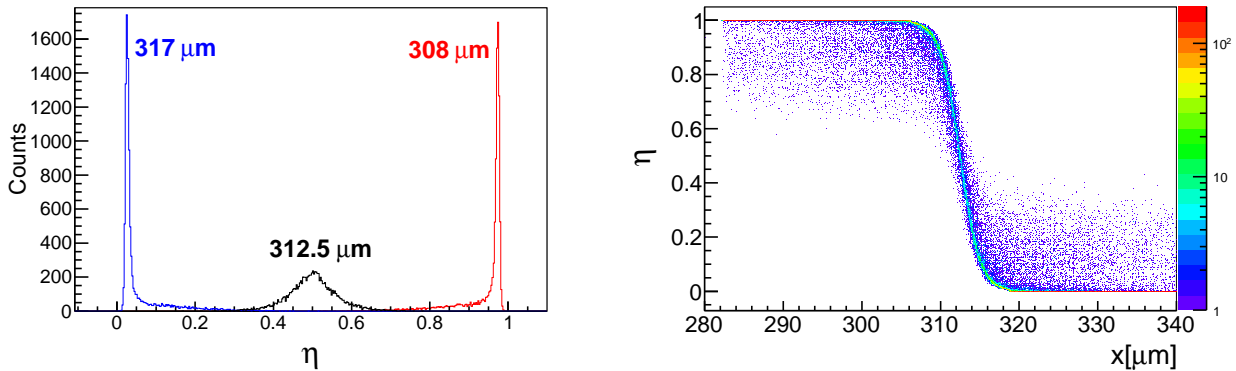
One of the aims of the present simulations is to study the charge partitioning due to the interstrip hits and its effect on the energy spectra. In the past years, a lot of effort was invested to understand this problem in experiments with multisegmented detectors [136, 137]. Also, complex theoretical models have been successfully applied to describe the charge-collection efficiency [138, 139]. Based on these works, a simple model was assumed for the simulation of charge-partitioning in interstrip hits. Let Q_0 be the total charge collected at a certain event. Then, if the particle hits in between two neighboring strips, the charge is divided in a left (Q_L) and a right (Q_R) part, i.e.

$$Q_{L(R)} = \frac{Q_0}{1 + \exp\left(\frac{x-x_m}{a}\right)} \quad \text{and} \quad Q_{R(L)} = Q_0 - Q_{L(R)}, \quad (\text{A.3})$$

where x_m is the center of the interstrip gap and a is related to the diffusion of the electron (hole) cloud, which can be assumed as 10% of the interstrip gap [138]. Under this consideration, there are no charge losses and the fraction of collected charge in one strip depends on its proximity to the hit. Since the same procedure is employed in the p and n sections, it is necessary to track the interacting particles inside the detector at every step. One way to validate this model is to perform a simulation by scanning the interstrip area with constant energy particles and, for example, extract the charge-collection efficiency for the left strip (analogous for the right part)

$$\eta = \frac{Q_L}{Q_L + Q_R}. \quad (\text{A.4})$$

In the present results, we focus on the interstrip gap between $305 \mu\text{m}$ and $320 \mu\text{m}$. In Fig. A.8(a) one can see the efficiency of the charge-collection at three different hit positions. The efficiency distributions are quite narrow at vicinity to the strip's edge, but are more extended at intermediate positions because of the large amount of charge shared in these regions.



(a) Charge collection efficiency for 3 hit positions.

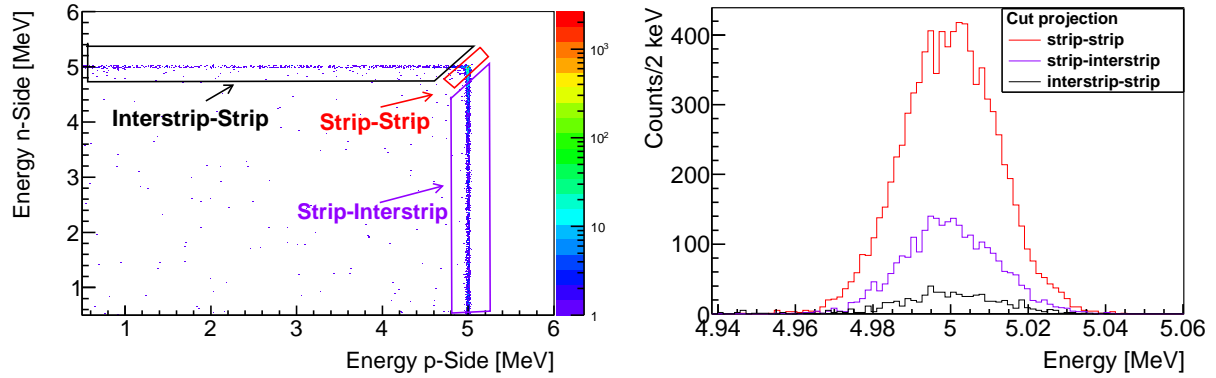
(b) Interstrip area illuminated with a plane source.

Figure A.8.: Interstrip simulation results. The edge of the left strip is $305 \mu\text{m}$ and $320 \mu\text{m}$ for the right strip. The interstrip area was scanned with constant energy particles.

These effects can also be seen when the interstrip gap is illuminated with a horizontal plane source (see Fig. A.8(b)). In the middle, the efficiency distribution has an extension up to 20%. Also, it is possible to see that the assumed shape in eq (A.3) is obtained.

Now, when the detector is totally illuminated we can study the correlations between p and n side. Fig. A.9 shows the simulated p-n side energy spectrum, from where we can identify the different interstrip events.

The horizontal line represents the hits on the p-side interstrip gap and on the n-side strip. Similarly, the vertical line shows the events from the n-side interstrip gap with strip hits on the p-side. When the



(a) Correlation spectrum of p - n sides.

(b) Energy projection for different interstrip conditions.

Figure A.9.: Energy spectra when the detector was totally illuminated with 5 MeV alpha particles.

respective energy projection is done, it is possible to extract the interaction probability in each case, which are: 71% for (p) Strip- (n) Strip, 22% for (p) strip- (n) interstrip, 6% for (p) interstrip- (n) strip and 1% for (p) interstrip- (n) interstrip. These results are in perfect agreement with the experimental data [140] and also with the expectations from the effective interaction areas.

Returning to the initial problem, where simulations without strip correlation were not able to describe the experimental results of the in-beam test (see Fig. A.2(b)), we employ the present simulations in order to understand the effect of the interstrip events on the energy spectra. Fig. A.10 shows the comparison of the energy spectrum of one of the strips with this new simulations. Now we can see the peaks are more extended especially towards low energy region, which is in much better agreement with the experimental peak shape.

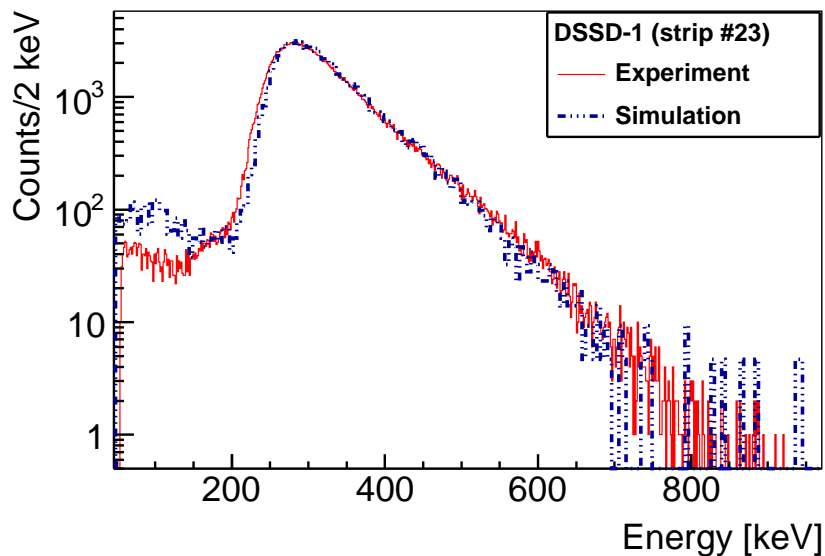


Figure A.10.: Comparison of a strip energy spectrum with the simulation. For this simulation the charge-partitioning in the interstrip events was taken into account.

The low energy part, as also seen in Fig. A.9(a), basically belongs to the interstrip events. In our model, this energy region is overestimated, and this could be a sign for charge losses in the detector. Another way to see the interstrip events in the demonstrator test is to check the p - n side correlation. Fig. A.11 shows the comparison of our simulations with the experiment. In both cases it is possible to see the counts out of diagonal that are from charge-partitioning in the interstrip hits. As also seen before, this contribution does not represent more than 30% of the total events, and this percentage could even decrease at very low energies due to the charge losses effect with low penetrating particles.

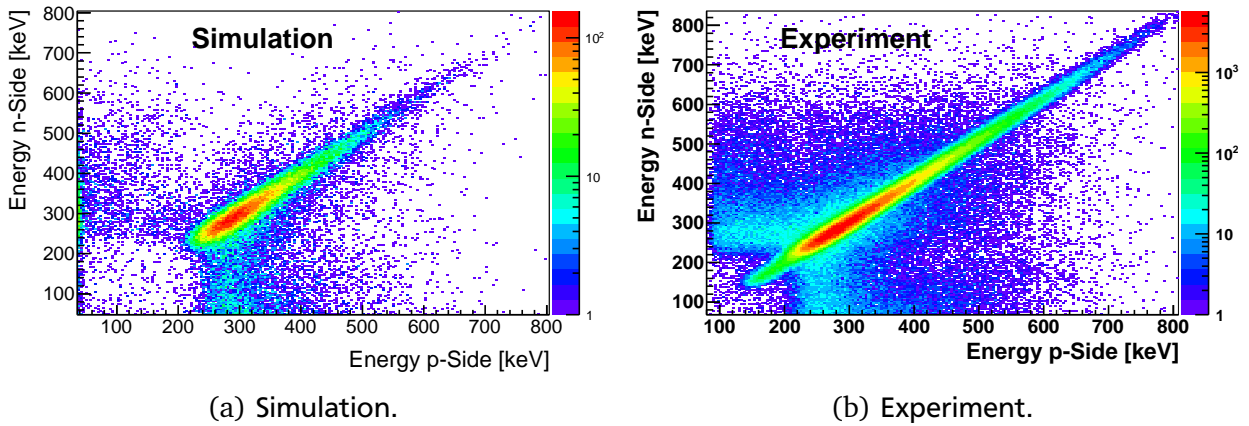


Figure A.11.: Comparison of simulation and experiment for the p - n side energy correction.

Future upgrades toward full EXL

B.1 Optional detector arrangement at the present vacuum chamber

In this chapter we will study some possible detector setups that would be implemented for experiments in the near future. With these new detector configurations, measurements with a higher angular coverage and better selectivity for reaction channels in interest would be achievable. The idea of the next step of the EXL project is to include as many detectors as possible in the current vacuum chamber (presented in Chapter 2) in an arrangement that enhances the particle tracking and the detection of inelastically scattered recoils at very forward angles in the center-of-mass system (c.m.s.). Specifically, one of the future goals will be to investigate the giant resonances with radioactive stored beams, like for example ^{56}Ni . For that reason it would be interesting to include telescope systems in order to separate the products from distinct reaction channels, particularly at low energy detection range. Fig. B.1 shows an optional design that comprises eight DSSDs and two Si(Li) detectors.

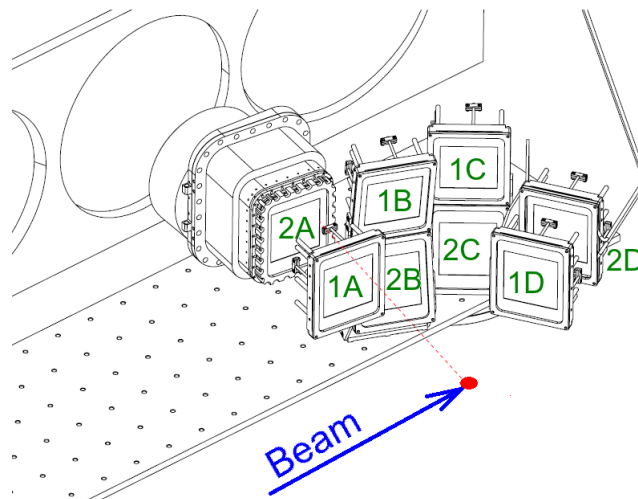


Figure B.1.: Schematic illustration of an optional detector setup for the next experiments of the EXL project. The setup is divided in four zones: A, B, C and D. In total eight DSSD will be mounted in the UHV and two Si(Li) detectors inside of a pocket. (Technical design by M. Lindemulder, KVI [34])

As can be noticed with the detector labeling, the system is divided in four sections: A, B, C and D. The section A is centered at a polar angle of 80.5° , comprising an optional DSSD in the front part of a pocket which contains a DSSD and two Si(Li) detectors behind, the one employed in the experiment E105. For

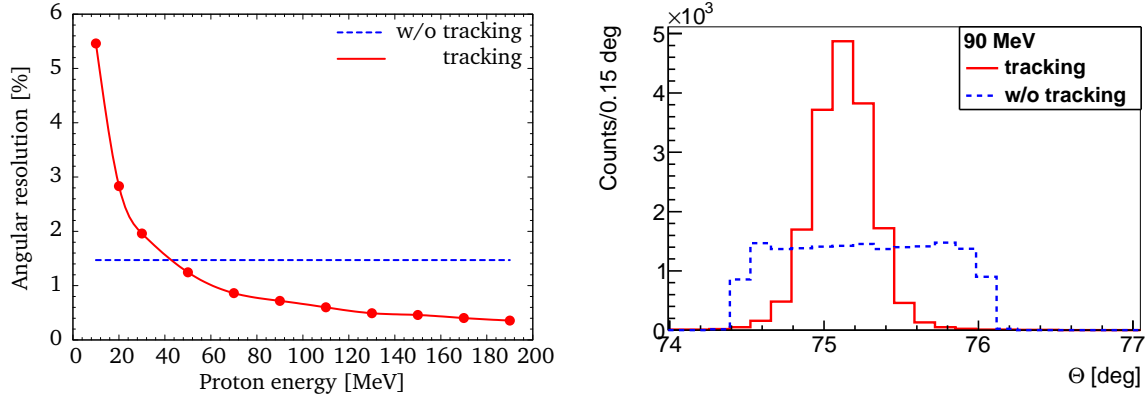
sections B and C, 1.5 mm thick DSSDs are planned to be used covering the polar angles from 70° to 43° , but installed symmetrically with respect the azimuth angle $\phi = 0^\circ$. The section D, centered at the angle $\theta = 28.5^\circ$, is a telescope composed by a thin DSSD in the front and a thick DSSD behind. A more detail information about this proposed detector setup can be found in Table B.1.

Detector ID	Thickness [mm]	Polar angle (θ)	Azimuthal angle (ϕ)	Distance [mm]
DSSD-1A	0.285	80.5°	0°	235
DSSD-2A	0.285	80.5°	0°	360
Si(Li)-1A	6.5	80.5°	0°	419
Si(Li)-2A	6.5	80.5°	0°	444
DSSD-1B	1.5	65.0°	$+11^\circ$	300
DSSD-2B	1.5	65.0°	-11°	300
DSSD-1C	1.5	48.0°	$+11^\circ$	355
DSSD-2C	1.5	48.0°	-11°	355
DSSD-1D	0.285	28.5°	0°	220
DSSD-2D	1.5	28.5°	0°	320

Table B.1.: Some specifications of the detector setup presented in Fig. B.1. The angles are measured with respect the beam direction and the distances are determined from the center of the gas target.

One of the main features of this new experimental arrangement is the possibility to track the high energy recoils using telescope systems composed by multiple DSSDs. For instance, section A provides the opportunity to record the trajectories of the recoils coming from elastic scattering, excitation of low lying states and some products from transfer reactions that can be observed with high kinetic energies in this angular region. In principle, the direction of incidence of these particles on the front DSSD defines the laboratory angles of the reaction. However, the resolution is constrained by the extended target distribution and the beam diameter. An alternative method for deducing the recoil angles is to use a couple of multisegmented detectors, mounted sequentially, with a sufficient separation between them to resolve the angular coverage per strip, like the telescope of section A. Thus, the angles can be directly deduced from the recoil trajectory, which is obtained from coincidences of the diverse strips (or pixels) of the two DSSDs. In order to evaluate this method, proton recoils impinging on section A were simulated at different kinetic energies above the punching through threshold for protons in the DSSD-1A. In Fig. B.2, a comparison of the polar angle deduced from the recoil particle tracking and the one obtained from the DSSD-1A acceptance is presented. In particular, this tracking method is not very efficient at energies around the punching-through threshold of the two DSSDs (~ 14 MeV) because of the importance of the angular straggling in this energy range. For energies larger than 40 MeV, clearly, the most advantageous way to calculate the angles is from the particle tracking. As an example, Fig. B.2(b) shows the significant improvement for the angular resolution already at 90 MeV.

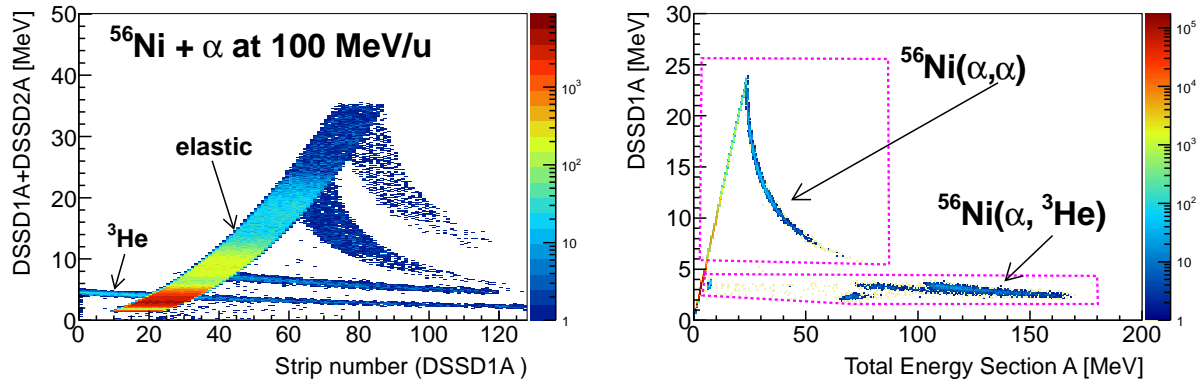
As previously mentioned, one of the principal applications for this dedicated detector setup is to investigate the isoscalar giant resonances with the stored radioactive beam ^{56}Ni by measuring the α -particle scattering. As expected in this type of inverse kinematics experiments, the elastically scattered particles are detected mainly in the detector sections A and B. Similarly, due to the kinematics, some stripping reactions can also be observed in these detectors. At 100 MeV/u, with a luminosity in the order of $10^{27} \text{ cm}^{-2}\text{s}^{-1}$, reactions like $^{56}\text{Ni}(\alpha, ^3\text{He})^{57}\text{Ni}$ could be measured in laboratory angles close to 90° , because of their significant probability at angles below 30° in the center of mass system. In Fig. B.3, simulation results assuming the reaction channels mentioned above are presented. Fig. B.3(a) shows the energy deposited in the two DSSDs of section A, as a function of the different vertical strips from the DSSD located closer to the interaction zone. Similar to the results of Section 4.2, the strip number is proportional to the polar angle due to the large separation of these detectors from the target position,



(a) Angular resolution at different recoil energies. (b) Sample of angle projection for protons at 90 MeV.

Figure B.2.: Polar angle deduced by tracking the recoil particle. The method is more efficient at high energies.

what in turn provides a clear visualization of the recoil kinematics. The intensity of the elastic reaction channel is quite significant, even at given angles the scattered recoils have energies large enough to punch through both DSSDs. On the other hand, the detection of the ${}^3\text{He}$ particles produced in the transfer reaction is predicted to have an intensity of almost three orders of magnitude lower than the elastic scattering. The detection of these particles is mainly observed at energies below 10 MeV, because in such angles their kinetic energy is quite significant and only energy loss is registered in the DSSDs. The two parallel kinematic lines reflect the region where the detectors are geometrically overlapping.



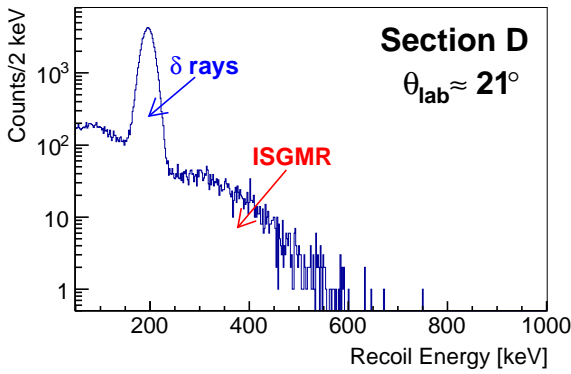
(a) Deposited energy in the DSSDs of section A vs. the vertical strip number of the frontal DSSD. (b) Telescope energy spectrum using the DSSD-1A against total energy detected in section A.

Figure B.3.: Simulation results for elastic scattering of ${}^{56}\text{Ni} + \alpha$ and the pick-up reaction ${}^{56}\text{Ni} + \alpha \rightarrow {}^3\text{He} + {}^{57}\text{Ni}$ at 100 MeV/u.

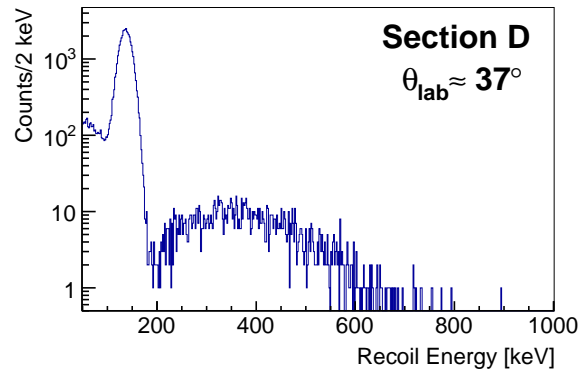
A more clear separation of the reaction channels can be done using the detector system as a telescope ($\Delta E-E_T$), where the signal of the DSSD-1A is employed as a ΔE and the other detectors (including the two Si(Li)s) for the total energy deposited, as is shown in Fig. B.3(b). Such configuration is quite advantageous for performing a separation between the events involving distinct recoil species and, especially, by their kinetic energy. In the upper part of this spectrum can be observed events produced from the elastic scattering, starting from a well defined growing part that represents the particles stopped in the

DSSD-1A, and followed by a decreasing region that exhibit the energy loss in this detector. Also, the ^3He residues are distinguishable at the bottom part of this spectrum, with total deposited energies larger than 100 MeV. This means, in order to identify this reaction channel a combination of several detectors is required due to the high energies of the recoils.

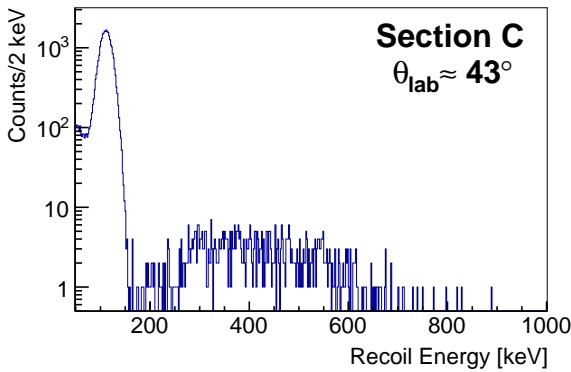
Simultaneously, in the detector sections C and D, which are located at more forward angles in the c.m.s., inelastically scattered recoils can be measured. As seen in Chapter 6, one of the main experimental problems for the giant resonances identification was the presence of δ -rays. In the present simulations we can still take into account this reaction channel in order to investigate the separability with this new detector configuration. Moreover, the position of the detectors in section D would permit measurements of inelastic scattering below $\theta_{\text{cm}} = 1^\circ$, while for section C in the range $1^\circ < \theta_{\text{cm}} < 2^\circ$. For this simulation, the Gaussian parametrization of the Ref.[116] was employed to describe the energy distribution of ISGMR. Also, the respective angular cross section was included in the event generator to have more realist results. In Fig. B.4, simulation results assuming only electron elastic scattering and the ISGMR excitation are presented. Fig. B.4(a) and Fig. B.4(b) are energy spectra samples from the edges of the DSSD-1D detector, where laboratory angles from 21° to 37° are covered. Similarly, Fig. B.4(c) and Fig. B.4(d) are energy spectra from the DSSD-1C at laboratory angles of 43° and 53° , respectively.



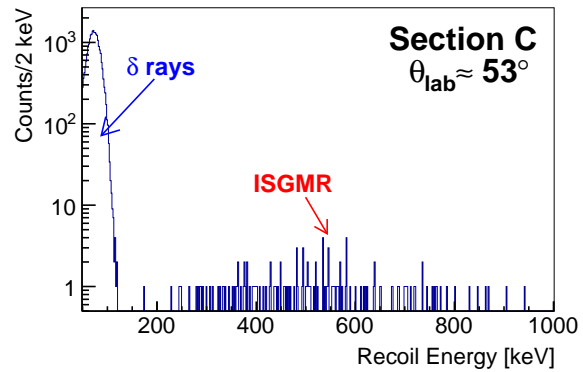
(a) The first strip of DSSD-1D at $\theta_{\text{lab}} \approx 21^\circ$.



(b) The last strip of DSSD-1D at $\theta_{\text{lab}} \approx 37^\circ$.



(c) The first strip of DSSD-1C at $\theta_{\text{lab}} \approx 43^\circ$



(d) The last strip of DSSD-1C at $\theta_{\text{lab}} \approx 53^\circ$

Figure B.4.: Simulated energy spectra for sections C and D assuming two reaction channels: δ -rays production and excitation of ISGMR. The sequence shows the changes in peak positions and shape for different polar angles in this part of the detector setup.

For the most forward strip (Fig. B.4(a)), one can note the important contribution of the resonance below 500 keV, but here the detection of the δ -rays affects the full separation of this peak since energies about 200 keV. However, in laboratory angles larger than 30° the position of the δ -ray peak is shifted to lower energies, what in turn enhances the identification of the ISGMR component. In the detector section C the

separation is still better, but in contrast, the ISGMR intensity is decreased due to the low cross section in this range. From the present results we learn that measurements of isoscalar giant resonances are feasible with the planned detector setup, as long as the signals of the δ -rays are vetoed or well identified during the data acquisition. Also, the use of telescope systems may be important in order to remove the contribution from particles with high kinetic energies.

B.2 Implementation of the full EXL recoil-detector setup

All experimental results and simulations which have been presented along this work are devoted to the investigation of detector response under diverse conditions and their applications towards the final version of the recoil-detector setup of EXL. As it was seen in Chapter 1, the full EXL setup will feature hundreds of multisegmented silicon detectors (ESPA, EXL Silicon Particle Array) covering a large solid angle around an internal gas-jet target, and surrounding this, a complex arrangement of scintillator crystals (EGPA, EXL Gamma and Particle Array) will operate as a calorimeter [8]. For this work, the complete geometry of this recoil-detector setup has been implemented in our simulations in order to explore its performance in distinct experiments that might be performed in the future with the full detector configuration. The simulated geometry is based on technical designs presented in previous works [8, 141], but with slight differences such as the dimensions of some type of detectors and their distances from the interaction center. In total, 735 independent multisegmented-volumes divided in 6 sections were included for the reconstruction of the silicon array (ESPA): A, B, C, D, E and F. Each of these sections are composed of manifold detector layers, which can be employed for particle tracking and separation, as it was studied in the previous section. The polar angle coverage is rather extended, ranging forward angles from 10° to backward regions up to 170° . The sections D and F have 360° coverage in azimuth angles, while the other sections cover lower ranges due to limitation imposed by the mechanical structure of the system. An outline of the distances, dimensions and number of detectors implemented in each of these sections is presented in Table B.2.

Section	Layer ID	θ_{lab} [deg]	Area [mm ²]	Thickness [mm]	Distance [mm]	Number of det.
A	0	89-80	90 × 90	0.3	580	22
	1		90 × 90	6.5	600	22
B	0	80-75	60 × 90	0.3	450	22
	1		60 × 90	6.5	468	22
	2		60 × 90	6.5	525	22
	3		60 × 90	6.5	560	22
C	0	75-45	90 × 90	0.1	450	88
	1		90 × 90	0.3	580	88
D	0	45-10	90 × 90	0.1	450	56
	1		90 × 90	0.3	550	56
	2		90 × 90	6.5	560	56
E	0	120-91	90 × 90	0.3	580	66
	1		90 × 90	6.5	600	66
F	0	170-120	50 × 50	0.3	250	64
	1		50 × 50	6.5	260	64

Table B.2.: Specifications of the recoil silicon array (ESPA). Each section is divided in different layers distributed along its angular range. Distances and angles are given with respect to the center of the interaction point.

As can be noticed, the most forward angles (respect to the beam direction) are covered by the regions D and C, also the detection near 90° would take place in sections B and A, and at rear angles the regions

E and F would complete the polar angle coverage. Fig. B.5 shows a schematic illustration of the ESPA geometry implemented in this work. Fig. B.5(a) shows a horizontal cut of the simulated geometry seen from the top and Fig. B.5(b) is a vertical cut in a rear angle perspective.

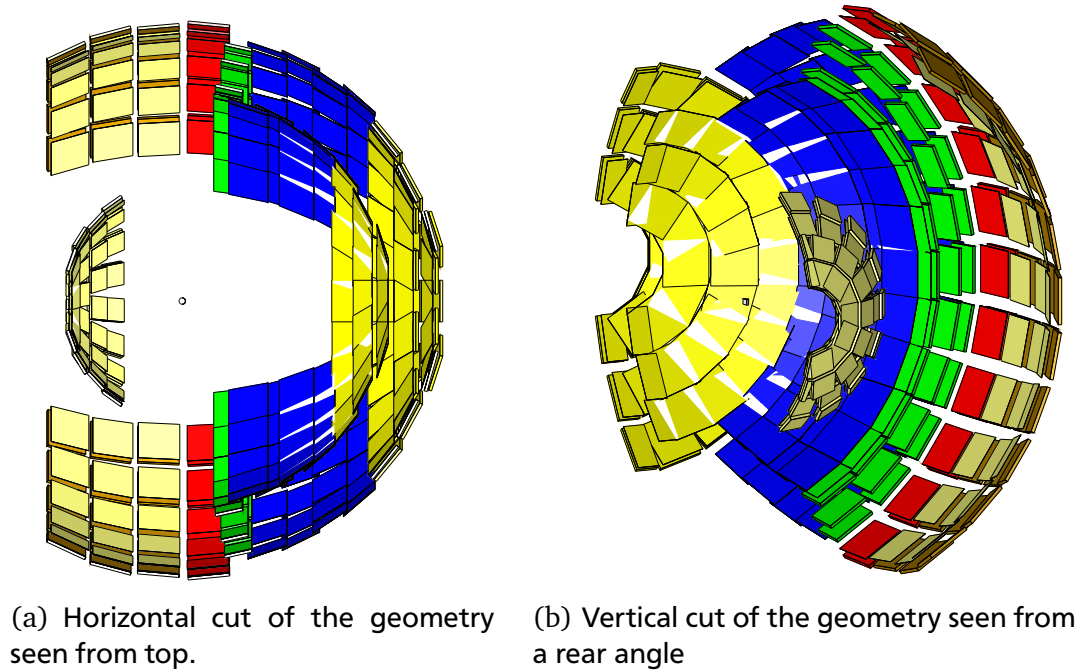


Figure B.5.: Schematic illustration of the implemented silicon array ESPA. Each section of the system can be distinguished by a different color tone.

Each detector zone can be distinguished in the illustrations by different color tones used to fill the detector volumes. In these illustrations a significant amount of detector layers at some angular regions which can provide a precise high energy particle detection. As the detectors foreseen to be used in section F have a smaller size, this detector zone has been installed closer to the internal gas-jet target in order to full fit the solid angle acceptance at backward direction.

Moreover, the complex EGPA configuration which will comprise about 2000 CsI crystals arranged in a spherical shell shape enveloping the ESPA. Since the detailed implementation of the EGPA is beyond the objectives of this work, this arrangement was constructed in the present simulation as a single macroscopic volume with the same angular coverage and dimensions that are expected for the final geometry of this system [8]. In Fig. B.6 we can observe the entire ESPA structure from a frontal perspective and an external shell of CsI representing the EGPA. A natural way to evaluate this dedicated geometry is to simulate some possible nuclear reaction experiments with this system, e.g., elastic scattering at low momentum transfer, isoscalar giant resonances excitation, transfer reactions or quasi-free scattering. Below we will study some specific cases of nuclear reaction experiments with this setup.

B.2.1 Elastic Scattering

The elastic scattering of light ions (like p , d , α , etc.) at intermediate energies is a standard tool for extracting nuclear matter distributions and radial shapes of nuclei. In particular, the EXL recoil-detector setup gives access to complete measurements at low momentum transfer from where skin or halo structures of radioactive ion beams can be investigated. For instance, unstable nuclei like ^{11}Be (neutron halo) or ^{132}Sn (doubly magic) could be studied in the future by the EXL project. In the following simulations the reactions $^{11}\text{Be}(p, p)$ and $^{132}\text{Sn}(\alpha, \alpha)$, at 400 MeV/u energy beam are considered, in order to recon-

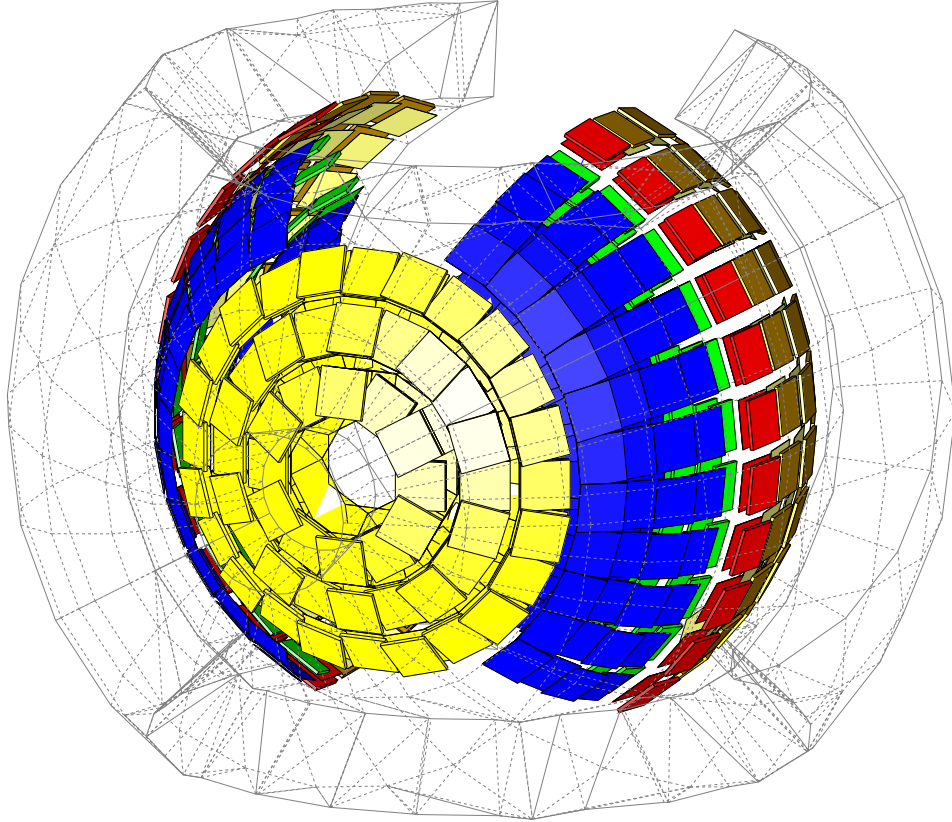


Figure B.6.: Schematic illustration of the complete ESPA and EGPA from a forward angle view. The internal ESPA is shown in color and the EGPA is the outer transparent volume.

struct the detection of such reaction channels from each of the individual detectors of the system. In Fig. B.7(a), one can see the total events built-up from the reaction $^{11}\text{Be} + p$.

The contribution from each detector-strip corresponding to sections A and B is presented in this spectrum, where the respective elastic kinematic-plot can be identified up to an energy of 60 MeV. The vertical dashed line represents the angular boundary between these two detector sections. In the case of elastic scattering with the ^{132}Sn beam (see Fig. B.7(b)), the α recoils are produced at higher kinetic energies and the reaction angles (in c.m.s.) are condensed close to 90° . For this reason the total amount of detected events in section B is reduced, since the respective cross section drops significantly at large θ_{cm} .

B.2.2 Excitation of Isoscalar Giant Resonances

One of the major advantages of the full EXL setup is the option to measure scattered particles at very forward angles in the center of mass system. For light-ion inelastic scattering at small θ_{cm} , it is possible to study collective properties of nuclei through the excitation of giant resonances. As it was previously mentioned, the α inelastic scattering enhances the excitation of isoscalar giant resonances in the nucleus. For example, in a future experiment with an unstable stored ^{132}Sn beam, the ISGMR or the ISGQR can be

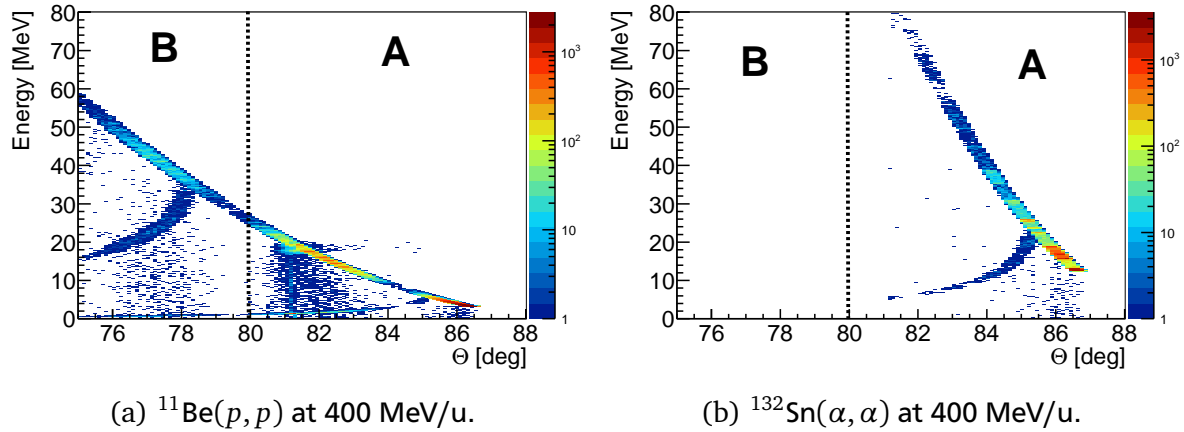
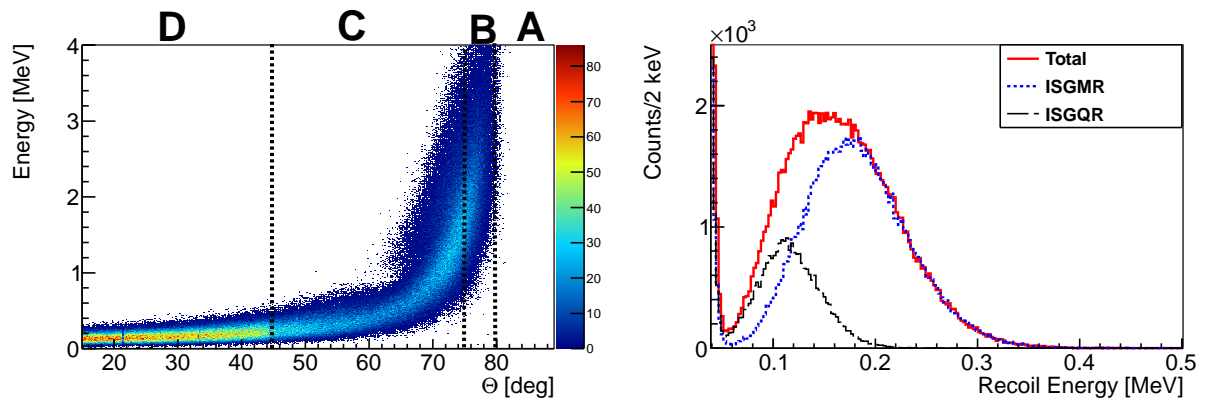


Figure B.7.: Simulation results for elastic scattering with the complete recoil detector system of EXL. The vertical dashed lines represent the separation of the detector section A and B that are described in Table B.2.

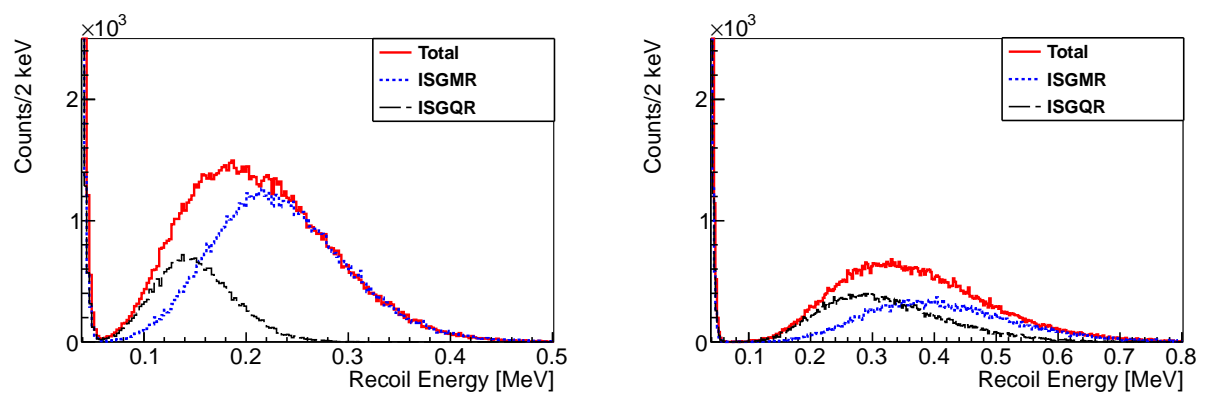
investigated with a good accuracy by employing this EXL detector setup. In order to perform a realistic simulation for these resonances, the differential cross section of these multipolarities was calculated with the program CHUCK3 [59] and included as an input to the event generator of the simulation. Also, the energy distributions of these resonances was extracted from a RPA calculations with the code SKYRME_RPA [110]. In Fig. B.8 results of the simulation are shown, where the scattering angle θ_{cm} ranges from 0° to 5° . As can be noticed in Fig. B.8(a), the kinematic plot is reconstructed from the energy deposited in all detectors placed in laboratory angles from 10° to 90° . The detector zone D is more favorable for the detection of giant resonances due to the inverse kinematics, but in some cases this component could be even below the noise threshold which was assumed to be about 60 keV for the present simulations. For sections C and D, the detected recoils have higher kinetic energies, but with extended distributions in the energy axis for all individual detectors in such range. In principle, this could affect the full identification of the resonances in this angular region since its cross section is small and also because there may be other reaction channels with a higher intensity. Using only detectors mounted in a given polar angle (ring), the energy profile of the resonance peak is obtained. In Figs. B.8(b), B.8(c) and B.8(d) three samples at distinct angles are shown. For the projection of the ring at 27.15° , the ISGMR component is dominant due to the small angles covered in c.m.s.. However, the ISGQR peak in these detectors is very close to the noise threshold. The ISGQR excitation becomes more important at rear rings, but its energy distribution becomes more extended and less intense.

B.2.3 Transfer Reactions

Nuclear reactions which involve transfer of one or few nucleons provide information on the single-particle configurations of neutrons and protons in nuclei. Also, occupation numbers and spectroscopic factors can be deduced from this type of experiments, that are particularly important for understanding the nucleosynthesis pathways. For instance, pick-up reactions in vicinity of ^{56}Fe , like $^{55}\text{Co}(p, d)$, can provide information about the final phase in the life of stars (presupernova evolution). With stripping reactions, as $^{66}\text{Ni}(d, p)$, the low energy astrophysical S-factors can be directly obtained. So, the reactions mentioned may be good examples of nucleon-transfer experiments feasible with the future EXL setup. In the present case, the reactions $^{55}\text{Co}(p, d)$ and $^{66}\text{Ni}(d, p)$ at 50 MeV/u were simulated. Results from the pick-up reaction are shown in Figs. B.9(a) and B.9(c). The recoil detection in this reaction channel is enhanced at forward angles in the laboratory system where section D has a large coverage. Therefore,



(a) Reconstructed kinematic plot for the detector sections at forward angles. (b) Energy projection of the ring at 27.15°.

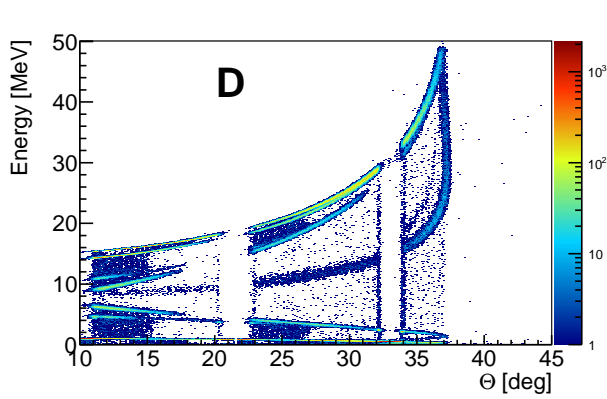


(c) Energy projection of the ring at 38.55°. (d) Energy projection of the ring at 56.21°.

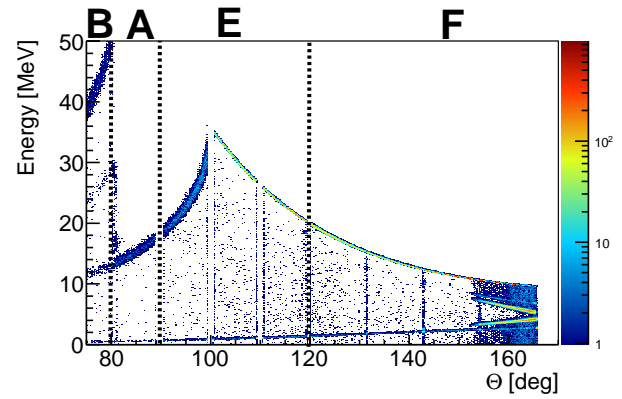
Figure B.8.: Simulation results of ISGMR and ISGQR excitations in ^{132}Sn with the full recoil-detector system.

reactions which occur in small θ_{cm} are measured by detecting deuterons at angles close to 10° (in lab.) with energies smaller than 20 MeV.

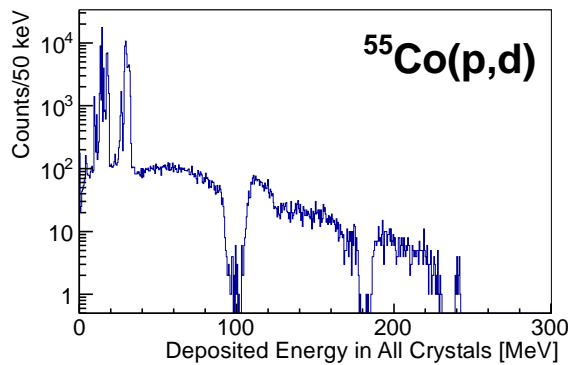
The maximum scattered angle in the laboratory system is reached at 37° , which corresponds to θ_{cm} around 52° . Also, the maximum deposited energy of these recoils in the silicon array (ESPA) is about 50 MeV. Deuterons with higher kinetic energies are able to escape from the silicon array, but are totally stopped in the external CsI setup (EGPA). Fig. B.9(c) shows the total deposited energy spectrum in the EGPA for the present reaction. As can be noticed, very intense peaks at low energy range from γ -rays and/or neutrons are also measured. In principle, particle coincidences between ESPA and EGPA detector systems would permit a full kinematic identification of the recoils in an extended range of excitation energies. On the other hand, stripping reactions in inverse kinematics are characterized by producing recoils (with small θ_{cm}) in backward directions in the laboratory system. In this case, the detector zones F and E are the most relevant for such transfer reactions, as can be seen in Fig. B.9(b). Also, detection of recoils in more forward regions (sections A and B) is still possible given that the respective angles in c.m.s are just about 50° . It is important to note that the maximum energy deposited by the protons in section F is around 36 MeV, however relatively clean measurements would be possible due to the kinematic selectivity for most of the allowed nuclear reactions. Similarly as seen before, Fig. B.9(d) shows the total deposited energy in the EGPA calorimeter where most of the faster recoils and emitted γ -rays are absorbed.



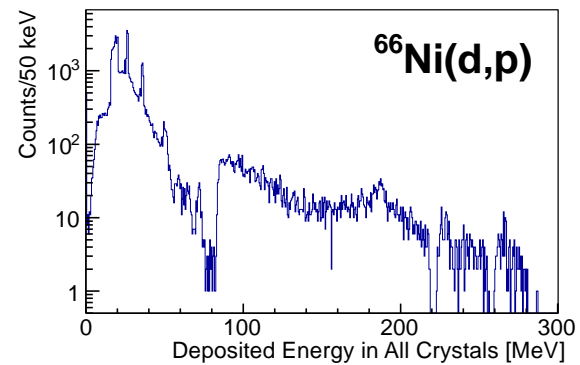
(a) Reconstructed kinematic plot with the ESPA for the reaction $^{55}\text{Co}(p, d)$.



(b) Reconstructed kinematic plot with the ESPA for the reaction $^{66}\text{Ni}(d, p)$.



(c) Total energy deposited in the EGPA for the reaction $^{55}\text{Co}(p, d)$.



(d) Total energy deposited in the EGPA for the reaction $^{66}\text{Ni}(d, p)$.

Figure B.9.: Simulation results of transfer reactions with the complete recoil detector system of EXL. The figures on the left side correspond to the pick-up-reaction results. On the right side, simulation results of a stripping reaction are shown.

B.2.4 Quasi-free Scattering

Quasi-free scattering is the most direct and powerful way to investigate the single-particle properties such as separation energies and the momentum distribution of nucleons inside of the nucleus. Particularly, the structure of light and medium mass nuclei near the neutron closures can be studied using $(p, 2p)$ and (p, pn) reactions. In the future, the full version of the EXL setup will also include a dedicated system for neutron detection which would allow to perform proton and knockout neutron coincidences. Nevertheless, the most appropriate way to test the performance of the simulated EXL geometry with this type of reaction is by measuring two charged particles in coincidence (like $(p, 2p)$). For the present simulation, the reaction $^{14}\text{O}(p, 2p)$ at 400 MeV/u was produced by using a three-body particle kinematics generator routine. Then, two protons are produced at the same event with a certain orientation and energy given by the nucleon-momentum inside the nucleus and the energy conservation. The results presented in Fig. B.10(a) correspond to the characteristic polar-angle correlation of the two light-particles in the quasi-free scattering. The average polar angular separation (in the laboratory system) of these two protons is close to 80° . The detection of this reaction channel is exclusively done in sections D and C. Another feature of the quasi-free scattering, that is possible to observe in the present simulations, is the azimuth-angle correlation (Fig. B.10(b)). Two parallel lines show that these protons are produced in

opposite directions with $\Delta\phi \approx 180^\circ$. This result also demonstrates the large azimuth-angle acceptance of this full EXL setup, which is a key requirement for the realization of such experiments.

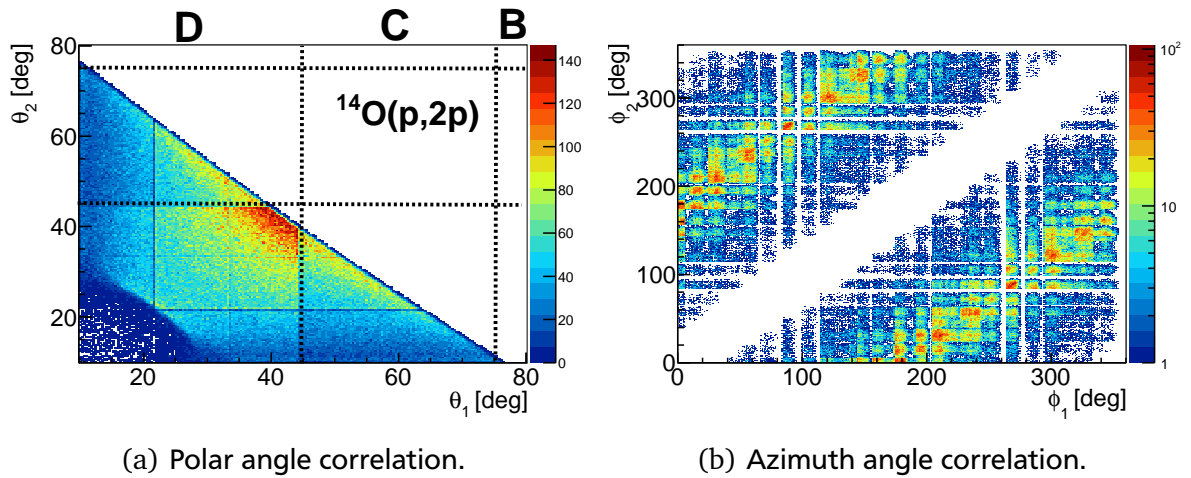


Figure B.10.: Simulated angle correlation for the reaction $^{14}\text{O}(p, 2p)$, at 400 MeV/u, using the complete recoil detector system of EXL. The subscript (1 or 2) in the angles denote each proton in the output channel.



Continuum Discretized Coupled Channel

Weakly bound nuclei have small separation energies and thus, break-up easily. The proximity of the ground state to separation threshold also means that the breakup states of such nuclei (i.e. its continuum) influence all other reactions that can take place [142]. The breakup is an inelastic process which can be induced by Coulomb or nuclear interaction. When the target-projectile interaction is pure Coulomb, this reaction channel is called *Coulomb breakup*. A natural way to describe this process is by coupling the continuum states (non-bound) of the weakly-bound particle. Thus, the problem can be reduced to solving the scattering equations in the coupled-channel formalism [67–69]. In principle, this procedure might be extended to describe the coupling with the continuum, however there are normalization problems related to the wavefunctions of the continuum excited states. Whereas the wavefunction of a bound state is normalizable and decays exponentially at large distances, the corresponding wavefunction of a non-bound state has significant oscillations asymptotically and its norm does not exist [143], as suggested in Fig. C.1.

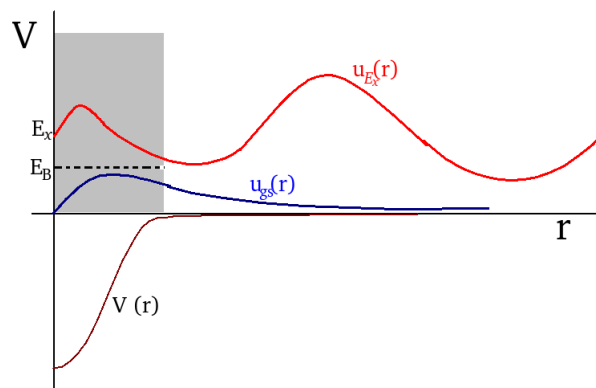


Figure C.1.: Schematic representation of the wavefunctions of a bound state and a continuum one. The wavefunction of the bound state is normalizable, while the corresponding wavefunction of a continuum excited state have large oscillations asymptotically. (Adapted from Ref. [143])

In order to overcome this problem, a discretized representation of the continuum is employed. This method permits a suitable description of a set of normalizable wavefunctions from the continuum. When such discrete states are included into a coupled channel calculation, the formalism is called *Continuum Discretized Coupled Channel (CDCC)* [142, 144]. The discretization can be done by divid-

ing the continuum range in energy bins, of width Γ , in order to represent an average wavefunction per bin. Hence, the resulting bin states are square integrable, and are defined as [145]

$$\psi_\ell(r) = N \int_{E_r - \Gamma/2}^{E_r + \Gamma/2} \phi_E(r) f(E) dE, \quad (\text{C.1})$$

with

$$\int_0^R |\psi_\ell(r)|^2 dr = 1 \quad \text{and} \quad N^2 = \frac{1}{\int |f(E)|^2 dE}. \quad (\text{C.2})$$

The $\phi_E(r)$ are eigenfunctions with a potential which is energy-independent, and $f(E)$ is a weight function that is chosen to guarantee the asymptotic normalization of the wavefunction ($R \rightarrow \infty$).

In the CDCC calculations, the target-projectile interaction is described with the cluster model. The weakly bound nucleus is then considered as cluster composed by a core (c) and a valence (v) particle. In the same manner, the target-projectile potential can be splitted into a core-target and valence-target interactions which are projected over the weakly-bound particle states

$$V_{\alpha, \alpha'} = \langle \alpha | V_{c,A} + V_{v,A} | \alpha' \rangle. \quad (\text{C.3})$$

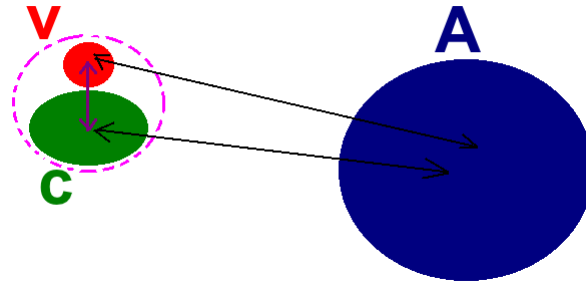


Figure C.2.: Representation of the cluster interaction composed by a three body system: core, valence and a target (or projectile) A which is a tightly bound particle. In the CDCC calculations the problem can be described by the potentials: c - A , v - A and c - v (binding energy).

Bibliography

- [1] I. Brissaud, , et al. Détermination du rayon de la distribution de neutrons de certains noyaux par l'étude de la diffusion élastique de particules alpha de 166 MeV. *Nucl. Phys. A*, 191(1):145–165, 1972.
- [2] G.D. Alkharov et al. Neutron matter densities in the even Ni isotopes. *Phys. Lett. B*, 67(4):402–404, 1977.
- [3] A.M. Bernstein et al. Neutron and proton transition matrix elements and inelastic hadron scattering. *Phys. Lett. B*, 103(4-5):255–258, 1981.
- [4] B.K. Nayak et al. 'bi-modal' isoscalar giant dipole strength in 58Ni. *Phys. Lett. B*, 637(1-2):43–47, 2006.
- [5] M. N. Harakeh and A. van der Woude. *Giant Resonances: Fundamental High-frequency Modes of Nuclear Excitation*. Oxford science publications. Oxford University Press, 2001.
- [6] W.R. Falk et al. Energy levels of 18Ne from the 20Ne(p, t)18Ne reaction. *Nucl. Phys. A*, 157(1):241–262, 1970.
- [7] J. P. Schiffer et al. Study of the (d, p) reaction in the 1p shell. *Phys. Rev.*, 164:1274–1284, Dec 1967.
- [8] H. H. Gutbrod et al. *FAIR Baseline Technical Report*, ISBN:3-9811298-0-6, 4(4.9), (2006).
- [9] B. Streicher et al. Application of a double-sided silicon-strip detector as a differential pumping barrier for NESR experiments at FAIR. *Nucl. Instr. and Meth. A*, 654:604, (2011).
- [10] J. Klabunde. The high charge state injector for GSI. *Linear Accelerator Conference, Ottawa, Canada*, page 570, 1992.
- [11] https://www.gsi.de/en/work/fairgsi/linac_and_operations/linac.htm.
- [12] W. B. Bayer et al. Heavy-ion-beam emittance measurements at the GSI UNILAC. *International LINAC, Knoxville, Tennessee USA*, page 177, 2006.
- [13] R. Hollinger, , et al. *Ion Source Operation at the GSI Accelerator Facility*, volume 2013-1 of *GSI Report*, pages 257– p. GSI Helmholtzzentrum für Schwerionenforschung, Darmstadt, 2013.
- [14] UNILAC/SIS accelerator logbook
. https://web-docs.gsi.de/~wolle/EB_at_GSI/GSI/ACCELERATOR/accelerator.html.
- [15] P. Kienle. The SIS-ESR project of GSI. *GSI Scientific Report*, May 1985.

-
- [16] <http://bel.gsi.de/online/log/2012/index.html>.
- [17] B. Schlitt. *Schottky Mass Spectrometry at the Heavy Ion Storage Ring ESR*. PhD thesis, Ruprecht-Karls-Universität Heidelberg, 1997.
- [18] H.F. Beyer et al. Crystal optics for hard-X-ray spectroscopy of highly charged ions. *Spectrochimica Acta Part B: Atomic Spectroscopy*, 64(8):736 – 743, 2009.
- [19] A. Gumberidze. *Experimental Studies of the Ground State QED Corrections in H- like and He-like Uranium*. PhD thesis, Johann Wolfgang Goethe-Universität Frankfurt, 2003.
- [20] M. Steck. Storage Rings Lecture, Helmholtz-Rosatom School, 2011. Unpublished.
- [21] H. Reeg and N. Schneider. Current transformers for GSIs keV/u to GeV/u ion beams - an overview. *5th European Workshop on Diagnostics and Beam Instrumentation, Grenoble, France*, page 120, 2001.
- [22] K. Unser. Beam current transformer with D.C. to 200 MHz range. *Nuclear Science, IEEE Transactions on*, 16(3):934–938, June 1969.
- [23] M. von Schmid et al. First EXL experiment with stored radioactive beam: Proton scattering on ^{56}Ni . *EPJ Web of Conferences*, 66:03093, (2014).
- [24] Th. Stöhlker, , et al. Charge-exchange cross sections and beam lifetimes for stored and decelerated bare uranium ions. *Phys. Rev. A*, 58:2043–2050, Sep 1998.
- [25] Th. Stöhlker, , et al. Radiative electron capture studied in relativistic heavy-ion–atom collisions. *Phys. Rev. A*, 51:2098–2111, Mar 1995.
- [26] A. Gruber et al. Internal gas-jet target for the ESR at GSI. *Nucl. Instrum. and Methods A*, 282(1):87 – 93, 1989.
- [27] W. Christen and K. Rademann. Cooling and slowing in high-pressure jet expansions. *Phys. Rev. A*, 77:012702, Jan 2008.
- [28] http://web-docs.gsi.de/~stoe_exp/laboratory/environment/gasjet/gasjet.php.
- [29] F. Nolden et al. Radioactive beam accumulation for a storage ring experiment with an internal target. *4th International Particle Accelerator Conference, Shanghai, China*, page 91, 2013.
- [30] T. Gassner et al. Spatial characterisation of the internal gas target at the ESR for the FOCAL experiment. *GSI Scientific Report*, 2013.
- [31] T. Gassner. private communication, 2014.
- [32] H. Moeini et al. First feasibility experiment for the EXL project with prototype detectors at the ESR storage ring. *Nucl. Instr. and Meth. A*, 634:77, (2011).
- [33] M. Mutterer et al. Experimental techniques for in-ring reaction experiments. *Proc. Int. Conf. STORI14*.
- [34] M. Lindemulder. KVI-CART, Groningen, (private communication), 2012.
- [35] G. F. Knoll. *Radiation detection and measurement*. John Wiley & Sons, Inc., 2010.
- [36] M. von Schmid. *Nuclear matter distribution of ^{56}Ni measured with EXL*. PhD thesis, TU Darmstadt, 2015.

-
- [37] Multi branch system, MBS. <https://www.gsi.de/mbs>.
- [38] ROOT, data analysis framework. <https://root.cern.ch/drupal/>.
- [39] E. Falk et al. Algorithms for reduction of coherent noise in the silicon shower maximum detector of STIC. *DELPHI*, 97-60 CAL 137, 1997.
- [40] D. H. Son et al. Signal-to-noise ratio measurement of a Double-sided Silicon Strip Detectors by using 45 MeV proton beam. *Journal of the Korean Physical Society*, 52(3):949–953, 2008.
- [41] T. Frisson and R. Poeschl. Coherent noise source identification in multi channel analysis. *arXiv:1401.7095*, 2014.
- [42] M. Morhac et al. Identification of peaks in multidimensional coincidence γ -ray spectra. *Nucl. Instrum. and Methods A*, 443(1):108 – 125, 2000.
- [43] V. Eremin. Ioffe, St. Petersburg, Russia, (private communication), 2013.
- [44] Stopping-power and range tables for electrons, protons, and helium ions. <http://www.nist.gov/pml/data/star/index.cfm>.
- [45] S. Litvinov. GSI, Germany, (private communication), 2014.
- [46] H. Wiedemann. *Particle Accelerator Physics II*. Springer-Verlag, 1995.
- [47] Y. A. Litvinov. *Basic Nuclear Properties of Neutron-Deficient Nuclei investigated via High Precision Mass Measurements in the Element Range of $36 < Z < 92$* . PhD thesis, Justus-Liebig Universität Giessen, 2003.
- [48] Ionivac transmitters itr 90, DATASHEET. <http://www.elvac.com.pl/ITR90.pdf>.
- [49] H. Wiedemann. *Particle Accelerator Physics I*. Springer-Verlag, 1995.
- [50] D.A. Edwards and J. Syphers. *An Introduction to the Physics of High Energy Accelerators*. Wiley Series in Beam Physics and Accelerator Technology. Wiley, 2008.
- [51] A. Chao. *Handbook of Accelerator Physics and Engineering*. Handbook of Accelerator Physics and Engineering. World Scientific, 1999.
- [52] S. Ilieva et al. Feasibility studies of the EXL setup for FAIR using the GSI storage ring ESR. *Eur. Phys. J. Special Topics*, 150:357–358, 2007.
- [53] T.M. Apostol. *Calculus*. Number v. 1 in Blaisdell Mathematics Series. Blaisdell Publishing Company, 1961.
- [54] E. Byckling and K. Kajantie. *Particle kinematics*. A Wiley-Interscience publication. Wiley, 1973.
- [55] Geant4 Collaboration. Geant4 simulation toolkit. *Nucl. Instrum. and Methods A*, 506(3):250 – 303, 2003.
- [56] C. M. Poole et al. A CAD Interface for GEANT4. *Arxiv preprint arXiv:1105.0963*.
- [57] M. Steck et al. Electron cooling experiments at the ESR. *Nucl. Instr. and Meth. A*, 532(1-2):357–365, 2004.
- [58] FRESCO program. <http://www.fresco.org.uk/>.
- [59] P. D. Kunz. Program CHUCK3. (*University of Colorado, unpublished*), 1978.

-
- [60] J. Raynal. Notes on ECIS94. *CEA Sclay Report No. CEA-N-2772*, 1994.
- [61] N. S. Chant. Program THREEDEE. (*University of Maryland, unpublished*).
- [62] R. Shinnar and G. H. Weiss. A note on the resolution of two gaussian peaks. *Separ. Sci*, 11(377), 1976.
- [63] D. T. Doherty. PhD thesis, University of Edinburgh, 2013.
- [64] G. Marsaglia. Choosing a point from the surface of a sphere. *Ann. Math. Stat.*, 43:645–646, 1972.
- [65] Y.-W. Lui et al. Isoscalar giant resonances for nuclei with mass between 56 and 60. *Phys. Rev. C*, 73:014314, 2006.
- [66] C.A. Bertulani and P. Danielewicz. *Introduction to nuclear reactions*. Institute of Physics (IOP), 2004.
- [67] N.K. Glendenning. *Direct Nuclear Reactions*. World Scientific, 2004.
- [68] G. R. Satchler. *Direct Nuclear Reactions*. Oxford science publications. Oxford University Press, 1983.
- [69] P. Fröbrich and R. Lipperheide. *Theory of Nuclear Reactions*. Oxford science publications. Clarendon Press, 1996.
- [70] G.R. Fowles. *Introduction to Modern Optics*. Dover Books on Physics. Dover Publications, 1975.
- [71] G. D. Alkhasov et al. Nuclear radii of unstable nuclei. *International Journal of Modern Physics E*, 20(03):583–627, 2011.
- [72] R. J. Glauber. *Lectures in Theoretical Physics, vol 1*. Interscience Publishers, New York, 1959.
- [73] R.J. Glauber and G. Matthiae. High-energy scattering of protons by nuclei. *Nuclear Physics B*, 21(2):135 – 157, 1970.
- [74] B. Abu-Ibrahim et al. Calculation of the complete glauber amplitude for p+6He scattering. *Nucl. Phys. A*, 657(4):391 – 410, 1999.
- [75] K. Varga et al. Monte Carlo integration in Glauber model analysis of reactions of halo nuclei. *Phys. Rev. C*, 66:034611, Sep 2002.
- [76] J. Chauvin et al. Low and intermediate energy nucleus-nucleus elastic scattering and the optical limit of Glauber theory. *Phys. Rev. C*, 28:1970–1974, Nov 1983.
- [77] A. Vitturi and F. Zardi. Modified Glauber model for the description of elastic scattering between heavy ions. *Phys. Rev. C*, 36:1404–1407, Oct 1987.
- [78] M. H. Cha. Modified Glauber model II description for heavy-ion elastic scattering. *Phys. Rev. C*, 46:1026–1029, Sep 1992.
- [79] S. K. Charagi and S. K. Gupta. Nucleus-nucleus elastic scattering at intermediate energies: Glauber model approach. *Phys. Rev. C*, 56:1171–1174, Aug 1997.
- [80] L. Ray. Proton-nucleus total cross sections in the intermediate energy range. *Phys. Rev. C*, 20:1857–1872, Nov 1979.
- [81] M. S. Hussein, R. A. Rego, and C. A. Bertulani. Microscopic theory of the total reaction cross section and application to stable and exotic nuclei. *Phys. Rep.*, 201:279–334, 1991.

- [82] J.J. Sakurai. *Modern Quantum Mechanics*. Addison-Wesley, 1994.
- [83] F Petrovich and W.G. Love. The scattering of elementary probes from nuclei at medium energy: A new look at the nucleus. *Nucl. Phys. A*, 354(1-2):499 – 534, 1981.
- [84] Dao T. Khoa et al. Folding model analysis of elastic and inelastic proton scattering on sulfur isotopes. *Nucl. Phys. A*, 706(1-2):61 – 84, 2002.
- [85] P Ring and P. Schuck. *The Nuclear Many-Body Problem*. Physics and astronomy online library. Springer, 2004.
- [86] A.J. Koning and J.P. Delaroche. Local and global nucleon optical models from 1 keV to 200 MeV. *Nucl. Phys. A*, 713(3-4):231–310, 2003.
- [87] H. De Vries et al. Nuclear charge-density-distribution parameters from elastic electron scattering. *Atomic Data and Nuclear Data Tables*, 36(3):495–536, 1987.
- [88] James J. Kelly. Nucleon charge and magnetization densities from Sachs form factors. *Phys. Rev. C*, 66:065203, Dec 2002.
- [89] J. J. Kelly. Simple parametrization of nucleon form factors. *Phys. Rev. C*, 70:068202, Dec 2004.
- [90] G.R. Satchler and W.G. Love. Folding model potentials from realistic interactions for heavy-ion scattering. *Phys. Rep.*, 55(3):183–254, 1979.
- [91] A.M. Kobos et al. Folding-model analysis of elastic and inelastic α -particle scattering using a density-dependent force. *Nucl. Phys. A*, 425(2):205–232, 1984.
- [92] G. B. Arfken and Weber H. J. *Mathematical Methods for Physicists*. Harcourt/Academic Press), 2001.
- [93] P Fröbrich and R. Lipperheide. *Theory of nuclear reactions*. Oxford University Press Inc., New York, 1996.
- [94] P J. Karol. Nucleus-nucleus reaction cross sections at high energies: Soft-spheres model. *Phys. Rev. C*, 11:1203–1209, Apr 1975.
- [95] I. Tanihata et al. Measurements of interaction cross sections and nuclear radii in the light p -shell region. *Phys. Rev. Lett.*, 55:2676–2679, Dec 1985.
- [96] S. Kox et al. Trends of total reaction cross sections for heavy ion collisions in the intermediate energy range. *Phys. Rev. C*, 35:1678–1691, May 1987.
- [97] R. K. Tripathi et al. Proton-nucleus total cross sections in coupled-channel approach. *NASA/TP-2000-210534*, 2000.
- [98] CODATA. The NIST reference on constants, units and uncertainty. <http://physics.nist.gov/cuu/Constants/index.html>.
- [99] L. Chulkov et al. Interaction cross sections and matter radii of $A = 20$ isobars. *Nucl. Phys. A*, 603(2):219–237, 1996.
- [100] J. Kelly et al. Neutron transition density for the lowest $2+$ state of ^{18}O . *Phys. Lett. B*, 169(2-3):157–160, 1986.
- [101] N. D. Chien and D. T. Khoa. Neutron transition strengths of 2_1^+ states in the neutron-rich oxygen isotopes determined from inelastic proton scattering. *Phys. Rev. C*, 79:034314, Mar 2009.

- [102] A. Bohr and B.R. Mottelson. *Nuclear Structure*. Number v. 2 in Nuclear Structure. World Scientific, 1998.
- [103] National Nuclear Data Center. <http://www.nndc.bnl.gov/>.
- [104] S. Raman et al. Transition probability, $B(E2)$, from the ground to the first-excited $2+$ state of even-even nuclides. *Atomic Data and Nuclear Data Tables*, 36(1):1–96, 1987.
- [105] A. Gade and T. Glasmacher. In-beam nuclear spectroscopy of bound states with fast exotic ion beams. *Progress in Particle and Nuclear Physics*, 60(1):161 – 224, 2008.
- [106] Program MINUIT. www.cern.ch/minuit.
- [107] G. R. Satchler and Dao T. Khoa. Missing monopole strength in ^{58}Ni and uncertainties in the analysis of α -particle scattering. *Phys. Rev. C*, 55:285–297, Jan 1997.
- [108] C.A. Bertulani et al. A computer program for nuclear scattering at intermediate and high energies. *Comput. Phys. Commun.*, 152(3):317 – 340, 2003.
- [109] G. Cowan. *Statistical Data Analysis*. Oxford science publications. Clarendon Press, 1998.
- [110] G. Colò et al. Self-consistent RPA calculations with Skyrme-type interactions. *Comput. Phys. Commun.*, 184(1):142–161, 2013.
- [111] P.-G. Reinhard et al. Shape coexistence and the effective nucleon-nucleon interaction. *Phys. Rev. C*, 60:014316, Jun 1999.
- [112] L. Ray et al. Uncertainties in neutron densities determined from analysis of 0.8 GeV polarized proton scattering from nuclei. *Phys. Rev. C*, 18:2641–2655, Dec 1978.
- [113] S. Terashima et al. Proton elastic scattering from tin isotopes at 295 MeV and systematic change of neutron density distributions. *Phys. Rev. C*, 77:024317, Feb 2008.
- [114] J. Carter et al. Role of knockout contributions in giant resonance studies with $(p, p'x)$ reactions. *Phys. Rev. C*, 63:057602, Apr 2001.
- [115] B. Bonin et al. Response functions of ^{58}Ni , ^{116}Sn AND ^{208}Pb to the excitation of intermediate-energy α particles. *Nucl. Phys. A*, 430(2):349–396, 1984.
- [116] C. Monrozeau et al. First measurement of the giant monopole and quadrupole resonances in a short-lived nucleus: ^{56}Ni . *Phys. Rev. Lett.*, 100:042501, Jan 2008.
- [117] D. H. Youngblood et al. Systematics of the giant monopole resonance from inelastic alpha scattering. *Phys. Rev. C*, 23:1997–2007, May 1981.
- [118] D. H. Youngblood and Y.-W. Lui. Monopole strength in ^{58}Ni . *Phys. Rev. C*, 44:1878–1881, Nov 1991.
- [119] Y.-W. Lui et al. Giant monopole strength in ^{58}Ni . *Phys. Rev. C*, 61:067307, May 2000.
- [120] A. Krasznahorkay et al. Excitation of the isovector giant dipole resonance by inelastic α scattering and the neutron skin of nuclei. *Phys. Rev. Lett.*, 66:1287–1290, Mar 1991.
- [121] R. Klein et al. Electroexcitation of giant resonances in ^{58}Ni . *Phys. Lett. B*, 145(1-2):25 – 28, 1984.
- [122] M.A. Caprio. LevelScheme: A level scheme drawing and scientific figure preparation system for Mathematica. *Comput. Phys. Commun.*, 171(2):107 – 118, 2005.

- [123] H.M. Sen Gupta et al. A study of the level structure in ^{57}Fe from the (d,p) reaction on ^{56}Fe . *Nucl. Phys. A*, 160(3):529–549, 1971.
- [124] H. Toyokawa et al. Coupling effects studied in the $^{13}\text{C}(p, pn)^{12}\text{C}$ and $^{13}\text{C}(p, d)^{12}\text{C}$ reactions at $e_p = 35$ MeV. *Phys. Rev. C*, 51:2592–2596, May 1995.
- [125] R. C. Johnson and P. J. R. Soper. Contribution of deuteron breakup channels to deuteron stripping and elastic scattering. *Phys. Rev. C*, 1:976–990, Mar 1970.
- [126] W. N. Cartford. *The Euroschool on Exotic Beams, vol IV; Chapter 3*. Lectures notes in Physics 879. Springer, 2014.
- [127] Y. Sakuragi. Energy and target dependence of projectile breakup effect in elastic scattering of ^6Li . *Phys. Rev. C*, 35:2161–2174, Jun 1987.
- [128] I.J. Thompson et al. The threshold anomaly in $^{16}\text{O} + ^{208}\text{Pb}$ scattering. *Nucl. Phys. A*, 505(1):84 – 102, 1989.
- [129] F. Hinterberger et al. Inelastic scattering of 52 MeV deuterons. *Nucl. Phys. A*, 115(3):570 – 592, 1968.
- [130] K.I. Kubo. Reexamination of the DWBA method in the deuteron stripping reaction. *Progress of Theoretical Physics*, 44(4):929 – 951, 1970.
- [131] E. Caurier et al. The shell model as a unified view of nuclear structure. *Rev. Mod. Phys.*, 77:427–488, Jun 2005.
- [132] B. Alex Brown and W. A. Richter. New “USD” hamiltonians for the *sd* shell. *Phys. Rev. C*, 74:034315, Sep 2006.
- [133] Yinlu Han et al. Deuteron global optical model potential for energies up to 200 MeV. *Phys. Rev. C*, 74:044615, Oct 2006.
- [134] M. A. Najafi et al. In-beam test of EXL demonstrator at KVI. *EXL collaboration, Internal Report*, (2011).
- [135] PHOTONIS. <http://www.photonis.com/>.
- [136] D. Torresi et al. Influence of the interstrip gap on the response and the efficiency of double sided silicon strip detectors. *Nucl. Instr. and Meth. A*, 713(0):11–18, 2013.
- [137] J.A. Duenas et al. Interstrip effects influence on the particle identification of highly segmented silicon strip detector in a nuclear reaction scenario. *Nucl. Instr. and Meth. A*, 743(0):44–50, 2014.
- [138] E. Belau et al. Charge collection in silicon strip detectors. *Nuclear Instruments and Methods in Physics Research*, 214(2-3):253–260, 1983.
- [139] H. Ikeda and S. Okuno. Characterization of the wide-pitch ohmic-side readout for a silicon micro-strip detector. *Nucl. Instr. and Meth. A*, 365(2-3):462–472, 1995.
- [140] B. Streicher. GSI, Darmstadt, (private communication), 2012.
- [141] H. Moeini. *Feasibility experiment and simulations for EXL*. PhD thesis, University of Groningen, 2010.
- [142] F. Nunes. Continuum-Discretised Coupled Channels methods. 6(9):10497, 2011.

-
-
- [143] A. Moro. Nuclear Reactions: applications and examples. Lecture at TRIUMF Summer Institute, 2008. Unpublished.
- [144] N. Austern, , et al. Continuum-discretized coupled-channels calculations for three-body models of deuteron-nucleus reactions. *Phys. Rep.*, 154(3):125 – 204, 1987.
- [145] I. J. Thompson. Coupled reaction channels calculations in nuclear physics. *Comput. Phys. Rep.*, 7(4):167 – 212, 1988.

Curriculum vitae

Personal Information

Name: Juan Carlos Zamora Cardona

Date of Birth: 12-04-1983

Nationality: Colombian

Gender: Male

Email: jczamorac@ikp.tu-darmstadt.de

Email: jczamorac@gmail.com

Academic Information

2011 - current Doctor of Philosophy in Physics

Technische Universität Darmstadt, TUD, Germany

Thesis Title: Nuclear Reaction Studies using Stored Ion Beams at ESR with EXL

Advisor: Thorsten Kröll

Key-Words: Stored beams; Inverse kinematics; Elastic Scattering; Isoscalar Giant Resonances; Transfer Reaction

2009 - 2011 Master of Science in Physics

Universidade de São Paulo, USP, Brazil

Thesis Title: Study of the elastic scattering of $^{7,9,10}\text{Be}$ on a carbon target

Advisor: Valdir Guimarães

Key-Words: Exotic Nuclei; Elastic Scattering; Radioactive Nuclei; Break-up reaction

2003 - 2008 Bachelor of Science in Physics (5 years program)

Universidad Nacional de Colombia, UNAL, Colombia

Thesis Title: Influence of humidity in the soil physical properties

Advisor: Fernando Cristancho

Key-Words: Nuclear instrumentation; Soil moisture; Neutron probe

Professional Experience

2011 - 2014

Technische Universität Darmstadt, Germany

Type of contract: Tutor in the advanced nuclear physics laboratory

Working hours (weekly): 6

2007 - 2008

Centro Internacional de Física, CIF, Colombia

Type of contract: Researcher. Using the neutron backscattering technique to investigate soil properties

Working hours (weekly): 25

2006 - 2007

Universidad Nacional de Colombia, UNAL, Colombia

Type of contract: Scholarship (Monitor del departamento de Física)

Working hours (weekly): 8

Awards

2011 Fellowship, grantee of TU Darmstadt-GSI cooperation

2009 Student scholarship for master students, CNPq

2008 Honours degree. Bachelor of Science in Physics, Universidad Nacional de Colombia

Bibliographical Production

Articles in Scientific Journals

1. V. Morcelle et al., *Physics Letters B* **732**, 228 (2014)
2. V. Morcelle et al., *Physical Review. C* **89**, 044611 (2014)
3. D. Mendes et al., *Physical Review. C* **86**, 064321 (2012)
4. J. C. Zamora et al., *Physical Review. C* **84**, 034611 (2011)
5. A. Barioni et al., *Physical Review. C* **84**, 014603 (2011)
6. K. Pires et al., *Physical Review. C* **83**, 064603 (2011)
7. A. Lépine-Szily et al., *Nuclear Physics. A* **834**, 491c (2010)
8. J. C. Zamora et al., *American Journal of Physics* **77**, 169 (2009)

Proceedings of conferences

1. J. C. Zamora et al., *Physica Scripta T* **166**, 014006 (2015)
2. M. von Schmid et al., *Physica Scripta T* **166**, 014005 (2015)
3. M. Mutterer et al., *Physica Scripta T* **166**, 014053 (2015)
4. D. Doherty et al., *Physica Scripta T* **166**, 014007 (2015)
5. P. Egelhof et al., *JPS Conference Proceedings* **6**, 020049 (2015)
6. M. von Schmid et al., *EPJ Web of Conferences* **66**, 03093 (2014)
7. A. Lépine-Szily et al., *EPJ Web of Conferences* **69**, 00006 (2014)
8. V. Guimarães et al., *Journal of Physics. Conference Series* **312**, 082024 (2011)
9. J. C. Zamora et al., *XXXII Reunião de Trabalho sobre Física Nuclear no Brasil*, XXXII, 18 (2009)
10. J. C. Zamora and F. Cristancho, *XII International Workshop on Nuclear Physics*, Havana-Cuba (2009)